Numeró d'ordre : 21 - 2014 12 Fevrier 2014

Université Claude Bernard - Lyon 1

Institut Camille Jordan - CNRS UMR 5208
École doctorale InfoMaths

Thèse

de l'université de Lyon

pour obtenir le titre de

Docteur en Sciences
Mention : Mathématiques appliquées

présentée par

Alen Tosenberger

Blood flow modelling and applications to blood coagulation and atherosclerosis

Thèse dirigée par Vitaly Volpert
préparée a l'Université Lyon 1

Jury:

Charles Auffray	DR au CNRS, EISBM, Lyon	Examinateur
Jean-Claude Bordet	Biologiste, Laboratoire de Recherche sur l'Hémophilie, Lyon 1	Examinateur
Ionel Sorin Ciuperca	MCF, Institut Camille Jordan, Univ. Lyon 1	Examinateur
Elaine Crooks	Professeur, Swansea University	Examinateur
Andreas Deutsch	Professeur, Technische Universit at Dresden	Examinateur
Adélia Sequeira	Professeur, Instituto Superior Técnico	Rapporteur
Angélique Stéphanou	CR au CNRS, IN3S, Grenoble	Rapporteur
Vitaly Volpert	DR au CNRS, Université Lyon 1	Directeur de Thèse

Résumé

La thèse est consacrée à la modélisation discrète et continue des écoulements sanguins et des phénomènes connexes tels que la coagulation du sang et l'athérosclérose. Ce travail comprend l'élaboration des modèles mathématiques et numériques de la coagulation du sang, des simulations numériques et l'analyse mathématique d'un modèle d'inflammation chronique au cours d'athérosclérose. Une partie importante de la thèse est liée a la programmation, la mise en oeuvre et l'optimisation des codes numériques.

La partie principale de la thèse concerne la modélisation de la coagulation du sang in vivo tenant compte des écoulements sanguins, les réactions biochimiques dans le plasma et l'agrégation de plaquettes. La nouveauté principale de ce travail est l'élaboration d'un modèle hybride (discret-continu) de la coagulation du sang et de la formation de caillot sanguin dans le flux. La partie discrète du modèle est basée sur la méthode particulaire appelée la Dynamique des Particules Dissipatives (DPD). En raison de sa nature discrète, la méthode DPD nous permet de décrire des cellules sanguines individuelles. Cette méthode est utilisée pour la modélisation de l'écoulement du plasma sanguin, des plaquettes et de leur agrégation. La partie continue du modèle utilise les équations aux dérivées partielles pour décrire les concentrations de substances biochimiques dans le plasma et leurs réactions lors de la coagulation. Plusieurs aspects de la coagulation ont été étudiés: l'agrégation de plaquettes et son interaction avec les réactions biochimiques de coagulation, l'influence de la vitesse d'écoulement sur le développement d'un caillot sanguin ainsi que comment la croissance du caillot s'arrête. Le modèle a montré l'importance de l'interaction entre l'agrégation de plaquettes et les réactions de coagulation. La vitesse d'écoulement est faible à l'intérieur des caillots, ce qui permet de déclencher la cascade de coagulation et de renforcer l'agrégat accroissant par la formation du polymère de fibrine. La pression exercée par le flux sanguin enlève les parties extérieures du caillot et arrête finalement la croissance.

La partie théorique de la thèse est consacrée à l'analyse mathématique d'un modèle d'inflam-mation chronique liée à l'athérosclérose. Auparavant, il a été montré que l'inflammation se propage comme une onde de réaction-diffusion dont les caractéristiques dépendent du niveau du mauvais cholestérol dans le sang. Dans cette thèse, nous étudions un modèle décrivant la propagation d'une onde de réaction-diffusion dans le cas 2D avec des conditions aux limites non-linéaires. Nous utilisons la méthode de Leray-Schauder et des estimations à priori des solutions afin de prouver l'existence d'ondes dans le cas bistable.

Les simulations numériques réalisées dans le cadre de cette thèse impliquent l'élaboration des algorithmes numériques pour les modèles mathématiques et le développement des logiciels. Vu le fait que les simulations numériques ont été coûteuse en temps de calcul, des efforts considérables ont été consacrés à la parallélisation des logiciels et à leur optimisation.

Mots-clés : modèles hybrides, Dissipative Particle Dynamics, équations aux dérivées partielles, coagulation du sang, développement de caillot sanguin, athérosclérose.

Abstract

The thesis is devoted to discrete and continuous modelling of blood flows and related phenomena such as blood coagulation and atherosclerosis. It includes the development of mathematical and numerical models of blood coagulation, numerical simulations and the mathematical analysis of a model problem of chronic inflammation during atherosclerosis. An important part of the thesis is related to programming, implementation and optimization of numerical codes.

The main part of the thesis concerns modelling of blood coagulation in vivo which takes into account blood flows, biochemical reactions in plasma and platelet aggregation. The main novelty of this work is the development of a hybrid (discrete-continuous) model of blood coagulation and clot formation in flow. The discrete part of the model is based on a particle method called Dissipative Particle Dynamics (DPD). Due to the discrete nature of the DPD method, it allows the description of individual blood cells. This method is used to model blood plasma flow, platelets suspended in it and platelet aggregation. The continuous part of the model is based on partial differential equations for the concentrations of biochemical substances in the blood plasma and their reactions during blood coagulation. Several aspects of blood coagulation in flow were studied: platelet aggregation and its interaction with coagulation pathways, influence of the flow speed on the clot development, a possible mechanism by which clot stops growing. The model showed the importance of the interaction between platelet aggregation and coagulation pathways. Since the flow velocity is small inside of the platelet clot, it is possible for the coagulation cascade to begin and to reinforce the growing aggregate by the formation of a fibrin network. The pressure from the blood flow removes the outer parts of the platelet clot and eventually stops it growth.

The theoretical part of the thesis is devoted to the mathematical analysis of a model of chronic inflammation related to atherosclerosis. Previously it was shown that inflammation propagates as a reaction-diffusion wave whose properties depend on the level of bad cholesterol in blood. In this thesis we study a model problem which describes the propagation of a reaction-diffusion wave in the 2D case with non-linear boundary conditions. We use the Leray-Schauder method and a priori estimates of solutions in order to prove the existence of waves in the bistable case.

Numerical simulations carried out in the framework of this thesis were based on the numerical implementation of the corresponding models and on the software development. Since the numerical simulations were computationally expensive, a substantial effort was directed to software parallelization and optimization.

Key words: hybrid models, Dissipative Particle Dynamics, partial differential equations, blood coagulation, clot growth, atherosclerosis.

Acknowledgements

I would like to express my deepest gratitude to my supervisor Vitaly Volpert for his clear and comprehensive guidance and unreserved support throughout my PhD.

I would also like to extend my sincere appreciation to Nikolay Bessonov from the Institute of Mechanical Engineering Problems in Saint Petersburg for the invaluable advise and ideas on numerical methods.

My deep appreciation is extended to Fazly Ataullakhanov, Mikhail Panteleev and Alexey Tokarev from the National Research Center for Haematology in Moscow for the valuable collaboration and for providing the insight into the most recent advancements in the experimental research of blood coagulation.

I am very grateful to the reporters Adélia Sequeira and Angélique Stephanou, and the jury members Charles Auffray, Jean-Claude Bordet, Ionel Sorin Ciuperca, Elaine Crooks and Andreas Deutsch, for coming to Lyon and participating in the thesis defence, as well as for their exhaustive questions and comments.

I would also like to give special thanks to my colleagues from the INRIA Dracula team in Lyon, for their kind support and collegiality during my PhD, especially to Mostafa Adimy, Samuel Bernard, Fabien Crauste, Olivier Grandrillon, Thomas Lepoutre, Laurent Pujo-Menjouet and Caroline Lothe.

Moreover, I would like to extend my gratitude to Grigory Panasenko from Université de Saint-Etienne and Jean-Pierre Lohéac from Ecole Centrale de Lyon for providing several opportunities to present my work.

Last but not least, I would like to thank my wife Mathea, my family and my friends for sharing both the good and the bad moments, for their love and encouragement.

Contents

Chapter 1

Introduction

The thesis is devoted to blood flow modelling with applications to blood coagulation and atherosclerosis. In this introduction these physiological processes and the state of the art in their mathematical modelling will be described. The introduction finishes with the presentation of the main results of the thesis.

1.1 Blood flow

1.1.1 Biological background

The blood is one of the largest organs in the body, which performs the essential function of delivering oxygen and nutrients to all tissues and cells, as well as of taking away the metabolic waste products. As the cardiovascular system spans through the whole body, blood has the role of supporting the function of all other body tissues. By transporting antibodies the blood also makes it possible for the organism to react to and fight infections. Other functions include coagulation, which is a body's self-repair mechanism, messenger functions, by transporting hormones and signalling tissue damage, and regulation of body pH and temperature. Because of its functions and presence in all tissues of the body, blood and cardiovascular system are involved with the most pathological events and the related healing approaches, either as a cause of a disease, as a tissue that can be involved in various ways with the effects of the disease, as a way to administer the medicine and to counteract or cure the disease. Due to its important role and involvement in body functions and diseases, but also due to the easy sampling of blood, it has been in a focus of numerous medical, biological, chemical, physical, mathematical and pharmaceutical studies, and is probably one of the most intensively studied organs. Histologically, blood is considered to be a connecting tissue. However, being a fluid it differs largely from other connecting tissues.

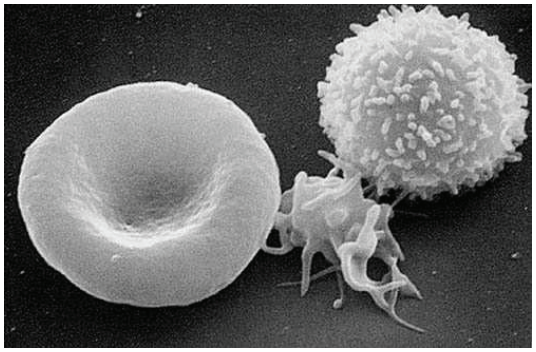

Figure 1.1: Image of blood cells taken by Scanning Electron Microscope (SEM). From left to right: erythrocyte, thrombocyte and leukocyte. Electron Microscopy Facility at The National Cancer Institute at Frederick, 2011.

The blood consists of its fluid component, called plasma, and blood cells that are suspended in the plasma. Blood plasma, which is an aqueous solution of electrolytes, proteins and small organic molecule like glucose, occupies about 50-60% of the blood volume. The blood cells (Figure 1.1) which occupy the remaining 40-50% of the blood volume are divided into erythrocytes (or red blood cells - RBC), thrombocytes (or platelets), and leukocytes (or white cells). Erythrocytes are the most numerous of blood cells, with concentration of about 5×10^{12} per litre of blood, taking about 45% of the blood volume. The value of erythrocyte volume in total blood is usually referred to as the hematocrit. They are produced in the red bone marrow of large bones in a process called erythropoiesis, which takes about 7 days. Their lifespan is about 120 days in a healthy individual, at the end of which erythrocytes undergo a change in its plasma membrane, making it susceptible to selective recognition by macrophages and subsequent phagocytosis in the mononuclear phagocyte system. The main role of erythrocytes is to transport oxygen from the lungs to other tissues. Their cytoplasm is rich in molecules called haemoglobin, which contain iron allowing them to bind oxygen. Iron is also responsible for the blood's red color. Mature erythrocytes do not have nuclei, and thus have more space for haemoglobin. By not having nucleus they do not contain any mitochondria. As a result erythrocytes spend no oxygen they carry, making the process of oxygen transportation more efficient. The normal erythrocyte in a relaxed state has a biconcave discoid shape with a diameter of about 7.65 μm, and a thickness of about 2.84 and 1.44 μm at its thickest part and its centre respectively. The volume of an erythrocyte is about 98 μm^3, while its surface area is about 130 μm^2. Due to the relatively large surface area to volume ratio and the visco-elastic properties of their membrane, erythrocytes can greatly deform without significant strain. The change in shape of erythrocytes can be a result of mechanical, chemical or thermal effects. Their ability to change shape under external factors makes erythrocytes suitable for their task of transferring oxygen to tissues, where they flow through capillaries of much smaller diameter than their own (down to 3 μm).

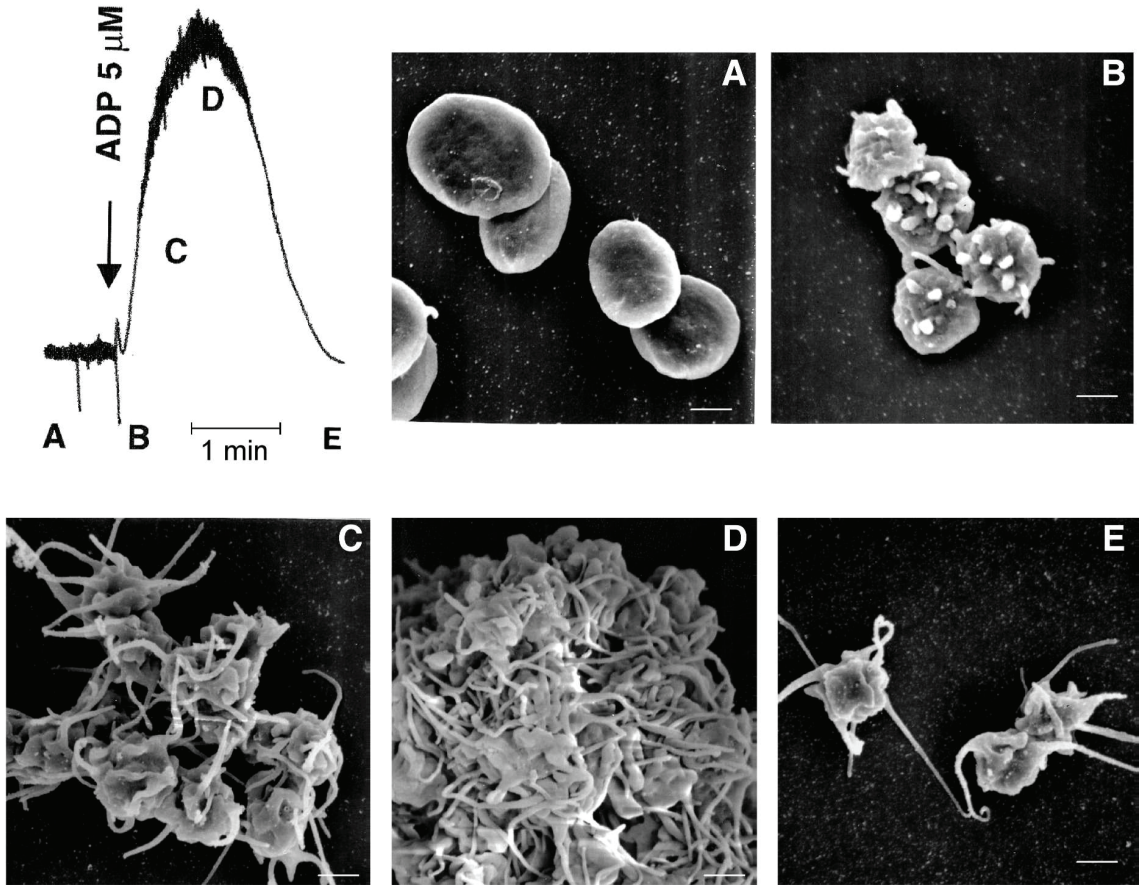

Figure 1.2: Morphological changes of washed platelets during ADP induced aggregation. An aggregation response was obtained by stimulating platelets with 5 μM ADP (arrow). The platelets were fixed at different time points and their surface features were visualized by scanning electron microscopy (SEM). (A) Discoid cells in the resting state. (B) Formation of early pseudopods (7 s). (C) Full shape change and first platelet-platelet interactions (20 s). (D) Large platelet aggregates (45 s). (E) Isolated platelets after disaggregation (3 min). Bars = 1 μm. Reprinted with permission from [22] – *J.-P. Cazenave et al., Methods in Molecular Biology, Springer, 2004.*

The second most numerous type of blood cells is the thrombocyte or platelet. Platelet concentration is of about 150-440 $\times$ 10^9 per litre of blood. They are discoid anucleate cells (Figure 1.1), that are much smaller than erythrocytes, having a diameter of about 3 μm, thickness of about 1 μm and volume of about 7 μm^3. The platelets are derived from cells in the marrow called megakaryocytes and their lifespan in circulation is between 10 and 12 days. The main role of platelets is the prevention of blood loss, by aggregation at the injury site. Although their membranes resemble the membrane of an erythrocyte, its detailed structure and function is much more complex. The external side of the membrane is exceptionally rich in receptors - GPIb, a primary receptor for von Willebrand factor (vWF) which serves to

mediate the initial adhesion between the platelets, GPIIb/IIIa which acts as a receptor for fibrinogen and vWF and others like receptors for ADP and thrombin which also play a role in the platelet aggregation. Except receptors that are present on the surface of a platelet, a second mechanism exists to facilitate the platelet aggregation (Figure 1.2). In this process, known as platelet activation, platelets undergo a shape change from the initial discoid shape to a more spherical shape with pseudopodia (stellate shape). The drastic change in shape increases the surface of platelets and thus facilitates surface adhesion interactions. In the early stages of activation the shape change is still reversible, while after they have undergone the full transformation, the change becomes irreversible.

The least numerous type of blood cells is the leukocyte, with a concentration of about 5×10^9 per litre of blood. Together with platelets, leukocytes account for 1% of the total blood volume. They are roughly spherical in shape with a diameter ranging from 7 to 22 μm. Their function is to fight infection in the body through both the destruction of bacteria and viruses, and the formation of antibodies and sensitized lymphocytes. Leukocytes are produced in the bone marrow and partially in the lymph tissue. While they are constantly present in a healthy blood stream, about three times more leukocytes are stored in the bone marrow, from where they can be rapidly deployed to different parts of the organism in a case of infection or inflammation. Morphologically, there are five different types of leukocytes, specialized for specific and non-specific reactions on foreign materials in the organism. The five types of leukocytes are: neutrophils, eosinophils, basophils, monocytes and lymphocytes. The first three groups, collectively known as "granulocytes" make 50-75% of the total number of circulating leukocytes. Granulocytes are responsible for a rapid defensive response upon detection of foreign materials in the organism. Monocytes and lymphocytes are responsible for a slower but more powerful defensive reaction. While lymphocytes are responsible for antigen-specific immune responses, the monocytes have a non-specific phagocytic function.

1.1.2 Modelling

Because of its importance, blood was extensively studied on both the macro and the micro level. A significant part of these studies included modelling of blood flows, in order to investigate blood flow mechanical and bio-chemical properties, as well as blood related phenomena like blood coagulation or atherosclerosis.

The blood flow characteristics come from three involved parts. The first part are blood vessels that influence the blood flow by their type, size and elastic properties. There are three main types of blood vessels: arteries, veins and capillaries. Arteries and veins are larger blood vessels, which carry the blood away and towards the heart respectively, while capillaries are smaller blood vessels which enable the exchange of water and chemicals between the blood and tissues. Arteries and veins contain a muscle layer which allows them to regulate their inner diameter by its contraction. The second part that influences the blood flow is the

heartbeat, i.e. the heart produces a pulsatile flow by its periodic contractions. This results in oscillations in the flow speed and pressure between heartbeats. The third part is blood, which composition is described in the previous section. All of the three parts - blood vessels, heartbeat, blood - are very complex systems and are thus in most models described with different level of details, usually having only one system in the focus of a study.

As a fluid blood is incompressible and has non-Newtonian properties, i.e. its viscosity depends on the shear rate. Although this property of blood comes from the properties of erythrocytes and other blood cells, which account for about 45% of blood volume, on the macro scale blood is usually modelled as a homogeneous fluid. In the classical approaches blood flow is usually described by partial differential equations, commonly Navier-Stokes equations [20, 31, 50, 52, 115], which, based on the properties of the fluid (density, viscosity), pressure or body force, and the given domain, give the corresponding velocity field. Furthermore, continuous approaches use differential equations also to describe phenomena related to blood flows. Concentrations of various substances are modelled with partial differential equations able to describe their diffusion and advection in the blood. Similarly, the blood cells are considered in terms of concentrations, and their motion is described also via diffusion and advection [113, 136]. The main disadvantage of continuous approaches is that they do not describe the interaction between individual blood cells in the flow. These interactions have an important impact on properties of the blood (blood flow), but they also play an essential role in many blood flow related phenomena and diseases. Nevertheless, the significance of continuous models is tremendous, as they give a mathematically well based and physically precise description of fluid behaviour related to its physical properties and provide a precise description of behaviour of other substances in the fluid.

Discrete models enable a description of individual cells and their interactions. However, the hydrodynamic properties in such models either have to be proven by a strict mathematical derivation from conservation laws and continuous hydrodynamic equations, or they have to be verified by comparison with accurate continuous models. A classical example of a discrete method is Molecular Dynamics (MD) [2, 60, 103], where the simulated medium is decomposed on particles represented by their centre of mass. The motion of the system is then determined by a pair-wise force acting between particles. In MD a single particle usually describes an atom or molecule. Hence, this method is not very efficient for studying problems on a larger scale (ex. blood flow). However, many other discrete methods were developed or adapted in order to describe complex fluids in larger domains [2, 24, 34, 55, 105, 137]. Usually such methods are referred to as meso-scale methods, because they model the complex structure of a fluid on a micro-scale, while they are still efficient for studying its effects on a macro-scale. This approach is called “coarse-graining” - the process of representing a system with fewer degrees of freedom than those actually present in the system [39, 105]. Many of such methods are not strictly mathematically derived but are rather constructed in order to satisfy certain conservation laws and symmetries that are considered to be essential for the observed phenomena. Since the interest in this area began thirty years ago, a lot of meso-scale methods and their specialised variants have been developed and a lot of effort

has been made in order to succumb their potential flaws, as well as to justify their definition by deriving them from continuous methods and conservation lows. One of the most successful and generally used methods is Dissipative Particle Dynamics (DPD) which was first described by Hoogerbrugge and Koelman in 1992 [61, 105]. By its definition DPD is a mass and momentum conservative method, and it produces a correct hydrodynamic behaviour, which was verified both analytically and by simulations. In its original description DPD method does not conserve the energy of the system, due to its definition of dissipative and random forces. However, a rigorous theoretical justification was later given by Español and Warren. In 1995 they derived the correct fluctuation dissipation relation for the friction and noise terms, while the same year Español has derived the hydrodynamic equations for the mass and momentum density fields. Since then the interest in DPD continued leading to further justifications of the method, establishing relations to other methods, like Smoothed Particle Hydrodynamics [39, 40, 105], the introduction of new integration methods for equations of motion, such as the modified Velocity-Verlet algorithm [56], and a vast number of applications. The behaviour of DPD method, as well as its suitability for the problem of fluid simulation is well described in literature [44, 45, 56, 72, 105]. In [44, 45] DPD simulation results are compared with the results obtained by using continuous methods (Navier-Stokes and Stokes equations) for Couette, Poiseuille, square-cavity and triangular-cavity flows.

Because erythrocytes constitute 95% of all cells in the blood, and occupy about 45% of the blood volume, as well as because of their complex structure and deformability, they are the most interesting blood cells to model. Therefore, most of the models of blood flow which are able to describe individual blood cells and their interactions were aimed to describe the motion of erythrocytes. Among these studies, erythrocyte membrane models are presented and the results are compared to known erythrocyte behaviour in different conditions. One of the behaviours is observed in Poiseuille flow in a micro-channel where erythrocytes take the characteristic parachute shape. This aspect was captured by both 2D and 3D RBC membrane models [62, 46, 47, 85, 87, 100, 119]. Other experimentally observed behaviours are RBC tumbling and tank-threading motion, as well as the erythrocyte response to stretching. These properties were successfully captured by 3D erythrocyte membrane models [21, 33, 46, 47, 48, 63, 100]. All these behaviours are mainly related to a single erythrocyte in the flow. The number of studies concerning blood flow in larger vessels, where blood is modelled as a suspension of blood cells in plasma, is much lower. Except the increased complexity of the problem, due to the cell collisions in flow, the reason is also the high computational demand that such models impose in larger domains (vessels) because of a large number of simulated cells. However, these studies are important to explain the behaviour of blood in the flow and its non-Newtonian properties. One of the most interesting topics is definitely the distribution of blood cells in the flow, and the mechanism which determines the distribution. As a result, erythrocytes occupy the bulk of the flow and are transferred faster due to higher velocity near the flow axis, while the platelets and leukocytes flow closer to the vessel wall. The proximity of platelets and leukocytes to the vessel wall plays an important role in many processes that occur in the vascular system, like blood coagulation and atherosclerosis.

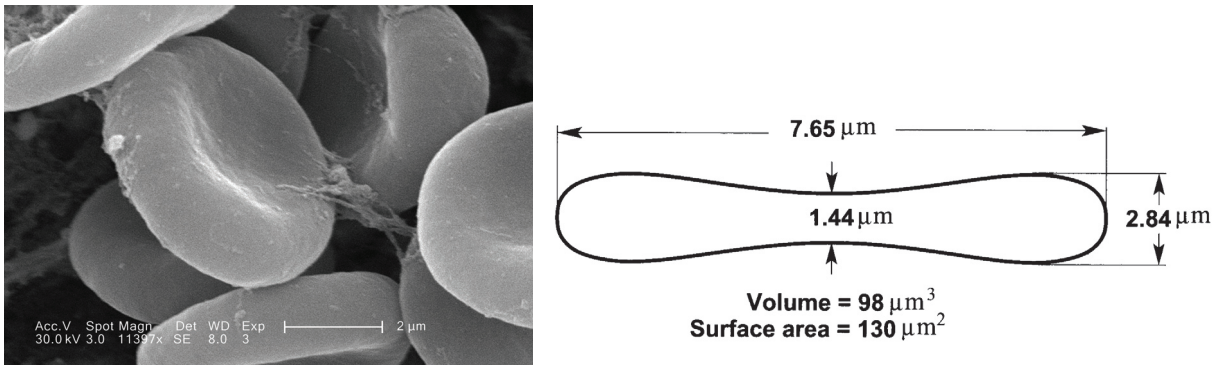

Figure 1.3: Left: a biconcave shape of RBC (Centers for Disease Control and Prevention, Public Health Image Library, Janice Carr). Right: Erythrocyte dimensions. Reprinted with permission from [104] – *A.M. Robertson et al., Oberwolfach Seminars, Birkhäuser Verlag Basel, 2008.*

Computational studies have been done in order to simulate this feature of blood flow which corresponds to the experimental observation of concentration of RBCs at the flow axis. Tsubota et al. [119] presented a two-dimensional particle model for blood flows between two parallel rigid plates. The moving particle semi-explicit (MPS) method was used to analyse the blood plasma flow. RBC was modelled as a deformable elastic membrane consisting of particles with the elastic energy depending on the distance between them, the angle between the neighbouring elements and the conservation of the membrane area. The simulation results demonstrated that RBCs concentrate near the flow axis forming the cell free layer near the boundaries. In a more recent work of Zhang et al. [140] another approach is used. Two-dimensional blood flow is simulated using the immersed-boundary lattice Boltzmann algorithm. Following Bagchi [12], RBCs are modelled as two-dimensional deformable biconcave membranes, while inter-cellular interactions are modelled using the Morse potential. In addition to the presence of the cell free layer it is shown that this layer thickness increases with cell deformability. In their work a known effect of erythrocytes migration toward the flow axis was observed, while platelets and their behaviour were not considered. AlMomani et al. [3] used the computational fluid dynamics (CFD) model to perform micro-scale simulations of platelet-RBC interactions in a shear flow. RBCs are assumed to be incompressible elliptical particles that retain elliptical shape during deformation by imposed shear stresses and platelets are assumed to be rigid particles of circular shape. The interaction between neighbouring particles is due to repulsive forces from a "soft" potential. It is shown that the concentration of platelets increases near the boundary, while erythrocytes are located near the flow axis. It was also found that the platelets behaviour is affected by the relative differences in the size of platelets and RBCs, but not by the differences in shape. Values of hematocrit were set to be 5%, 10% and 15%, which are lower than the normal hematocrit level in blood. Furthermore, it was observed that the migratory effect is absent at low hematocrit values (e.g., Ht = 5%), but occurs at higher values (e.g., Ht = 10%) and

becomes more evident as the hematocrit value increases. Another study [29] was devoted to a two-dimensional numerical investigation of the lateral platelet motion induced by RBCs. In that study a combination of the lattice Boltzmann method for fluid motion and Immersed Boundary method was used for the implementation of interaction between fluid and elastic objects suspended in or in contact with the fluid. A deformable elastic RBCs membrane was modelled following the Skalak [109] approach, while platelets were modelled as approximately rigid circular objects. Simulations were carried out for the following values of hametocrit: 0%, 20% and 40%. In the case of the RBC absence there was a negligible amount of lateral motion, however it was clearly shown that a near-wall increase in the platelet concentration occurs rapidly (within the first 400 ms) at both 20% and 40% hematocrits. In [15, 16] a three-dimensional discrete model that includes the simulation of blood as a suspension of erythrocytes and platelets in the blood plasma was used. Dissipative Particle Dynamics (DPD) method was used to carry out simulations of blood flow in a cylindrical vessel. RBCs were modelled as elastic highly deformable membranes. In contrast with [44], where a platelet is modelled as a rigid or almost rigid body, platelets were considered as elastic, although near spherical, membranes. The work investigates interaction between RBCs and platelets in flow and their distribution in the cross section of the vessel.

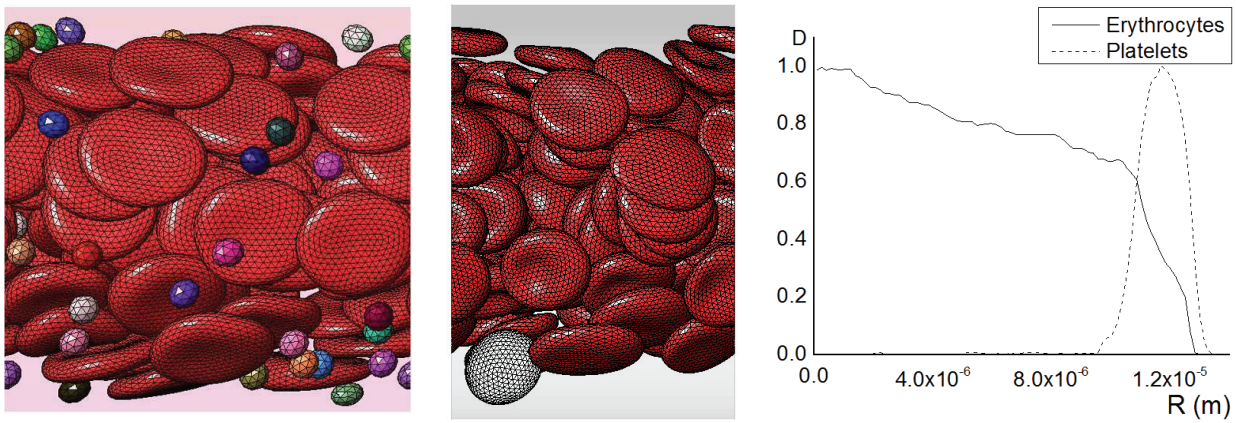

Figure 1.4: Left: Erythrocytes (larger cells) and platelets (smaller cells), suspended in blood plasma (not shown), in a flow through a 3D cylindrical channel, simulated by DPD method. Middle: Erythrocytes and a leukocyte (white cell) in a flow. Right: The distribution of erythrocytes and platelets as the function of distance from the flow axis. Reprinted with permission from [16] – *N. Bessonov et al., Mathematical Modelling of Natural Phenomena, Cambridge University Press, 2014.*

The distribution of platelets in flow, as shown in Figure 1.4, makes platelets naturally available at the site where they are most needed in the case of a vessel injury. Hence, the positioning of platelets makes the response of the organism to stop the bleeding, through the processes of platelet aggregation and blood coagulation, much more effective. Similarly, the distribution of leukocytes, which roll next to the vessel wall, makes it possible for them

to exit the vessel, by the process of extravasation, and to go to the site of tissue damage or infection. This mechanism is also relevant for atherosclerosis, as monocytes are recruited from the blood flow and integrated in the vessel wall intima in a response to the vessel wall inflammation.

1.2 Blood coagulation

1.2.1 Biological background

Hemostasis is a protective physiological mechanism that functions to stop bleeding upon vascular injury by sealing the wound with aggregates of specialized blood cells, platelets, and with gelatinous fibrin clots. Disorders of this system are the leading immediate cause of mortality and morbidity in the modern society. The most prominent of them is thrombosis, the intravascular formation of clots that obstruct the blood flow in vessels. The life-threatening clot formation is an ubiquitous complication or even a cause of numerous diseases and conditions such as atherosclerosis, trauma, stroke, infarction, cancer, sepsis and others. To provide only one example, 70% of sudden cardiac deaths are due to thrombosis [32] and they annually kill approximately 400 000 people in the United States only [88]. The development of thrombosis diagnostics and antithrombotic therapy is hampered by the incredible complexity of the hemostatic system comprising thousands of biochemical reactions of coagulation and platelet signalling that occur in the presence of the spatial heterogeneity, cell reorganization and blood flow. The most promising pathway to resolving this problem is systems biology, a novel multidisciplinary science aimed at quantitative analysis and understanding of complex biological systems with the help of high-throughput experimental methods and computational modelling approaches. During the last 20 years, the hemostasis system was a subject of intense interest in this field; reviews are available that describe these theoretical studies of blood coagulation [9, 93] and platelet-dependent hemostasis and thrombosis [93, 130, 135]. In recent years, computational modelling of coagulation has become a very widely used tool for investigating the mechanisms of drug action, optimization of therapy, analysis of drug-drug interaction at early stages (e.g. see recent examples for direct factor Xa inhibitors, novel anti-TFPI aptamer and recombinant activated factor VIII [90, 96, 108]). However, numerous problems remain. There is currently no mathematical model that could adequately account for all innumerable aspects of thrombosis and hemostasis; even the best ones usually use very unreliable assumptions about platelets, biochemistry and hydrodynamics. Finding a solution to these problems requires close cooperation between specialists in the hemostasis field and those in computational mathematics.

The two principal components of hemostasis are: i) platelets, specialized cells that adhere to the damaged tissue and form a primary plug reducing blood loss; ii) blood coagulation, a complex reaction network that turns fluid plasma into a solid fibrin gel to completely seal the wound. Maintaining the delicate balance between the fluid and the solid states of

blood is not simple, and a lion's share among the causes of mortality and morbidity in the modern society belongs to hemostatic disorders. The leading one is thrombosis, intravascular formation of platelet-fibrin clots that obstruct the blood flow in vessels. The major obstacle for the prevention and treatment of thrombosis is the insufficient knowledge of its regulation mechanisms. Platelet aggregation and blood coagulation are extremely complex processes. Attachment of platelets and their accumulation into a clot is regulated by mechanical interactions with erythrocytes and the vessel wall, by numerous chemical agents such as thrombin, or ADP, or prostaglandins, or collagen, as well as by an enormous network of intracellular signalling. Blood coagulation is only marginally simpler, including some fifty proteins that interact with each other and with the blood or vascular cells in approximately two hundred reactions in the presence of flow and diffusion.

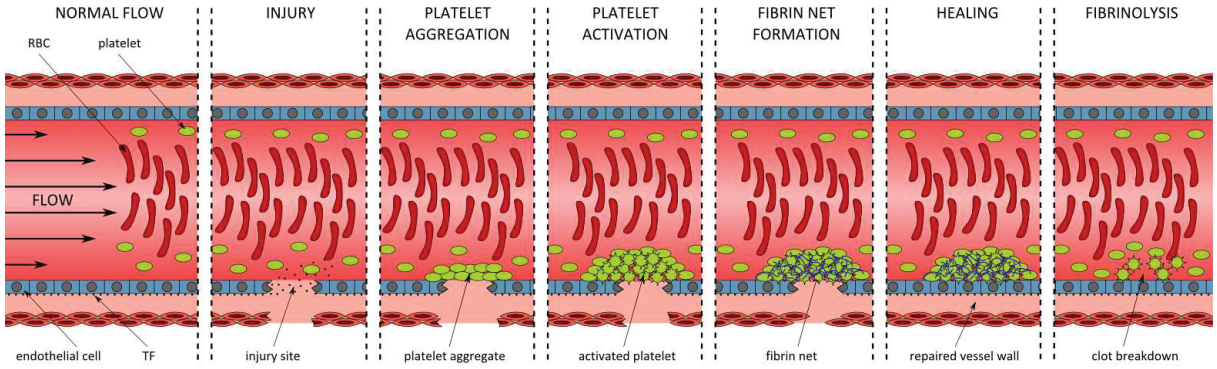

Figure 1.5: A simplified scheme showing the main stages of the process of injured vessel healing.

Although extensive research during the last decades has identified many key players in the hemostatic system, the regulation of hemostasis and thrombosis remains poorly understood. It is extremely difficult to relate a protein or a reaction in such a complex system to the functioning of the system as a whole. The most crucial unresolved problem is the very difference between hemostasis and thrombosis. All existing anticoagulants cannot tell them apart and target indiscriminately (that is why it is impossible to prevent coronary artery thrombosis simply by putting all persons in high risk groups on anticoagulation therapy: the possibility of death from external bleeding or a cerebral hemorrhage would become too high). If we knew these mechanisms, it would be possible to target them specifically in order to inhibit intravascular thrombi and prevent the blood vessel occlusion while leaving the hemostatic functions relatively intact. The most advanced and powerful pathway to decomposing complex systems in systems biology is developing a comprehensive mathematical model and then subjecting it to a sensitivity analysis in a sort of "middle-out" approach; an example of the modular decomposition for the blood coagulation cascade can be found in [94]. The most important problem hampering the application of this solution lies in the facet that thrombosis and hemostasis cannot be completely understood without combining all three essential elements: platelets, coagulation, and flow. Blood platelets form hemo-

static plugs and thrombi by aggregation. This process cannot proceed without flow, and is strongly dependent on the platelet-erythrocyte interaction in the presence of flow [112]. Blood coagulation is important for the platelet plug formation, because thrombin is one of the main activators of platelets ensuring clot/plug stability, and because the fibrin network solidifies the cell aggregate. In contrast, blood coagulation is strongly inhibited by flow. Active coagulation factors are removed from the site of injury to such a degree that no fibrin clot can be formed at a physiological arterial shear rate [107]. Therefore, the clot formation in the presence of a rapid flow requires platelets that mechanically protect coagulation from the flow, provide binding sites for coagulation factors and secrete substances that participate in coagulation such as fibrinogen, factor V, Xi, etc.

One of the most intriguing problems in the field of thrombosis is the problem of regulating the clot size. While the mechanisms of clot growth became well established during the last decade [64], it is not clear how and when a clot stops growing in order to avoid a complete vessel occlusion. One thing that is firmly established is that an occlusion does not always occur: while the popular experimental model of ferric-chloride induced damage of the carotid artery usually ends with occlusion [82], there is no occlusion in the laser-induced injury model of thrombosis in small arterioles [43]. Numerous hypotheses have been proposed to explain the mechanism by which the clot stops growing (e.g. the role of thrombomodulin [95]). One of the most intriguing ones is the role of fibrin clot - platelet clot interaction: it suggests the formation of a fibrin cap on the surface of the clot that prevents further the platelet accumulation [71]. However, the formation of fibrin on the surface of the clot is unlikely because of high shear rates that remove active coagulation factors [107]. In other words, the fibrin formation can occur only under the protection of platelets and this prevents the formation of the fibrin cap on the surface of the platelet clot.

Pathways. Blood coagulation is a complex process involving plasma proteins, called "coagulation factors", with the purpose to completely seal the wound. In the case of injury, the blood factors interact in a highly predetermined order, and it is because of this that the blood coagulation regulatory network is sometimes referred to as "the coagulation cascade". This series of interactions enables the transformation of a blood factor fibrinogen to its polymerized state called "fibrin polymer". The purpose of fibrin polymer is to reinforce a platelet aggregate at the injury site, making it more resistant and stronger, thus giving the injured tissue time to heal. Because of its function and structure the polymerized fibrin reinforcing the clot is often referred to as "the fibrin net". The coagulation factors are generally divided into two groups – zymogens and cofactors. The zymogens are inactive plasma proteins which are, in the presence of other enzymes, transformed to active enzymes. The cofactors are proteins which act as accelerators or catalysts for other enzymatic reactions. However, some blood factors cannot be classified neither as zymogens nor cofactors. One of these exceptions is fibrinogen which is transformed to fibrin, which has no enzymatic properties. Coagulation factors are referred to by a system of Roman numerals and when activated are denoted by the suffix $_a$.

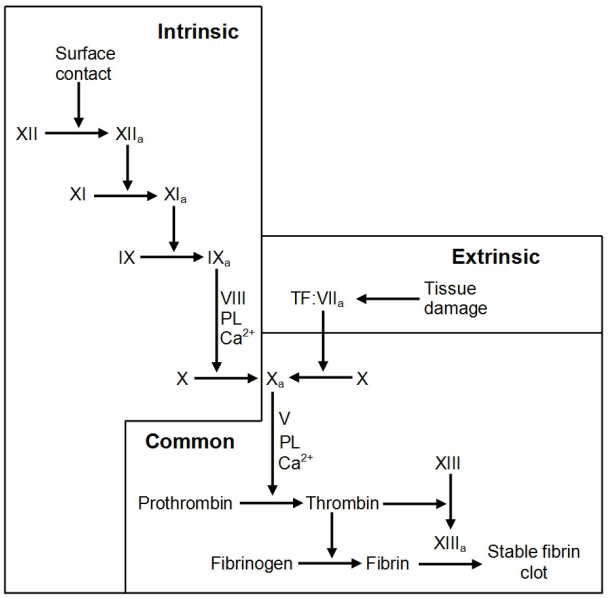

Figure 1.6: Coagulation pathways in vitro - extrinstic, intristic and common. Reprinted with permission from [92] – *C.J. Pallister and M.S. Watson, Scion Publishing Ltd, 2011.*

With a view to detecting abnormalities in blood clotting two different in vitro screening test were developed: in 1935 A.J. Quick et al described a method based on the prothrombin time (PT) [102], while in 1953 R.D. Langdell et al described another screening method based on the activated partial thromboplastin time (APTT) [79]. The two methods however yielded different observations about the process of blood coagulation. This led to the development of two distinct blood coagulation pathways – the extrinsic pathway for PT and the intrinsic pathway for APTT. Both pathways converge to a so called common pathway as shown in Figure 1.6. The main difference between the two pathways is in the way the blood coagulation is initiated. The intrinsic pathway is triggered by a contact of flowing blood with a negatively charged surface, such as glass, in which factor XII gets activated and the intrinsic reaction cascade is started. In the extrinsic pathway the process is initiated by tissue damage and with the release of tissue factor which forms a complex with both factor VII and factor VII$_a$. These complexes accelerate the activation of factor VII and with it the activation of factor X. In the common pathway, once the factor X gets activated it induces the production of trombin enzyme from prothrombin. Thrombin then acts as the enzyme in the transformation of fibrinogen to fibrin. As thrombin has multiple enzymatic activities, including direct activation of factors which are responsible for factor X activation, it also accelerates its own production resulting in an explosive increase in the rate of coagulation.

Although the classical model of coagulation pathway, consisting of intrinsic, extrinsic and common pathways, has been very important for understanding the results of laboratory screenings, it does not exist as such in vivo. Hence a new model was developed in order to

describe blood coagulation in vivo. The model consists of two phases – the initiation phase, followed by the amplification phase. The scheme of each phase is given in Figure 1.7. The main physiological activator of blood coagulation in vivo is tissue factor. It is expressed on sub-endothelial fibroblasts, injured vascular endothelium and activated monocytes. Hence, in the initiation phase the exposed tissue factor binds with activated factor VII_a to form a complex called "the extrinsic tenase complex". The complex activates factors IX and X in a low amount, substantial only for the initiation of a low rate of thrombin production. At this point the level of thrombin is still insufficient to sustain the generation of fibrin at a high rate, and instead it mediates in the activation of factors V and VIII. The formed extrinsic tenase complex is rapidly inactivated by the formation of a complex with factor X_a and by tissue factor pathway inhibitor (TFPI). In the amplification phase factors IX_a and $VIII_a$ bind to form the intrinsic tenase complex. The complex prompts the rapid generation of factor X_a, which is followed by the generation of another complex consisting of factors X_a, V_a, calcium ions and platelet phospholipid, called the prothrombinase complex. The prothrombinase complex induces prothrombin activation to form thrombin. As thrombin acts as the enzyme in the activation of factors V, VIII, XI, it also implicitly accelerates its own production. The generated thrombin enables the formation of fibrin from fibrinogen. Fibrin monomers are then polymerized in the presence of factor $XIII_a$, whose production is also induced by thrombin.

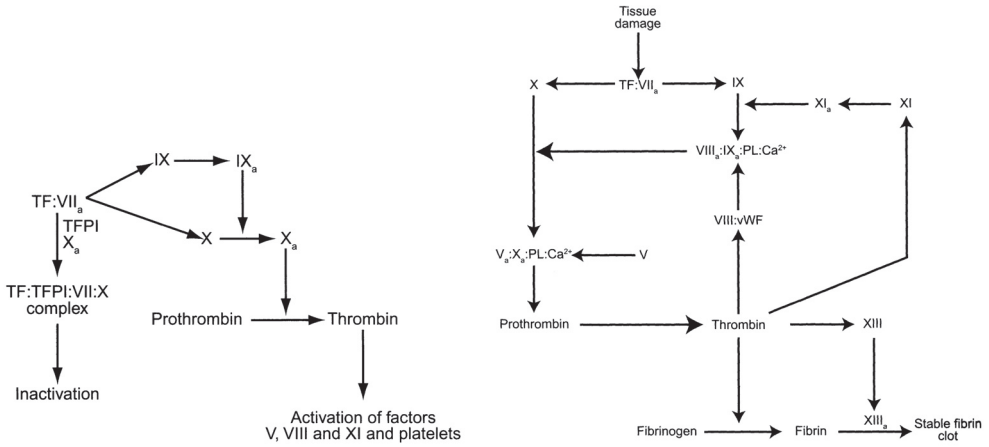

Figure 1.7: Coagulation pathways in vivo - initiation and amplification phase. Reprinted with permission from [92] – *C.J. Pallister and M.S. Watson, Scion Publishing Ltd, 2011.*

1.2.2 Modelling

From the modelling point of view, various approaches have been used so far in an attempt to model blood coagulation. They can be divided in three main groups - continuous models, discrete models and hybrid models. Continuous models rely on a vast mathematical knowledge

of partial differential equations and numerical schemes used to solve them [1, 4, 5, 17, 58, 115]. Using PDEs, the hydrodynamic flows can be precisely described, as well as the propagation of blood factors in the blood flow. On the other hand, clot growth depends highly on the blood cells – first of them being platelets as the primary building material of the clot, but also on erythrocytes which also strongly influence the blood flow, blood viscosity and the distribution of platelets in flow. Due to the more discrete nature of the clot formation, continuous models were unable to capture cell interactions and processes like the rupture of a clot. In discrete approaches the most of the used methods consider the simulated medium to consist of particles, usually representing atoms, molecules, small lumps of the medium or cells. This allows the description of a heterogeneous medium while keeping the ability to approximate its hydrodynamic properties in the flow [99, 119]. The difficulty arises with the modelling of the complex regulatory network of proteins involved in coagulation and their transport in the flow. Here comes the idea of developing hybrid models which would use both continuous and discrete methods with the intention of coupling their strengths and avoiding as much as possible their downfalls. Among the hybrid models various approaches have been used, each of them taking their own ratio of continuous and discrete parts. A number of hybrid methods use the continuous concept to model blood flow and propagation of blood factors in it, while the discrete concept is used to model blood cells and interactions between them. In [51, 98, 111, 131, 132, 133, 134] the blood flow is described by Navier-Stokes equations. The motion of blood cells in the blood flow then follows from the calculated velocity field. As the flow simulation domain changes because of the clot development, the Immersed Boundary (IB) method is often used. The protein cascade is described with a system of differential equations, each equation describing a concentration of a single blood factor. Blood cells and their interactions are modelled with a discrete method like Cellular Potts Method (CPM) [131, 132, 133, 134] or with the method of Subcellular Elements (SCE) [111]. Another hybrid approach is to model the blood flow (blood plasma and blood cells) with a discrete method and to model the regulatory network of blood factors by a system of PDEs. One of the early works applying this method is [49].

Another important aspect of modelling blood coagulation concerns the biological assumptions of the model. In the past, one of the main assumptions was that platelets are first activated and then they begin to aggregate [49, 50, 64, 65, 99, 98, 131, 132, 133, 134]. Platelet activation can occur either because of their interaction with other activated platelets [98, 99] or with biochemical substances in blood plasma [49, 50, 131, 132, 133, 134]. However, recent results show that activation may not precede aggregation [65, 66, 67, 68, 69, 77, 138]. Platelet activation is not instantaneous and it can take some time (from several seconds up to one minute according to various estimates [53]), while platelet aggregation begins right after the injury. Moreover, if activation happens before aggregation, then it should occur at some distance from the injury site in the direction against the flow. This assumption implies that the biochemical compounds, which activate platelets, diffuse in the direction opposite to the flow. If the flow speed is sufficiently high, this assumption becomes unrealistic. Thus we come to the conclusion that platelets can aggregate in the clot without activation. This is confirmed by biological observations [65, 66, 67, 68, 69, 77, 138]. First, platelets are con-

nected by weak reversible bonds due to GPIb receptors. A new platelet coming from the flow can roll at the surface of the clot, slowing down because of these weak reversible connections. When it stops, other receptors (integrin) create more stable connections due to platelet activation. Finally, platelets can be covered by fibrin net, which fixes them completely in the clot. Thus we consider another concept of clot growth where platelet activation does not precede platelet aggregation but, on the contrary, follows the first stage of clot formation. One of the main objectives of this work is to test this hypothesis in numerical simulations.

The previously mentioned mechanism of the clot growth arrest (see above) is described and tested in this work. At the first stage of the clot growth, platelets aggregate without activation, providing a possibility for chemical reactions to start. Indeed, platelet aggregation in the growing clot essentially decreases the flow velocity inside it, and chemical compounds are not removed by the flow, or at least, removed to the lesser extent [115]. Coagulation reactions result in the development of the fibrin net which covers platelets inside the growing clot. On one hand, it reinforces platelet attachment in the clot, on the other hand, platelets covered by fibrin cannot attach other platelets, and fibrin itself is a poor substrate that does not support further formation of thrombi [71]. Since coagulation reactions occur inside the clot but not close to its outer surface because of the flow, the growing clot consists of two parts: the inner part covered with fibrin and the outer part without fibrin. Platelets are aggregated due to reversible connections in the outer part. If the clot becomes sufficiently large, flow pressure can break it and remove the outer part. Only the inner part covered by fibrin remains. It does not attach new platelets, and the clot stops growing.

1.3 Atherosclerosis

1.3.1 Biological background

Atherosclerosis is a syndrome in which an artery wall thickens as a result of the accumulation of cholesterol and triglyceride. It is a slowly developing cardiovascular disease with often fatal consequences. This is mainly because atherosclerosis remains asymptomatic, often for decades, before reaching the chronic stage. Chronic atherosclerosis is the most common cause of cardiovascular diseases, namely: heart attacks, strokes and peripheral vascular diseases. This group of diseases is the leading cause of deaths worldwide. In atherosclerosis the reasons for such a high mortality are numerous. First of them being the lack of understanding of the processes related to its development. An additional reason lays in the long period during which disease develops without showing any characteristic and easily noticeable symptoms. In many cases the first clear symptom is either a heart attack, a stroke, or a sudden cardiac death (death within one hour of the onset of acute symptoms). Also, due to the limited understanding of the atherosclerosis syndrome and its asymptomatic nature, it is rather difficult to detect the disease in its early stages, assess the stage of the disease and to stop or cure it. Therefore, further investigation of the disease is of a high importance.

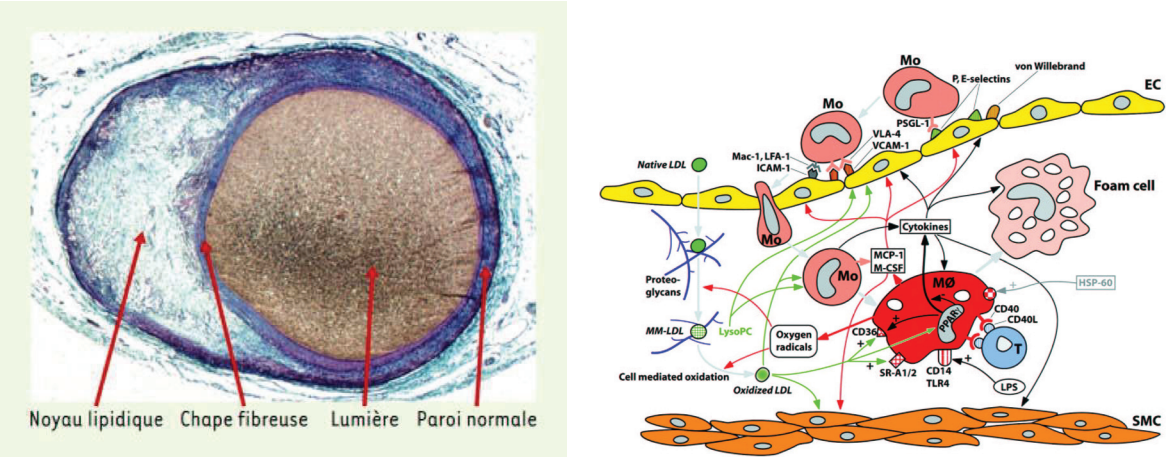

Figure 1.8: Left: Blood vessel and atherosclerotic plaque in the cross section. Reprinted with permission from [83] – *Z. Mallat and A. Tedgui, Medecine/Sciences, Editions EDK/Groupe EDP Sciences, 2004.* Right: Schematic of the regulatory network of atherosclerosis. Reprinted with permission from [91] – *B. Østerud and E. Bjørklid, Physiological Reviews, American Physiological Society , 2003.*

The schematic of the regulatory network of atherosclerosis is shown in Figure 1.8 (right), while the process of development of atherosclerotic plaque is depicted in 1.9. Low-density lipoproteins (LDL) enable the transport of different fat molecules, including cholesterol, phospholipids and triglycerides, from the liver to the tissues of the body. When a cell requires additional cholesterol it synthesizes the necessary LDL receptors, and inserts them into the plasma membrane. LDL particles in the bloodstream bind to these extracellular LDL receptors. However, LDL can enter the intima of the vessel wall from the blood flow. Once in the vessel wall, LDL particles and their content become more susceptible to oxidation by free radicals. The damage caused by the oxidized LDL molecules triggers a signal that attracts monocytes from the blood stream. Monocytes then enter the blood vessel intima by a process of extravasation (movement of leukocytes or monocytes from the circulatory system towards the site of tissue damage or infection). There they differentiate to macrophages, cells whose function is to engulf cellular debris and pathogens in a process called phagocytosis, and to brake them down using enzymes. After differentiation, macrophages absorb the oxidized LDL. However, as they are unable to process the oxidized LDL, they eventually transform into so-called foam cells (lipid-laden cells), which slowly accumulate in the vessel wall. A large amount of foam cells at the same place in the vessel wall has a twofold effect on the vessel: first, it thickens the vessel wall and causes the narrowing of the lumen of the vessel, and second, it starts a chronic inflammatory reaction. The chronic inflammatory reaction is an auto-amplification process which begins when foam cells start to secrete pro-inflammatory cytokines (e.g., TNF-α, IL-1). Pro-inflammatory cytokines increase endothelial cells activation, promote the recruitment of new monocytes and support the production of new pro-inflammatory cytokines. This auto-amplification phenomenon is

compensated by an anti-inflammatory phenomenon mediated by the anti-inflammatory cytokines (e.g., IL-10). The anti-inflammation process is twofold: biochemical and mechanical. In the biochemical anti-inflammation part of the process the anti-inflammatory cytokines inhibit the production of pro-inflammatory cytokines. The mechanical anti-inflammation consists of the proliferation and the migration of smooth muscle cells to create a fibrous cap over the lipid deposit, and of the formation of atherosclerotic plaque. The fibrin cap isolates the lipid deposit from the blood flow. Potential necrotic death of foam cells in the lipid deposit results in the formation of a necrotic center of atherosclerosis and significantly stimulates the inflammatory reaction. The thickening of the vessel wall and the formation of the hard fibrous cap change significantly the geometry of the vessel. As plaque grows it narrows the vessel lumen, which increases the flow pressure on the plaque and its fibrous cap. Because of the increased pressure in cases of a large plaque, the fibrin cap can break and release tissue factor and the contents of the plaque in the blood flow. In the case of the plaque rupture, its solid parts can go to the blood stream and cause a stroke or a heart attack. The rupture also induces coagulation at the site where the vessel lumen is already narrowed by the plaque, further increasing the stenosis. Additionally, as it occurs on the less elastic fibrous cap, there is an increased probability of clot rupture and the formation of embolus with fatal consequences.

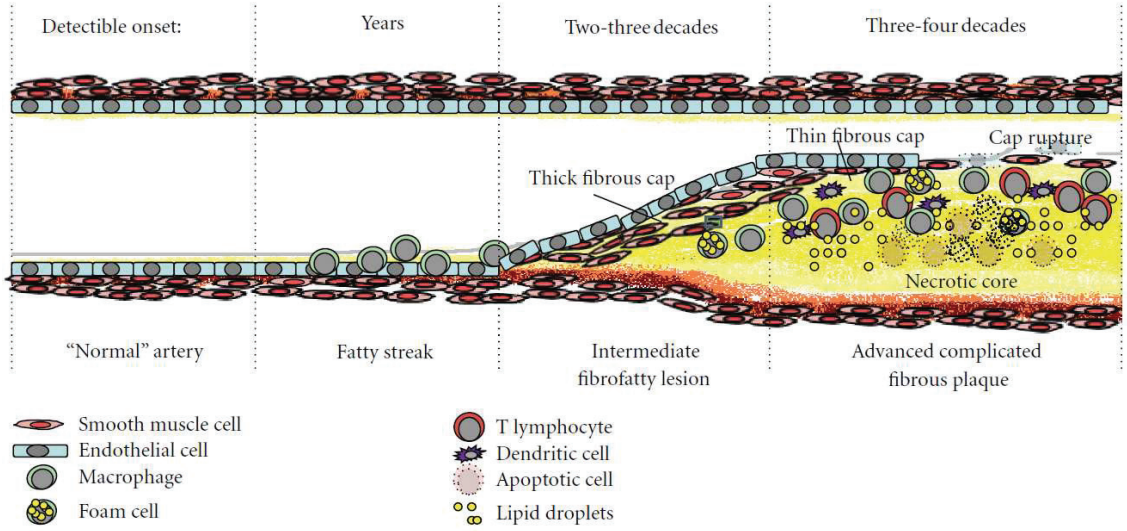

Figure 1.9: Schematic of the process of atherosclerotic plaque development. Reprinted with permission from [10] – *M.V. Autieri, ISRN Vascular Medicine, Hindawi, 2012.*

1.3.2 Modelling

The development of atherosclerosis is closely related to the characteristics of the blood flow, the composition of blood, the distribution of blood cells (especially monocytes), as well as to the process of blood coagulation. More precisely, the vessel wall thickens as monocytes, which

roll on the inner surface of the vessel, enter the vessel wall intima in a response to the bad cholesterol accumulation. Furthermore, at a chronic stage of atherosclerosis the thickening of the vessel wall can be severe and result in a remodelling of the vessel and significant changes in the flow configuration at the inflammation site. Due to the vessel remodelling the stress from the flow on the vessel wall at the inflammation site can significantly increase, leading to a rupture of the thrombotic plaque. The parts of the ruptured plaque can lead to a stroke or a heart attack. Additionally, the blood coagulation process will begin and a clot will form at the inflammation site, increasing further the stenosis of the vessel. In this case, the otherwise normal coagulation process can be compromised by the altered vessel wall properties (plaque) and stenosis, possibly leading to further complications such as clot rupture or vascular occlusion. Because of this the modelling of atherosclerosis is closely related to modelling of the blood flow, blood cells, and blood coagulation.

Another aspect of studying the development of atherosclerosis is related to chronic inflammation. The theory of atherosclerosis as an inflammatory disease is well accepted [35], although the process is not yet completely understood and other theories have also been developed in the last decades. The inflammatory aspect of atherosclerosis makes it suitable for modelling and studying with partial differential equations. This approach allows to describe the inflammation propagation as a wave solution of a parabolic partial differential equation. Depending on the initial conditions, the system can stay in the disease free equilibrium, or a travelling wave propagation can occur, which corresponds to a chronic inflammatory response.

In the simplest, one-dimensional model atherosclerosis can be represented by a system of two ordinary differential equations [35, 121]:

$$\begin{aligned} \frac{dM}{dt} &= f_1(A) - \lambda_1 M, \\ \frac{dA}{dt} &= f_2(A)M - \lambda_2 A, \end{aligned} \tag{1.1}$$

where M denotes the concentration of monocytes and macrophages, and A the concentration of cytokines secreted by immune cells, $x \in [0, L]$. The functions $f_1(A)$ and $f_2(A)$ describe the qualitative properties of the system described above:

$$\begin{aligned} f_1(A) &= \frac{\alpha_1 + \beta_1 A}{1 + A/\tau_1}, \\ f_2(A) &= \frac{\alpha_2 A}{1 + A/\tau_2}. \end{aligned} \tag{1.2}$$

The function $f_1(A)$ describes the rate at which monocytes are attracted to the vessel wall by pro-inflammatory cytokines. $\alpha_1 = f_1(0)$ corresponds to the amount of monocytes attracted due to the presence of oxidized LDL. β_1 represents the auto-amplification effect that

occurs as monocytes secrete more pro-inflammatory cytokines that attract even more monocytes to the inflammation site. The factor $1 + A/\tau_1$ represents the mechanical obstruction of the recruitment of new monocytes due to the formation of a fibrous cap, where τ_1 denotes the characteristic time of the fibrous cap formation. Term $f_2(A)M$ modells the cytokine production rate, where $\alpha_2 A$ describes the auto-promoted secretion of pro-inflammatory cytokines, and $1 + A/\tau_2$ describes the inhibition of the pro-inflammatory cytokine secretion by anti-inflammatory cytokines. Here τ_2 represents the time that is necessary for the inhibition to commence. λ_1 and λ_2 denote the degradation rates of immune cells and cytokines respectively, while d_1 and d_2 describe the corresponding diffusion (or cell displacement) rates in the vessel intima.

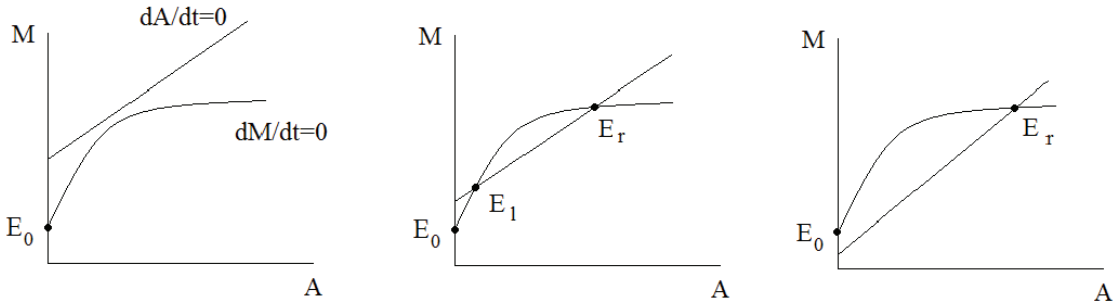

Figure 1.10: Three possible situations depending on the level of ox-LDL: one stable stationary point (left), three stationary points, two of them are stable (middle), two stationary points, stable and unstable (right). Reprinted with permission from [35] – *N. El Khatib et al., Mathematical Modelling of Natural Phenomena, Cambridge University Press, 2007.*

The system (1.1)-(1.2) can have one to three stationary points, depending on the level of oxidized LDL. The three possible situations are shown in Figure 1.10. The first situation (Figure 1.10 (left)) corresponds to the case when α_1 is small, i.e. there is a low initial concentration of oxidized LDL. It this case E_0 is the only stationary point, and it is stable, which means that chronic inflammatory reaction does not occur. In the second situation (Figure 1.10 (middle)) the value of α_1 is intermediate, and there are three stationary points: E_0 and E_r are stable, while E_l is unstable. In this bistable case the system will reach E_0 for low, and E_r for high initial values. Therefore, the chronic inflammation can occur only if the initial values are larger than a certain threshold. The third situation (Figure 1.10 (right)) corresponds to the case when the value of α_1 is large. In this case E_0 is an unstable and E_r is a stable point. This is a monostable case in which even a small perturbation from the non-inflammatory state E_0 leads to the chronic inflammation state E_r.

If the diffusion of cytokines and the random displacement of monocytes and macrophages in the intima are taken into account, from model equations (1.1) the following equations are obtained:

$$\begin{aligned} \frac{\partial M}{\partial t} &= d_1 \frac{\partial^2 M}{\partial x^2} + f_1(A) - \lambda_1 M, \\ \frac{\partial A}{\partial t} &= d_2 \frac{\partial^2 A}{\partial x^2} + f_2(A) M - \lambda_2 A, \end{aligned} \tag{1.3}$$

where d_1 is the cell displacement coefficient, d_2 is the cytokine diffusion coefficient, and the definition of functions $f_1(A)$ remains unchanged $f_2(A)$ (equations (1.2)). The existence of the travelling wave solution for the reaction diffusion system (1.2)-(1.3) is proven in [35].

Although, the inflammatory reaction in atherosclerosis occurs in the vessel intima, the one-dimensional model (equations (1.2) and (1.3)) does not take into account the process of extravasation, by which monocytes from the blood flow enter the vessel intima. Hence, a two-dimensional model was proposed in [36, 37, 38], where the recruitment of monocytes is described in terms of a boundary condition. The domain of the model is an infinite strip $\Omega = \{(x, y) : -\infty < x < \infty, 0 \leq y \leq h\}$ which represents again the vessel intima, where h denotes its thickness. The model is then described by the following system of equations:

$$\begin{aligned} \frac{\partial M}{\partial t} &= d_M \Delta M + \beta M, \\ \frac{\partial A}{\partial t} &= d_A \Delta A + f(A) M - \gamma A + b_s. \end{aligned} \tag{1.4}$$

with the corresponding boundary conditions:

$$\begin{aligned} y = 0: \quad & \frac{\partial M}{\partial y} = 0, \qquad \frac{\partial A}{\partial y} = 0, \\ y = h: \quad & \frac{\partial M}{\partial y} = g(A), \quad \frac{\partial A}{\partial y} = 0. \end{aligned} \tag{1.5}$$

The boundary conditions at $y = 0$ are homogeneous Neumann as they describe the condition with no flux of monocytes and cytokines through the boundary. At $y = h$ the flux of monocytes is non-zero and depends on the level of cytokines, while there is again no flux of cytokines. The system (1.4)-(1.5) is a reaction-diffusion system in an unbounded domain with non-linear boundary conditions. As such the classical results for semi-linear parabolic problems (Volpert et al. 2000) [122] are not applicable to this problem. Therefore, in [37, 38] the existence of a travelling wave is proven in the monostable case. Additionally, it is numerically shown [37, 38] that as h goes to zero, the solution of the 2D problem converges to the solution of the above mentioned 1D problem [35].

1.4 Main results of the thesis

The main subject of this thesis is the modelling of blood flow related phenomena by using hybrid models. More precisely, a mathematical hybrid model is developed to study the biological process of blood coagulation. The second chapter contains the description of a discrete method, called Dissipative Particle Dynamics (DPD), which is a particle method used to model the flow of blood plasma. The description of the method is followed by a description of integration schemes for equations of motions, containing a novel integration scheme for DPD, which allows a significant increase of the time step for DPD. In Section 2.2 methods of measuring physical properties in simulations are explained. As in DPD method modelling of boundaries can pose a problem, Section 2.3 contains descriptions of multiple ways to implement no-slip boundary conditions in DPD. The final section of the first chapter (Section 2.4) discusses the modelling of the erythrocyte membrane in DPD for both 2D and 3D case.

The third and fourth chapter concern the modelling of blood coagulation in flow. In the Chapter 3 a discrete model of clot growth in flow is described. In the model, blood plasma and platelets are modelled by the DPD method, while the platelet aggregation is modelled by Hooke's law. The model is used to study several approaches to modelling different inter-platelet bonds. Furthermore, it is used for a preliminary study of a possible mechanism of growth arrest of the platelet clot, which will be further studied in hybrid models. Chapter 4 describes two hybrid (discrete-continuous) models. Section 4.1 describes the first hybrid model. The discrete part of the model uses DPD to describe platelets suspended in the plasma flow, while the continuous part consists of a single reaction-diffusion-advection equation which describes the concentration of fibrin. The model is used to calibrate parameters and methods used to combine the discrete and the continuous parts of the model, as well as to study the interaction between the platelet aggregate and a blood factor concentration in flow. In Section 4.2 the second hybrid model is described. Instead of the single reaction-diffusion-advection equation, the blood coagulation pathways are modelled by a system of three equations. The system simulates the main characteristics of the coagulation cascade: the self-accelerated thrombin production from prothrombin, the influence of thrombin concentration on the transformation of fibrinogen to fibrin, and the influence of the flow on concentrations of blood factors. The model is used to study the influence of the platelet clot formation on the blood factor concentrations in flow. It showed the importance of the interaction between the platelet aggregation and coagulation pathways. Since the flow velocity is small inside the platelet clot, it is possible for the coagulation cascade to begin and to reinforce the growing aggregate by the formation of a fibrin network. The pressure from the blood flow removes the outer parts of the platelet clot and eventually stops it growth since the platelets covered by fibrin cannot attach new platelets [71]. Thus we suggest a possible mechanism how platelet clot stops growing. It is different from the mechanism which stops the coagulation cascade in blood plasma, though they interact with each other. The end of Section 4.2 contains simulation results of clot growth in vessels of different diameters and in

flows of different wall shear rates, obtained by use of the second hybrid model.

The fifth chapter is devoted to the mathematical analysis of a model of chronic inflammation related to atherosclerosis. Previously it was shown that the inflammation propagates as a reaction-diffusion wave whose properties depend on the level of the bad cholesterol in blood [38]. In this thesis we study a model problem which describes the propagation of a reaction-diffusion wave in the 2D case with nonlinear boundary conditions. The Leray-Schauder method and a priori estimates of solutions are used in order to prove the existence of waves in the bistable case.

The thesis concludes with a section containing all the relevant references used in this work, and the Appendix section containing a description of the numerical implementation of the models developed in this work. These details are gathered to the independent section in order to separate them from model descriptions and results, and to make the structure of the thesis easier to follow. However, the models of blood flows that describe blood as a plasma suspension of blood cells, as well as the blood coagulation models developed in this work, are computationally very expensive. Hence, in the scope of the work described in the thesis a substantial effort was directed to optimization and parallelization of the numerical implementation.

Chapter 2

Dissipative Particle Dynamics

2.1 Description

In order to simulate a complex fluid, a numerical method has to describe the structure of the fluid, usually on the microscopic level, for which classical continuous and discrete methods are not suitable. Continuous approaches, like Navier-Stokes equations, although useful for modelling simple fluids, lack the ability to model the composite structure of complex fluids. On the other hand, Molecular Dynamics (MD) as a classical discrete approach, although able to capture the complex structure of the fluid, is inappropriate because it becomes too expensive to study macroscopic phenomena on a larger scale. Hence, so-called meso-scale methods were developed. In order to describe a certain complex structure on a micro-scale and to still be able to study its effects on a macro-scale the meso-scale methods use "coarse-graining" - the process of representing a system with fewer degrees of freedom than those actually present in the system [41, 105]. Many of such methods are not strictly mathematically derived but are rather constructed in order to satisfy certain conservation laws and symmetries that are considered to be essential for the observed phenomena. Since the interest in this area began thirty years ago, a lot of meso-scale methods and their specialised variants were developed and a lot of effort was done in order to succumb their potential flaws, as well as to justify their definition by deriving them from continuous methods and conservation laws. One of the most successful and generally used methods is Dissipative Particle Dynamics (DPD) which was first described by Hoogerbrugge and Koelman in 1992 [61, 105]. By its definition DPD is a mass and momentum conservative method, and it produces a correct hydrodynamic behaviour, which was verified both analytically and by simulations. In its original description the DPD method does not conserve the energy of the system, due to its definition of dissipative and random forces. However, a rigorous theoretical justification was later given by Español and Warren who derived the correct fluctuation dissipation relation for the friction and noise terms in 1995. In the same year, Español derived the hydrodynamic equations for the mass and momentum density fields. Since then

the interest in DPD continued to increase, leading to further justifications of the method, establishing relations to other methods like Smoothed Particle Hydrodynamics [39, 40, 105], to the introduction of new integration methods for equations of motion, such as the modified Velocity-Verlet algorithm [56], and resulting in a vast number of applications. The behaviour of DPD method, as well as its suitability for the problem of fluid simulation is well described in literature [44, 45, 56, 72, 105]. In [44, 45] DPD simulation results are compared with the results obtained by using continuous methods (Navier-Stokes and Stokes equations) for Couette, Poiseuille, square-cavity and triangular-cavity flows.

In this work we use the DPD in the form described in literature [44, 56, 72]. As in other meso-scale methods, each particle of the system describes some small volume of a simulated medium rather than an individual molecule. The method implies the conservative, dissipative and random forces acting between each two particles (pair-wise):

$$\mathbf{F}_{ij}^{C} = F_{ij}^{C}(r_{ij})\hat{\mathbf{r}}_{ij}, \tag{2.1}$$

$$\mathbf{F}_{ij}^{D} = -\gamma\omega^{D}(r_{ij})(\mathbf{v}_{ij}\cdot\hat{\mathbf{r}}_{ij})\hat{\mathbf{r}}_{ij}, \tag{2.2}$$

$$\mathbf{F}_{ij}^{R} = \sigma\omega^{R}(r_{ij})\frac{\xi_{ij}}{\sqrt{dt}}\hat{\mathbf{r}}_{ij}, \tag{2.3}$$

where $\mathbf{r}_i$ is the vector of position of the particle i, $\mathbf{r}_{ij} = \mathbf{r}_i - \mathbf{r}_j$, $r_{ij} = |\mathbf{r}_{ij}|$, $\hat{\mathbf{r}}_{ij} = \mathbf{r}_{ij}/r_{ij}$, and $\mathbf{v}_{ij} = \mathbf{v}_i - \mathbf{v}_j$ is the difference between velocities of two particles, γ and σ are coefficients which determine the strength of the dissipative and the random force respectively, while ω^D and ω^R are weight functions; ξ_{ij} is a normally distributed random variable with zero mean, unit variance such that $\xi_{ij} = \xi_{ji}$, and dt is the time step. The conservative force is given by the equality

$$F_{ij}^{C}(r_{ij}) = \begin{cases} a_{ij}\,(1 - r_{ij}/r_c) & \text{for } r_{ij} \le r_c, \\ 0 & \text{for } r_{ij} > r_c, \end{cases} \tag{2.4}$$

where a_{ij} is the conservative force coefficient between particles i and j, and r_c is the cut-off radius.

The random and dissipative forces form a thermostat. If the following two relations are satisfied, the system will preserve its energy and maintain the equilibrium temperature [42]

$$\omega^{D}(r_{ij}) = \left[\omega^{R}(r_{ij})\right]^2, \qquad \sigma^2 = 2\gamma k_B T, \tag{2.5}$$

where k_B is the Boltzmann constant and T is the temperature. The weight functions are determined by:

$$\omega^R(r_{ij}) = \begin{cases} (1 - r_{ij}/r_c)^k & \text{for } r_{ij} \leq r_c, \\ 0 & \text{for } r_{ij} > r_c, \end{cases} \tag{2.6}$$

where $k = 1$ for the original DPD method, but it can be also varied in order to change the dynamic viscosity of the simulated fluid [44]. The reason for scaling the random force (equation (2.3)) by factor $1/\sqrt{dt}$ is to eliminate the displacement due to Brownian motion [57]. This preserves the momentum and leads to a correct description of hydrodynamics.

The motion of particles is determined by Newton's second law of motion:

$$d\mathbf{r}_i = \mathbf{v}_i dt, \qquad d\mathbf{v}_i = \frac{dt}{m_i} \sum_{j \neq i} \left(\mathbf{F}_{ij}^C + \mathbf{F}_{ij}^D + \mathbf{F}_{ij}^R \right), \tag{2.7}$$

where m_i is the mass of the particle i.

The simplest way to integrate the equations of motion (2.7) is by use of Euler method:

$$\mathbf{v}_i^{n+1} = \mathbf{v}_i^n + \frac{1}{m_i} \mathbf{F}_i \left(\mathbf{r}_i^n, \mathbf{v}_i^n \right) dt, \tag{2.8}$$

$$\mathbf{r}_i^{n+1} = \mathbf{r}_i^n + \mathbf{v}_i^{n+1} dt, \tag{2.9}$$

where indices n and $n + 1$ denote time steps, and

$$\mathbf{F}_i = \sum_{j \neq i} \left(\mathbf{F}_{ij}^C + \mathbf{F}_{ij}^D + \mathbf{F}_{ij}^R \right). \tag{2.10}$$

Instead of the conventional Euler method, a more refined method, called "modified velocity-Verlet method", can be used [2, 56]. First described by Groot and Warren in 1997 [56], it is more accurate and it allows a certain increase in time step dt, thus reducing the computational cost of the simulation. The discretization of the equations (2.7) by modified velocity-Verlet scheme is given by:

$$\mathbf{r}_i^{n+1} = \mathbf{r}_i^n + \mathbf{v}_i^n dt + \frac{1}{2} \mathbf{a}_i^n dt^2, \tag{2.11}$$

$$\mathbf{v}_i^{n+\frac{1}{2}} = \mathbf{v}_i^n + \frac{1}{2} \mathbf{a}_i^n dt, \tag{2.12}$$

$$\mathbf{a}_i^{n+1} = \frac{1}{m_i} \mathbf{F}_i \left(\mathbf{r}_i^{n+1}, \mathbf{v}_i^{n+\frac{1}{2}} \right), \tag{2.13}$$

$$\mathbf{v}_i^{n+1} = \mathbf{v}_i^{n+\frac{1}{2}} + \frac{1}{2} \mathbf{a}_i^{n+1} dt, \tag{2.14}$$

where a_i^n denotes the acceleration of the particle i at the n^{th} time step.

2.2 2D Poiseuille flow

2.2.1 Measurements

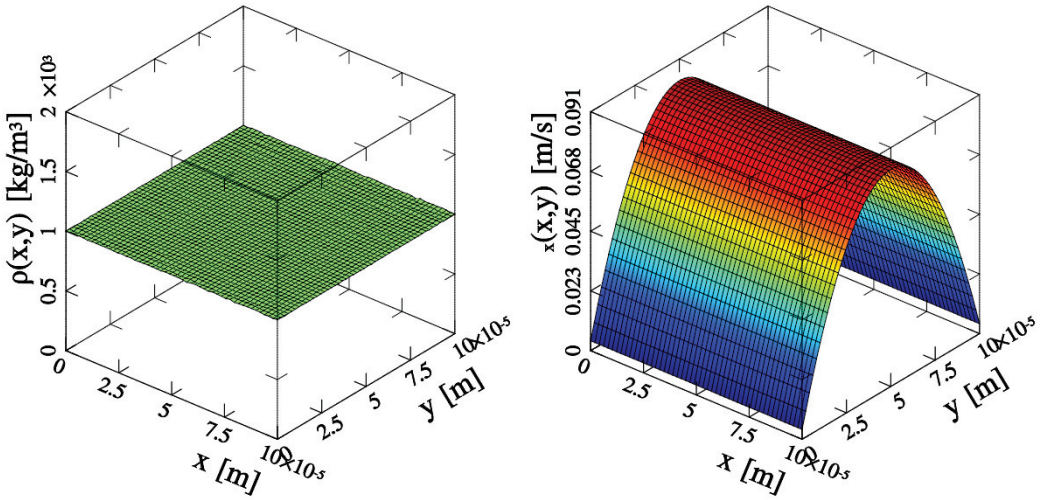

Figure 2.1: An example of density (left) and velocity (right) profiles obtained by a simulation of Poiseuille flow with DPD method.

As DPD is used in this work to model blood plasma flow for purposes of studying blood coagulation in vivo, the spatial domain represents a section of a blood vessel. Hence, in the three-dimensional (3D) case the spatial domain is a cylinder, while in two dimensions (2D) the spatial domain represents a cross-section of the vessel along its axis. The dimensions of the spatial domain are defined accordingly to the diameter D and the length L of the simulated vessel. The blood plasma, due to its composition (92% of water), is considered in this model to have properties similar to those of water, i.e. it is viscous and incompressible. The flow is induced by a constant external force or a pressure gradient in the direction along the vessel axis. The effect of pressure waves generated by the heart in systole moves is not considered within this study. Following the Poiseuile law for laminar flows (a solution of Navier-Stokes equations), the described system should yield a parabolic velocity profile. In the 2D case the velocity profile is given by:

$$u_x(y) = \frac{f_x - \frac{\partial p}{\partial x}}{2\mu} \left(yD - y^2 \right), \tag{2.15}$$

where x and y are coordinates of the Cartesian coordinate system with the x-axis along the vessel wall and being parallel to the vessel axis, u_x is the x component of a velocity vector $\vec{u}$, f_x is the x component of a the volume force vector $\vec{f}$, p is the pressure, and μ is the dynamic

viscosity of blood plasma. In 3D case the velocity profile is given by:

$$u_x(r) = \frac{f_x - \frac{\partial p}{\partial x}}{4\mu} \left(R^2 - r^2\right), \tag{2.16}$$

where x and r are the coordinates of the cylindrical coordinate system in which x-axis is along the vessel axis.

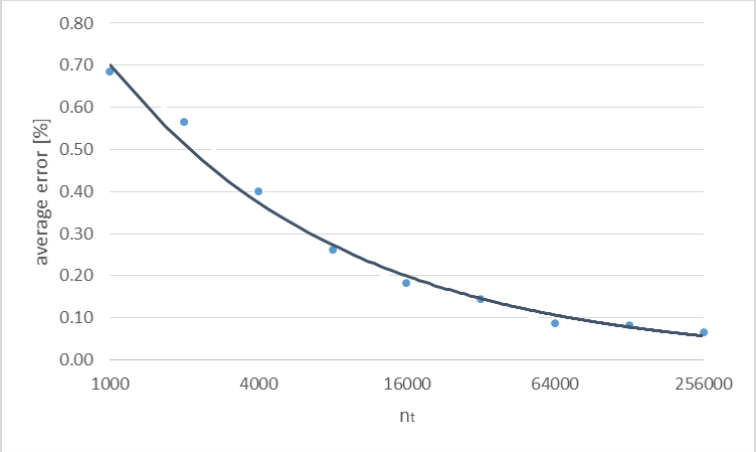

Figure 2.2: Convergence of density profile towards the uniform density as the numbers of measured steps n_t increases. The horizontal axis denotes the number of measured steps, while the vertical axis denotes the average difference between the measured and analytical density.

In order to obtain density and velocity profiles of a medium simulated by DPD particles one has to apply spatial and/or temporal averaging. For that purpose a spatial subdivision of the domain with some uniform step dx in directions of all coordinates is defined. During some number of time steps n_t, the presence of particles and their velocities is summarized for each spatial element of the subdivision, i.e. $S_{ij} = [x_i, x_i + \Delta x\rangle \times [y_j, y_j + \Delta x\rangle$ in the 2D case, or $S_{ij} = [x_i, x_i + \Delta x\rangle \times [r_j, r_j + \Delta x\rangle$ in the 3D case. In order to obtain the velocity profile, for each spatial element the mean velocity is calculated by dividing its total velocity by the number of particles observed in that element. To obtain the density profile, for each spatial element the number of observed particles is divided by the number of time steps n and multiplied by the factor $m/V_{S_{ij}}$, where m is the mass of a single particle and $V_{S_{ij}}$ is the volume of the spatial element S_{ij}. The level of noise in this measurements can be reduced by increasing the step of the spatial subdivision dx and/or the number of time steps in which the profiles are being measured n_t. However, at the same time the larger spatial and temporal steps decrease the sensibility of the measurement for detecting flow changes in space and time correspondingly. Therefore, for non-steady flows, such as the flow during a clot development studied in this thesis, there is usually a fine balance between noise reduction and measurement sensitivity (Chapter 4). Additionally, a filtering

or smoothing methods can be used to reduce the noise. Due to the suitability of the DPD method for modelling hydrodynamics, with properly defined boundary conditions the density and velocity profiles will converge to the corresponding analytical solution of Navier-Stokes equations as n_t increases. An example of the smooth density and velocity profiles obtained by DPD method for the case of Poiseuille flow is shown in the Figure 2.1.

2.2.2 Physical parameters in 2D

In a 2D DPD simulation some physical values, like the particle volume and mass, have to be reinterpreted. Let us consider the simulation of a homogeneous fluid (like water or blood plasma), where all DPD particles in the system can be considered to have the same properties (mass, volume, inter-particle DPD forces). Then the 2D problem can be interpreted as a layer of DPD particles whose movement is restricted to a single plane. This enables the 3D interpretation of all parameters and the calculation of corresponding physical properties. As a result, in the 2D method physical parameters can be directly defined and used. Thus, in a 2D DPD simulation, next to the DPD parameters, the following physical parameters are necessary and sufficient to determine flow properties in the vessel: vessel diameter D and length L, density ρ, viscosity μ, mean flow velocity $\bar{u}_x$ and only one discretization parameter N_y, representing the number of particles in the y cross-section in their initial positions (on the regular grid with a uniform step). From the values of these parameters the values of the remaining parameters can be deduced - the mass and the volume of a single particle, as well as the body force necessary to induce the flow. Because of the uniform step of the grid for the initial positions of particles we can write:

$$\frac{L}{N_x} = \frac{D}{N_y} = \frac{H}{N_z}, \tag{2.17}$$

where H is the thickness (3rd dimension) of the volume defined by the layer of particles in the simulated plane, while N_x and N_z are defined analogously to N_y. Note that N_z is equal to 1, as the particles are contained in a plane. Then the values of N_x and H can be directly obtained from the equation (2.17). The volume V of the particle layer can be on the one hand expressed as the product of its dimensions, and on the other as the sum of volumes of all particles. Thus we have:

$$LDH = V = N_x N_y N_z V_p, \tag{2.18}$$

where V_p is the volume of a single particle. It follows that the particle volume is equal to H^3. Finally, the mass of a single particle is given by $m = \rho V_p$. The value of volume force f_x can be obtained from the equation (2.15), and the corresponding acceleration G is given by dividing the volume force by density, $G = f_x/\rho$.

2.2.3 Calculating viscosity

Although the values of the physical parameters of a simulated fluid can be set a priori, the values of DPD parameters have to be determined experimentally in order to obtain the wanted value of viscosity. The calibration of DPD parameters, σ, γ, a_{ij}, r_c and k, can be done by simulating a Poiseuille flow and comparing it to the corresponding solution of Navier-Stokes equations [11]. By integrating the equation (2.15) and dividing it by the vessel diameter, one obtains the expression for the average flow velocity in the 2D case as a function of the dynamic viscosity, the channel diameter and the external force (or pressure):

$$\bar{u}_x = \frac{\left(f_x - \frac{\partial p}{\partial x}\right) D^2}{12\mu}. \tag{2.19}$$

where $\bar{u}_x$ is the average flow velocity in the direction tangential to the vessel axis. By analogy the average flow velocity in the 3D case is given by:

$$\bar{u}_x = \frac{\left(f_x - \frac{\partial p}{\partial x}\right) R^2}{8\mu}, \tag{2.20}$$

Therefore, for the given DPD parameters, physical parameters and the volume force, the average flow velocity can be measured in a simulation and the viscosity of the simulated fluid can be calculated. The influence of the DPD parameters on the viscosity of the simulated fluid is shown in the Figure 2.4. The cut-off radius has a great impact on the viscosity of the fluid, however, it has an even greater impact on the computational cost. Hence, it is better to keep it as low as possible, and, if necessary, to increase the viscosity via other DPD parameters. Among the strength coefficients of the three DPD forces, σ, γ and a_{ij}, the dissipative force coefficient σ has the largest influence on the viscosity of the simulated fluid. The conservative force coefficient a_{ij} regulates the compressibility of the simulated fluid. While it also has a mild influence on the viscosity, by increasing it too much the velocity profile ceases to be parabolic (Figure 2.3). This effect can be counteracted by the simultaneous increase of the value of the random force coefficient γ, as it brings more energy to the system and enables particles to move more easily. Increasing values of any of the three force coefficients can result in a decrease of the upper limit of the time step, thus increasing the computational cost. Another way to regulate viscosity is to vary the value of the exponent k from the equation (2.6). However, it also brings an additional computational cost of calculating the power of k. Values of parameters used for the initial simulation in the results shown in Figure 2.4 are given in the Table 2.1. The values of initial parameters correspond to the following physical values: density of 1000 kg/m^3, vessel diameter of 0.1 mm, viscosity of 1.354 mPa·s, and mean flow velocity of 11 mm/s. In Figure 2.4 the empty dot on the graphs denotes the viscosity value obtained in the initial simulation. Data related to each of the graphs in the figure is given in Table 2.2.

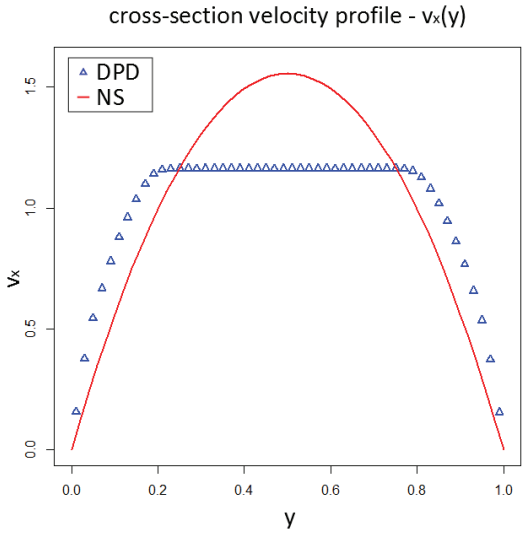

Figure 2.3: Non-parabolic velocity profile (blue) measured in simulation of Poiseuille flow with too large coefficient a_{ij} of DPD conservative force. The red curve denotes the corresponding parabolic profile obtained as a solution of Navier-Stokes equations. The horizontal axis represents the y-coordinate of the system, i.e. the cross-section of the vessel normalized by the vessel diameter. The vertical axis represents non-dimensional values of velocity in the direction tangential to the flow axis, v_x.

In DPD, the ratio of the applied body force and the measured mean velocity in Poiseuille flow is not constant for different magnitudes of body force. Thus the viscosity of the simulated fluid will change depending on the amount of the applied body force. In Figure 2.5 two graphs show the dependence of the viscosity on the body force in DPD on a larger and a smaller scale respectively. On a larger scale DPD shows a non-linear dependence and the tendency for a high increase in the viscosity as the body force becomes lower, while for a high body force the viscosity is near constant. On a smaller scale the change can be considered almost linear. Additionally, on a smaller scale a series of ten subsequent velocity measurements were taken for each value of body force. The results show the increase of oscillations as the amount of the body force decreases and as it becomes a less dominant force over the local DPD forces. For the values of parameters used in scope of this work, especially for purposes of studying blood coagulation in flows of different velocities (Section 4.2.7), changes of viscosity due to different flow velocities were under 2%.

$[L]$	$[M]$	$[T]$	D	L	n	m	r_c	σ	γ	a_{ij}	k	G
10^{-6} m	10^{-11} g	10^{-2} s	100	100	0.36	0.462963	5	3550	20000	$6{\cdot}10^5$	1	1800

Table 2.1: Initial values of parameters used in simulations for viscosity dependence of DPD parameters. $[L]$, $[M]$, $[T]$ denote the length, mass and time scales, respectively. n is the number density of particles, m is the mass of a single particle, and G is the acceleration constant of the volume force f_x in the direction along the vessel axis.

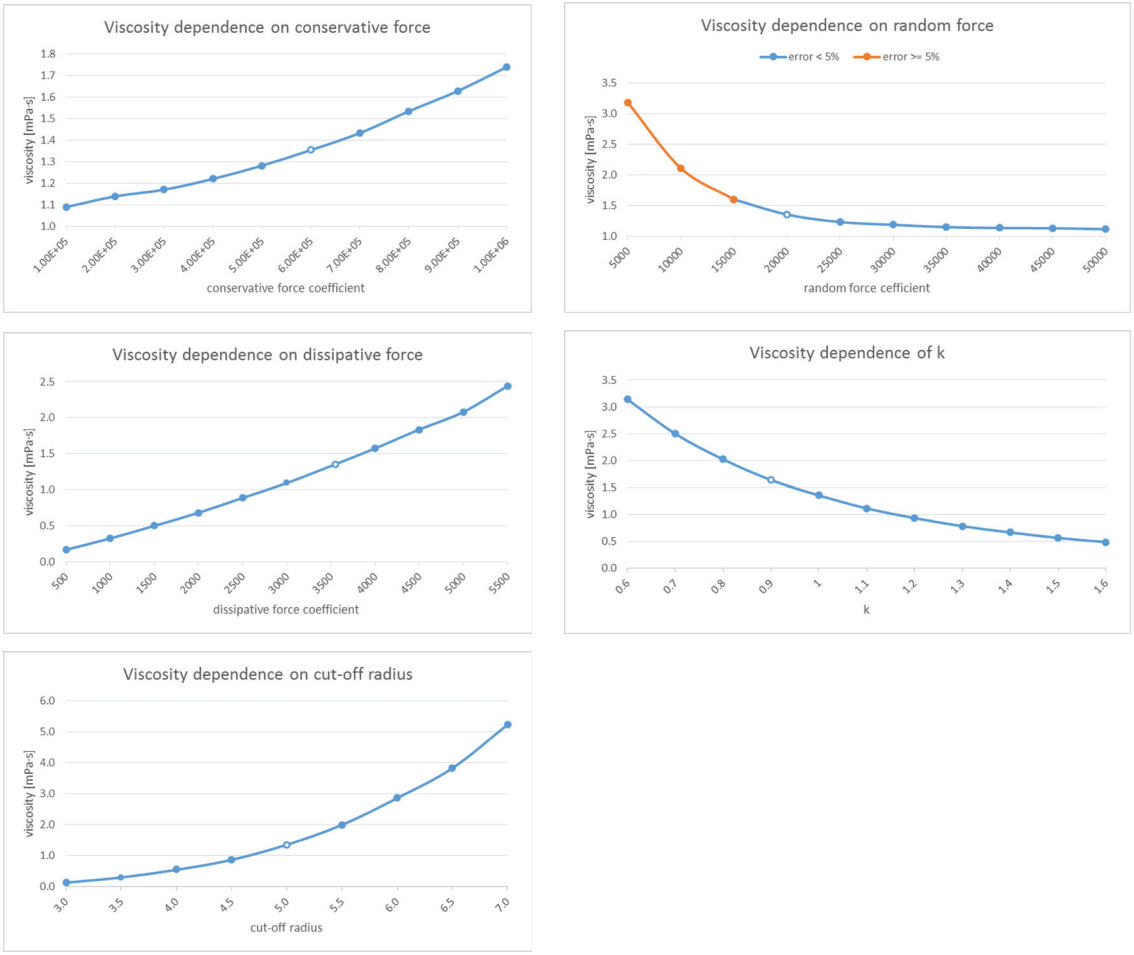

Figure 2.4: Detailed results of simulations related to viscosity dependence on DPD parameters. "err" denotes the difference between the value 1.5 and the ratio of the maximal and the mean measured flow velocity.

a_{ij}	μ [mPa·s]	err (%)	γ	μ [mPa·s]	err (%)	σ	μ [mPa·s]	err (%)	k	μ [mPa·s]	err (%)
1.00E+05	1.089	0.25	5000	3.186	24.13	500	0.169	0.49	0.6	3.137	1.38
2.00E+05	1.139	0.61	10000	2.111	15.41	1000	0.325	0.39	0.7	2.497	1.51
3.00E+05	1.170	0.11	15000	1.600	5.39	1500	0.500	0.45	0.8	2.020	1.81
4.00E+05	1.220	0.43	20000	1.354	0.99	2000	0.681	0.85	0.9	1.637	1.31
5.00E+05	1.282	0.82	25000	1.232	0.50	2500	0.887	1.00	1.0	1.354	0.99
6.00E+05	1.354	0.99	30000	1.187	0.74	3000	1.094	0.86	1.1	1.114	1.24
7.00E+05	1.433	2.56	35000	1.148	0.26	3550	1.354	0.99	1.2	0.932	1.87
8.00E+05	1.535	3.06	40000	1.135	1.05	4000	1.574	1.82	1.3	0.781	1.63
9.00E+05	1.629	3.75	45000	1.131	0.02	4500	1.836	2.43	1.4	0.665	1.49
1.00E+06	1.740	3.87	50000	1.115	0.12	5000	2.080	3.57	1.5	0.562	1.77
						5500	2.441	4.24	1.6	0.484	1.68

r_c	μ [mPa·s]	err (%)	G	μ [mPa·s]	err (%)	G	μ [mPa·s]	err (%)
3.0	0.132	2.95	57	1.510	14.59	300	1.427	0.31
3.5	0.300	2.37	180	1.435	1.23	600	1.410	1.26
4.0	0.545	2.10	569	1.397	1.69	900	1.399	1.25
4.5	0.868	1.43	1800	1.354	0.99	1200	1.373	1.27
5.0	1.354	0.99	5692	1.232	1.90	1500	1.362	1.48
5.5	1.994	1.67	18000	1.150	1.21	1800	1.345	1.35
6.0	2.859	1.58	56921	1.103	0.81	2100	1.330	1.62
6.5	3.823	1.07	180000	1.074	0.62	2400	1.318	1.66
7.0	5.227	2.21	569210	1.074	0.09	2700	1.295	1.76

Table 2.2: Data corresponding to results shown in Figure 2.4 and Figure 2.5. The spatial step Δx and the number of time steps Δt used in data measuring was 2 and $2{\cdot}10^5$ respectively. For the last data set related to the viscosity dependence on the volume force acceleration (Figure 2.5), where volume force is varied from 300 to 2700, the number of time steps Δt was increased to $1{\cdot}10^6$, to obtain more precise values of viscosity.

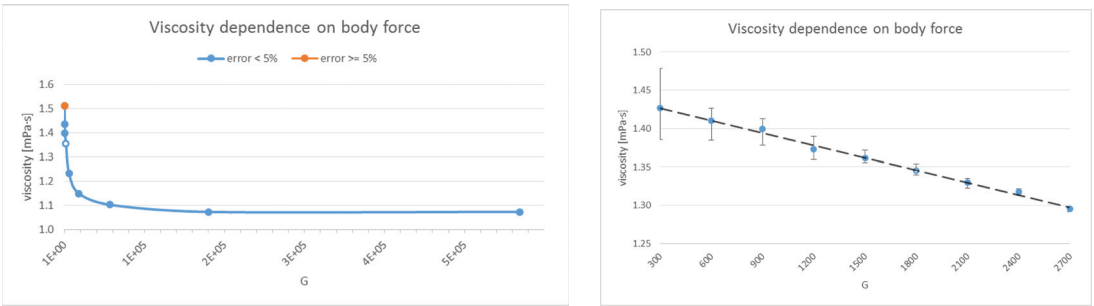

Figure 2.5: Detailed results of simulations related to viscosity dependence on external force f_x. "err" denotes the difference between the value 1.5 and the ratio of the maximal and the mean measured flow velocity.

2.2.4 Calculating wall shear rate

The experimental data related to blood flows, blood coagulation and atherosclerosis are often expressed in terms of the wall shear rate. For the simulated Poiseuille flow the value of the wall shear rate can be obtained by derivation of equation (2.15), obtaining:

$$u'_x(y) = \frac{f_x - \frac{\partial p}{\partial x}}{2\mu}(D - 2y), \tag{2.21}$$

followed by the elimination of the terms of pressure, volume force and viscosity by use of equation (2.19). Therefore

$$u'(y) = \frac{6\bar{u}}{D^2}(D - 2y). \tag{2.22}$$

Then the wall shear rate in the 2D case can be expressed in terms of just the average flow velocity and the tube diameter as:

$$u'(0) = \frac{6\bar{u}}{D}. \tag{2.23}$$

By analogy, in the 3D case from equation (2.23) we obtain:

$$u'(-R) = \frac{4\bar{u}}{R}. \tag{2.24}$$

2.3 Boundary conditions

Based on the forces acting between particles the DPD method correctly simulates hydrodynamic behaviour. However, it is not straightforward how to implement solid boundary conditions in order to obtain the correct characteristics of the system near its boundaries. In this study, for purposes of studying flow in blood vessel, the focus was on two types of boundary conditions - periodic and no-slip. The first one was used to simulate an infinite flow in a short section of a blood vessel, while the second one was used to simulate the friction blood plasma and vessel wall. The problems that appear near the no-slip solid boundaries can be separated into two types - errors in density and errors in velocity. Errors in density usually come from an imbalance of DPD forces in the boundary layer, which is present due to the lack of DPD particles on the outer side of the boundary, while the errors in velocity usually occur because of a combination of the previous reason and the implementation of the no-slip condition between particles and the boundary. In this section several methods for simulating boundary conditions in DPD are described and discussed. Even though the described methods are discussed in the context of DPD, they can be also applied directly or with some modifications to other particle methods. The methods are tested for a 2D Poiseuille flow.

In order to simulate the flow at the outflow boundary, particles which exit the simulation domain need to be deleted and accordingly, to preserve density, new particles need to be

created on the inflow boundary. This can be avoided by use of periodic boundary conditions, where the opposite boundaries (inflow and outflow) are joined to create a spatial loop - a particle which crosses the outflow boundary, instead of being removed from the system, re-enters the simulation domain at the inflow boundary. To preserve the balance of DPD forces near the boundaries, the particles near the outflow boundary exert DPD forces on the particles near the inflow boundary, and vice versa. Periodic boundary conditions are useful for studying flows where the inflow and outflow boundaries are of the same size and shape, and where the inflow and outflow velocity profiles are expected to be identical.

No-slip boundary describes the condition present in viscous fluid flows where at a solid boundary the fluid will have the zero velocity relative to the boundary. As it is the case in many particle methods, in DPD it is a priori unclear how to define a correct no-slip condition. For DPD a lot of different methods were suggested in order to achieve the correct results at low computational cost. Only some of them are listed here [44, 45, 73, 97]. In the following part of this section, methods that were investigated, developed and used in scope of this work are described and discussed.

2.3.1 Hard boundary conditions

Solid boundary implies that there is no transfer of mass (fluid medium) across the boundary. As the DPD method is discrete in time, it is possible that in a single time step some particles move across the boundary. Hence, the movement of particles which come in contact with the boundary has to be corrected. This is done by calculating the trajectory of a particle and the moment in which the particle comes in contact with the boundary. Then the particle's trajectory can be adjusted to correspond to an elastic collision. If at some step of the DPD algorithm a particle with a position p and a velocity v would cross the boundary in a single time step dt and have the incorrect position $p + vdt$, then the time of collision is given by $t_c = h/v_o$, where h is the particle's distance from the boundary and v_o is the component of velocity v orthogonal to the boundary. Once the time of contact is obtained the correct position of the particle after the elastic collision is obtained, by $p' = p + vt_c + (v - 2v_o)(dt - t_c)$, where the second and third right-hand terms describe the particle's path before and after the collision respectively. The expression can be also written in the following form $p' = p + vdt - 2v_o(dt - t_c)$ where the $p + vdt$ is already known and calculated as the incorrect position of the particle.

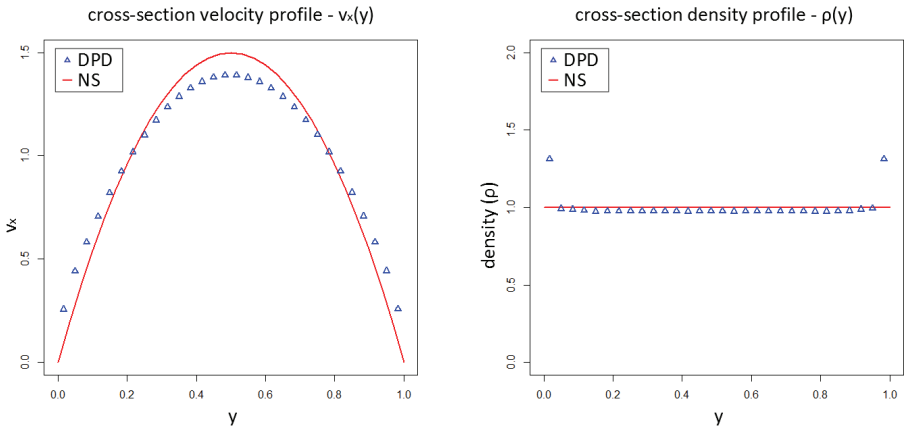

Figure 2.6: Hard boundary condition: cross-section velocity (left) and density (right) profiles obtained in Poiseuille flow by DPD method with use of hard boundary condition to simulate no-slip solid boundary. Blue markers represent data measured in the simulation, while red curves represent the corresponding solution of Navier-Stokes equations. Values on axes are non-dimensional.

In attempt to model the no-slip condition, instead of the elastic collision, an inelastic collision can be simulated where the colliding particle, at the time of contact, looses a part of its velocity which is tangential to the boundary. Its new velocity in that direction is set to the velocity of the boundary. This method is useful in Molecular Dynamics (MD) which is a micro-scale method where the movement of the particles is based on the potential forces acting between them in a case of physical contact (collision). In DPD, which is a meso-scale method, cut-off radius r_c is usually larger than the physical radius of the mass that a single particle represents, meaning that at each moment of time each particle is in contact with multiple, if not many, other particles. As there are no particles on the outer side of the boundary, there will exist an imbalance of the forces in the boundary layer, i.e. the layer of particles in the r_c proximity to the boundary. This imbalance will cause a significant deformation of the system's density profile, as it is shown in Figure 2.6. Because of the increased density of particles in the boundary layer the velocity profile cannot be correct either, resulting in a too steep increase of velocity in the boundary layer. This effect can be somewhat decreased by increasing the value of the random force coefficient σ.

2.3.2 Semi-periodic boundary conditions

Semi-periodic boundary conditions are the combination of the periodic and the hard boundary conditions. The method is suitable for flows between two parallel plates that are either stationary or move in the same direction with the same velocity. A modified periodic boundary condition acts between two opposing boundaries in a way that two particles in the

opposing boundary layers exert on each other only the component of DPD forces which is orthogonal to the boundary, while the tangential component is omitted. Additionally, the crossing of particles over the boundaries is prevented by use of hard boundary conditions. The method produces a correct density profile due to restored balance of DPD forces in boundary layers. However, the corresponding velocity profile again suffers from a too steep increase in the velocity in the boundary layers. This happens because particles do not collide with the boundary often enough to produce the effect of the no-slip condition. The effects of half periodic boundary condition shows the necessity of using boundary conditions which define the areal influence on the particles, rather than just defining the behaviour for the case of collision of particles with the boundary.

2.3.3 Estimated boundary conditions

As the problem of obtaining the correct density and velocity profiles is a result of not having particles on the outer side of the boundary, one way to try to resolve this problem is to estimate the effect such particles would have on a single particle in the boundary layer. The influence of the outer particles on a particle p inside of the domain will depend on the distance of the particle p from the boundary. In other words, the closer the particle p is to the boundary, the larger the part of the sphere around it, defined by the force cut-off radius r_c, will be outside of the domain. Let us consider a 2D case and a lower half of the circle defined by r_c around some particle p. For some step dx let us fill this lower half circle with particles p_{ij} positioned on the rectangular mesh with step dx in the following way - if $\mathbf{r}_p$ is the position of the particle p, then the position of particle p_{ij} is given with $\mathbf{r}_{ij} = \mathbf{r}_p + (i, -j)\, dx$, where $n = r_c/dx$, $-n \leq i \leq n$ and $0 \leq j \leq n$. By this definition it follows that $p \equiv p_{00}$, thus the particle p_{00} is not considered as a part of the mesh. The conservative and dissipative forces that a particle p_{ij} exerts on the particle p are then given by:

$$\begin{aligned}
\mathbf{F}^C(i,j) =& a\left(1 - \frac{r}{r_c}\right)\hat{\mathbf{r}} \\
=& \left(a\left(1 - \frac{r}{r_c}\right)\hat{r}_x, a\left(1 - \frac{r}{r_c}\right)\hat{r}_y\right) \qquad (2.25) \\
\mathbf{F}^D(i,j) =& -\gamma\omega^D(r)\left(\mathbf{v}\cdot\hat{\mathbf{r}}\right)\hat{\mathbf{r}} \\
=& \left(-\gamma\omega^D(r)\left(v_x\hat{r}_x + v_y\hat{r}_y\right)\hat{r}_x, -\gamma\omega^D(r)\left(v_x\hat{r}_x + v_y\hat{r}_y\right)\hat{r}_y\right) \\
=& \left(-\gamma\omega^D(r)\left(v_x\hat{r}_x^2 + v_y\hat{r}_x\hat{r}_y\right), -\gamma\omega^D(r)\left(v_x\hat{r}_x\hat{r}_y + v_y\hat{r}_y^2\right)\right), \qquad (2.26)
\end{aligned}$$

where $\mathbf{r} = \mathbf{r}_p - \mathbf{r}_{ij}$, $r = |\mathbf{r}|$, $\hat{\mathbf{r}} = \mathbf{r}/r$, $\mathbf{v_p}$ and $\mathbf{v}_{ij}$ are velocities of the particles p and p_{ij} respectively, and $\mathbf{v} = \mathbf{v}_p - \mathbf{v}_{ij}$. As all the particles p_{ij} are particles of the boundary we can

assume that are all moving with the same velocity $\mathbf{v}$. Now let us denote the components of the vectors in equations (2.25), (2.26) as:

$$\begin{aligned} X^C(i,j) &= a\left(1-\frac{r}{r_c}\right)\hat{r}_x, \\ X_x^D(i,j) &= -\gamma\omega^D(r)\hat{r}_x^2, \\ X_y^D(i,j) &= -\gamma\omega^D(r)\hat{r}_x\hat{r}_y, \\ Y^C(i,j) &= a\left(1-\frac{h}{r_c}\right)\hat{r}_y, \\ Y_x^D(i,j) &= -\gamma\omega^D\hat{r}_x\hat{r}_y, \\ Y_y^D(i,j) &= -\gamma\omega^D\hat{r}_y^2. \end{aligned} \tag{2.27}$$

Then it follows that:

$$\begin{aligned} X^C(-i,j) &= -X^C(i,j), \\ X_y^D(-i,j) &= -X_y^D(i,j), \\ Y_x^D(-i,j) &= -Y_x^D(i,j), \\ X^C(0,j) &= X_y^D(0,j) = Y_x^D(0,j) = 0. \end{aligned} \tag{2.28}$$

Let us now write the influence of all particles of the mesh for which r_y is greater than some non-negative value h on the particle p:

$$\begin{aligned} X^C(h) &= \sum_{-n\le i\le -n}\sum_{jdx>h} X^C(i,j) \\ X_x^D(h) &= \sum_{-n\le i\le -n}\sum_{jdx>h} X_x^D(i,j), \\ X_y^D(h) &= \sum_{-n\le i\le -n}\sum_{jdx>h} X_y^D(i,j), \\ Y^C(h) &= \sum_{-n\le i\le -n}\sum_{jdx>h} Y^C(i,j), \\ Y_x^D(h) &= \sum_{-n\le i\le -n}\sum_{jdx>h} Y_x^D(i,j), \\ Y_y^D(h) &= \sum_{-n\le i\le -n}\sum_{jdx>h} Y_y^D(i,j). \end{aligned} \tag{2.29}$$

From the identities (2.28) it follows that $X^C(h)$, $X_y^D(h)$ and $Y_x^D(h)$ are equal to zero for each h. This means that we can write a boundary force on a particle that is on h distance from the boundary as:

$$\mathbf{F}(h) = \frac{n_{sim}}{n_{calc}}\Big(v_x X_x^D(h) \quad , \quad Y^C(h) + v_y Y_y^D(h)\Big). \tag{2.30}$$

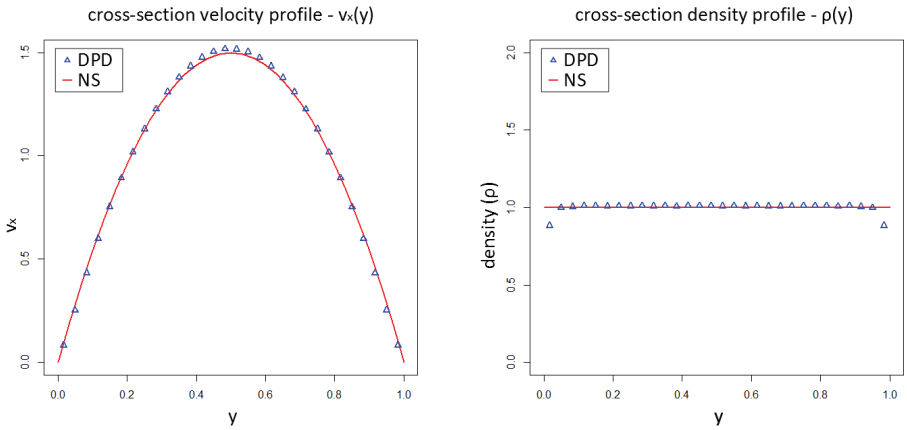

Figure 2.7: Estimated boundary conditions: cross-section velocity (left) and density (right) profiles obtained in Poiseuille flow by DPD method with use of estimated boundary conditions to simulate no-slip solid boundary. Blue markers represent data measured in the simulation, while red curves represent the corresponding solution of Navier-Stokes equations. Values on axes are non-dimensional.

In cases when the flow is tangential to the boundary, as it is in the case of Poiseuille flow, and the conservative force is large, usually the $v_y Y_y^D(h)$ can be omitted as the orthogonal part of particle velocities v_y is very small and the conservative force is much more dominant. In other words, in Poiseuille flow, the velocity profile is influenced mainly by the part of the dissipative force depending on the tangential velocity of particles, while the density profile is influenced mostly by the conservative force. Figure 2.8 shows all functions in (2.29) for $h \in [0, r_c]$. Results of the estimated boundary conditions, presented in Figure 2.7, show a more correct velocity profile, while the density profile has a small deformation in the near boundary layer.

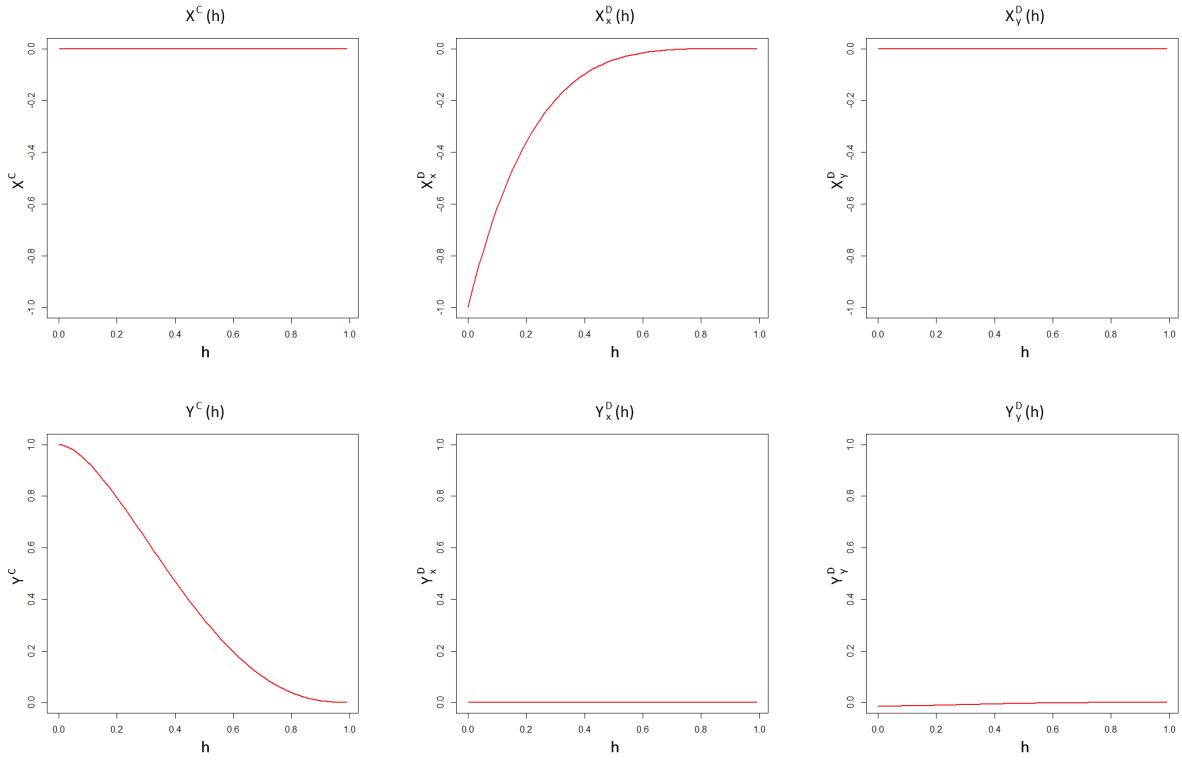

Figure 2.8: Estimated boundary conditions: dependence of forces described in equations (2.29) on the particle distance from the boundary, h. The horizontal axis represents the particle distance from the boundary normalized by the force cut-off radius r_c, while the vertical axis represents the value of force. Graphs in the top row correspond to forces X^C, X_x^D and X_y^D acting in the direction tangential to the boundary. Graphs in the bottom row correspond to forces Y^C, Y_x^D and Y_y^D acting in the direction perpendicular to the boundary.

2.3.4 Measured boundary conditions

Instead of estimating the average force on a particle and how it depends on the distance h from the boundary, this influence can be measured in the bulk flow. The orthogonal part of the force acting from the boundary on a particle at h distance from the boundary can be expressed in the following form:

$$F_y(h) = \frac{1}{N} \sum_{i=1}^{N-1} \sum_{j=i+1}^{N} |F_y(i,j)| \left[h_{ij} > h\right], \tag{2.31}$$

where N is the number of particles in the bulk flow,

$$F_y(i,j) = \left(\mathbf{F}_{ij}^C + \mathbf{F}_{ij}^D + \mathbf{F}_{ij}^R\right) \cdot \hat{\mathbf{y}} \tag{2.32}$$

is the sum of DPD forces for the pair of particles i and j, $h_{i,j} = |\mathbf{r}_{ij} \cdot \hat{\mathbf{y}}|$, $\mathbf{r}_{ij} = \mathbf{r}_i - \mathbf{r}_j$, $\mathbf{r}_i$ and $\mathbf{r}_j$ are vectors of positions of particles i and j respectively, $\hat{\mathbf{y}}$ is the unit vector in y direction, $\left[h_{ij} > h\right]$ is equal to 1 if the condition $(h_{ij} > h)$ is true and 0 if it is false, for $0 \leq h < r_c$. The expression (2.31) is given in a simple form to be easier to understand, but is not optimized for computation. Not all pairs of particles are in r_c proximity, hence forces between the most of the pairs are zero. The measurement can be taken at the same time when the forces between particles are calculated in a step of DPD algorithm. In this way the measurement can be done at a very low cost, and, for some given step dx, values of $F_y(h)$ can be calculated for $h = k \cdot dx$, $k = 0, \ldots, r_c/dx$, and memorized in a lookup table. For more precise results, an average of $F_y(h)$ can be measured through several time steps of DPD algorithm.

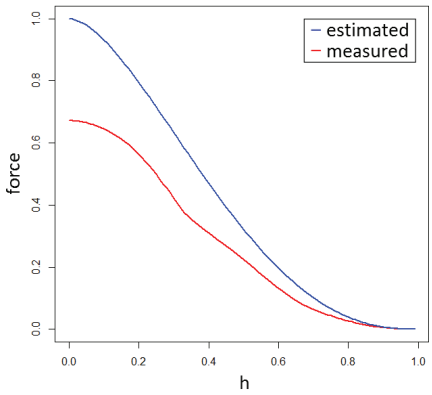

Figure 2.9: Comparison between the orthogonal components of force in estimated and measured boundary conditions.

An example of comparison of the measured and estimated forces on a particle can be seen in Figure 2.9. The difference between the force profiles can be explained by a rather high value of the conservative force coefficient used in the simulation, with the result that the particles were never closer then $0.33r_c$. For a lower value of the conservative force coefficient, the measured and calculated functions become similar. Figure 2.10 shows velocity and density profile obtained by a combined boundary condition - the estimated force function was used for the boundary influence in the direction tangential to the boundary, while the measured force function was used in the orthogonal direction. While the velocity profile remained similar to the one in Figure 2.7, the density profile was correct due to the use of the measured force function.

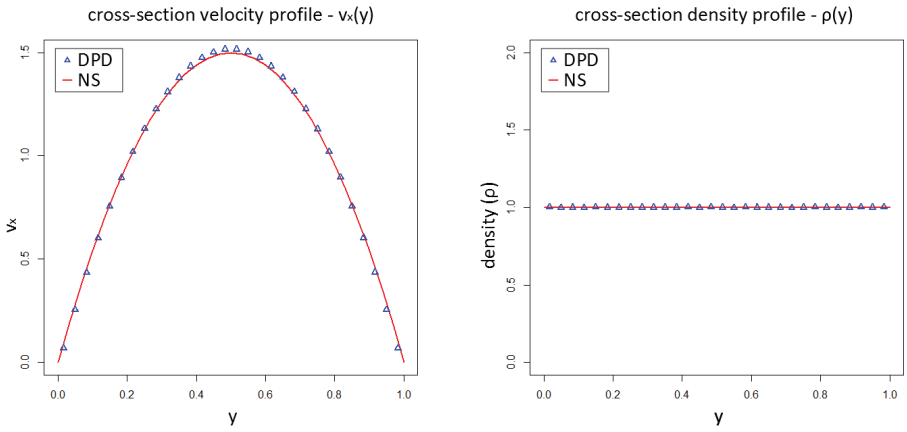

Figure 2.10: Measured boundary condition: cross-section velocity (left) and density (right) profiles obtained in Poiseuille flow by DPD method with use of a combination of measured and estimated boundary conditions to simulate no-slip solid boundary. Measured boundary condition was used for the part of force orthogonal to the boundary, while estimated boundary condition was used for the tangential part. Blue markers represent data measured in the simulation and red curves represent the corresponding solution of Navier-Stokes equations. Values on axes are non-dimensional.

2.3.5 Mirror boundary conditions

The no-slip solid boundary is modelled in the following way: if a particle p is on a distance $r < r_c$ from the solid boundary, there exists a mirror image p' of the particle p on the other side of the boundary, with the velocity opposite to the velocity of particle p ($\mathbf{v}_{p'} \equiv -\mathbf{v}_p$). This can seem like adding a fair number of new particles, which can increase the simulation cost. Although the increase of computational cost cannot be completely avoided, the boundary conditions can be efficiently implemented without any real addition of new particles. All the mirrored particles are mirror images of particles which are in boundary layers of the solid boundaries. Therefore, when we calculate forces between two particles in the simulation domain, p_1 and p_2, if they are both in the same boundary layer, we can calculate the force of the imaginary particle p_1' on the particle p_2 and p_2' on p_1. Additionally, if particle p is on $r < \frac{1}{2}r_c$ distance from the boundary, the force from p' on p is calculated. As it is shown in Figure 2.11, the described boundary condition produces correct profiles for both, density and velocity.

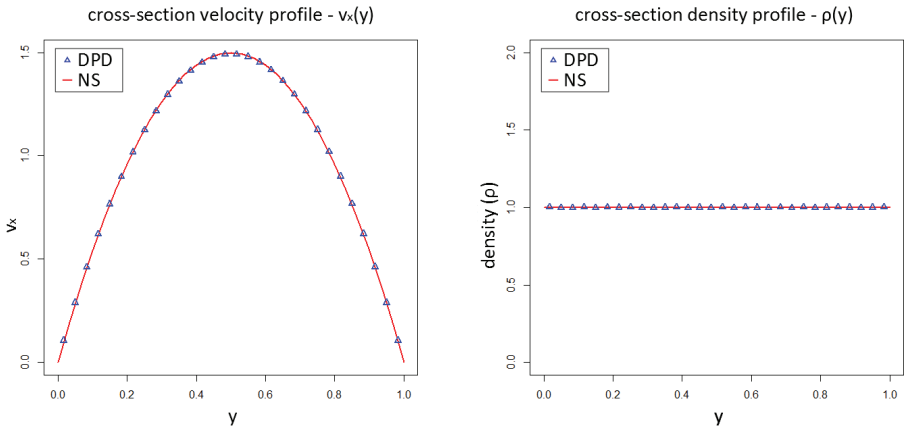

Figure 2.11: Mirror boundary condition: cross-section velocity (left) and density (right) profiles obtained in Poiseuille flow by DPD method with use of mirror boundary condition to simulate no-slip solid boundary. Blue markers represent data measured in the simulation, while red curves represent the corresponding solution of Navier-Stokes equations. Values on axes are non-dimensional.

2.3.6 Enforced boundary conditions

The velocity profile in Poiseuille flow can be also corrected by applying a correction in the boundary layer. The velocity profile is being measured during the simulation and on each particle in a boundary layer an additional force is applied in the direction tangential to the boundary. A precise expression of the additional force is given by the equation:

$$F_x = m\frac{(v' - v)}{dt}, \tag{2.33}$$

where v is the tangential part of the current velocity of the particle, v' is the velocity given by the corresponding solution of Navier-Stokes equations for an incompressible fluid in a Poiseuille flow, dt is the time step and m is the mass of the particle. The method produces correct velocity profile for Poiseuille flow, however it is not suitable for studying clot growth in flow.

2.3.7 Particle generation area

In the simulation of clot growth in flow the numbers of platelets which enter the domain at the inflow boundary and those which exit the domain at the outflow boundary are not equal as some platelets will become part of the clot and be contained in the domain. Hence, the constant inflow of platelets cannot be simulated by periodic boundary conditions, and more

complex methods have to be used. One approach is to define a particle generation area (GA) at the inflow part of the domain, as shown in Figure 2.12. The generation area (GA) works independently from the remaining part of the simulation domain - simulation area (SA). The solid boundaries in GA are modelled in the same way as in SA, but the inflow and outflow boundaries are modelled as periodic boundaries, meaning that the particle that exits GA on the outflow boundary reappears on the GA inflow boundary, creating an infinite flow loop. In addition, particles from SA do not influence the particles from GA, but the particles from GA can influence the particles from SA. For each particle which crosses the GA outflow boundary an exact copy is made at the SA inflow boundary, and this new particle is being joined to SA. Once the particle has been joined to SA, it can return for a short time in GA, but it remains assigned to SA and does not influence particles from GA. Furthermore, when it crosses back from GA to SA, it does not generate a new particle. All this insures the integrity and correctness of GA and also the non-biased creation of particles for SA.

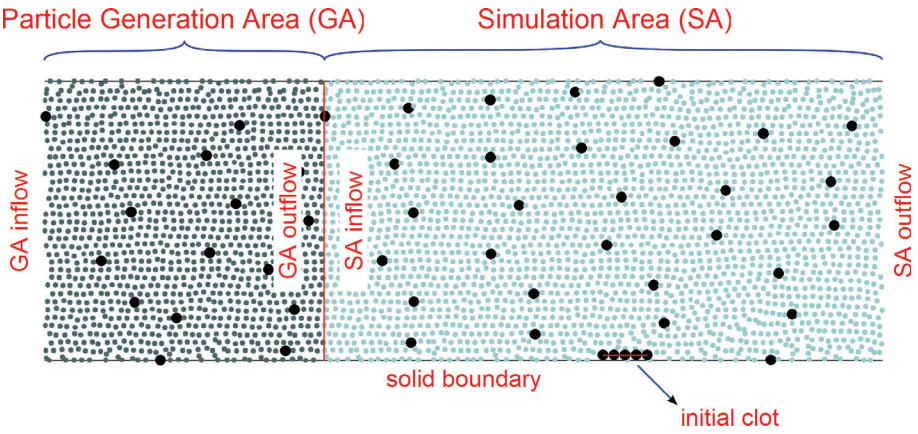

Figure 2.12: Particle Generation Area (GA) and Simulation Area (SA). Reprinted with permission from [117] – *A. Tosenberger et al., Russian Journal of Numerical Analysis and Mathematical Modelling, De Gruyter, 2012.*

On the SA outflow boundary, particles which exit the simulation domain are being deleted. In order to keep the balance of DPD forces near the outflow boundary, one way periodic boundary conditions are used. The GA inflow and SA outflow boundaries are paired, as it is normally done when using the periodic boundary conditions. However, only the particles from the inflow boundary layer can influence the particles in the outflow boundary layer, while in the opposite direction particles do not influence each other. This way, at the outflow boundary a correct velocity and density profiles are enforced, while the generation area remains a closed system. Figure 2.12 shows a scheme of the simulation and generation areas. The method is similar to a method used in [99].

In models of blood coagulation, described in chapters 3 and 4, the particle generation area was used in order to have a constant inflow of platelets, undisturbed by the ongoing clot growth and the related changes in flow. Vessel walls were modelled as solid no-slip

boundaries with use of mirror boundary conditions (Section 2.3.5), as they produce more correct results than other boundary conditions discussed in Section 2.3.

2.4 Erythrocyte model

In previous sections the DPD method was discussed in the aspect of homogeneous fluid simulation. Once we have good results for simulating blood plasma as a Newtonian fluid with particle dynamics, the next step in blood flow modelling is to introduce blood cells which are significant for the properties of blood. Erythrocytes are the most interesting blood cells for modelling from the point of view of membrane deformability and behaviour under different external conditions (in flow). An erythrocyte membrane includes a lipid bilayer and spectrin network connected by transmembrane proteins [86]. Such membrane exhibits incompressible properties, resistance to areal changes and planar shear deformation. In the resting state the erythrocyte membrane takes a biconcave shape (Section 1.1.2, Figure 1.3). This shape is the result of the minimization of surface energy. In 2D, we can take a membrane with constant perimeter $2r\pi$, encapsulating an area of $\frac{3}{5}r^2\pi$, and as a solution of the problem of minimization of surface energy we will obtain the biconcave shape. To model this behaviour with a method suitable for DPD, we take a n-sided regular polygon with particles on its vertices, and define three equations which govern the forces acting between vertices of the polygon. All three equations are based on the Hook's law (Figure 2.13). The first one defines forces between each two neighbouring vertices and describes the membrane elongation:

$$F_i^L = k_L \left(1 - \frac{l_i}{l_0}\right), \tag{2.34}$$

where k_L is the force strength coefficient, l_0 is the equilibrium distance between two neighbouring vertices, and l_i is the distance between vertices i and $i+1$. The second equation describes the forces originating from a local bending of the membrane:

$$F_i^B = k_B \left(1 - \frac{\alpha_i}{\alpha_0}\right), \tag{2.35}$$

where k_B is the force strength coefficient, α_0 is the equilibrium angle between two neighbouring sides of the polygon, and α_i is the angle between vertices $i-1$, i and $i+1$. To describe the tendency of the membrane to be locally smooth the equilibrium angle α_0 is set to π. The third equation describes the pressure and it is responsible for the preservation of the area enclosed by the membrane:

$$F_i^P = k_P \left(1 - \frac{A}{A_0}\right), \tag{2.36}$$

where k_P is the force strength coefficient, A_0 is the equilibrium and A the current area of the polygon. As a result, on a particle i, representing one polygon vertex, the following forces are exerted:

$$\mathbf{F}_i^L = \frac{1}{2}\left(F_{i-1}^L \hat{\mathbf{r}}_{i-1,i} - F_i^L \hat{\mathbf{r}}_{i,i+1}\right), \tag{2.37}$$

$$\mathbf{F}_i^B = \frac{F_{i-1}^B - F_i^B}{l_{i-1}} \hat{\mathbf{n}}_{i-1,i} + \frac{F_{i+1}^B - F_i^B}{l_i} \hat{\mathbf{n}}_{i,i+1}, \tag{2.38}$$

$$\mathbf{F}_i^P = F_{i-1}^P \hat{\mathbf{n}}_{i-1,i} + F_i^P \hat{\mathbf{n}}_{i,i+1}, \tag{2.39}$$

where $\mathbf{r}_{i-1,i} = \mathbf{r}_i - \mathbf{r}_{i-1}$, $r_{i-1,i} = |\mathbf{r}_{i-1,i}|$, $\hat{\mathbf{r}}_{i-1,i} = \mathbf{r}_{i-1,i}/r_{i-1,i}$, and $\hat{\mathbf{n}}_{i-1,i}$ is the unit vector normal to $\hat{\mathbf{r}}_{i-1,i}$ in direction outside of the polygon. Then the movement of each particle is simply determined by the sum of these forces according to Newton's second law of motion. As the volume and surface of RBC membrane does not change significantly in natural conditions, in simulations we used large coefficients k_L and k_P to preserve polygon perimeter and area, while k_B was significantly lower, allowing the membrane to deform. The equilibrium area A_0 of the polygon was set to $0.6A_{init}$, where A_{init} is the area enclosed by the corresponding regular polygon. With this model we obtained the characteristic biconcave shape of the RBC membrane, as shown in Figure 2.13 (right). As the model is basically a system of springs, the energy of the system will increase in time. One way to correct the error is to introduce dampening to the springs of the system. However, the use of dampened springs is unnecessary, as this model is intended to be used in DPD, where the vertices of the membrane will be DPD particles and the membrane itself will be surrounded by DPD particles (simulating fluid). The membrane, as a system of springs, will therefore be stabilized by dissipative forces acting between DPD particles.

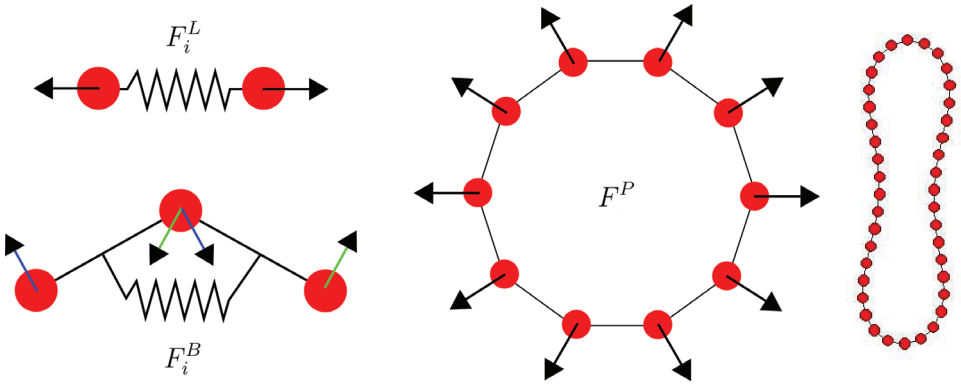

Figure 2.13: Erythrocyte model: scheme of membrane elongation and bending forces (left), pressure forces (middle), and the stable biconcave shape obtained by the model in DPD (right). Reprinted with permission from [116] – *A. Tosenberger et al.,Mathematical Modelling of Natural Phenomena, Cambridge University Press, 2011.*

2.4.1 Capillary flow

In order to test the behaviour of the erythrocyte model coupled with DPD we simulated the flow in a capillary of diameter 10μm with one erythrocyte starting in the resting biconcave shape turned orthogonally to the flow axis. It is observed that in such situations the erythrocyte undergoes a change from its natural biconcave shape to the so-called parachute shape following the parabolic velocity profile. The described behaviour obtained in DPD simulation is shown in Figure 2.14. For some time the erythrocyte remained in the parachute shape and in the position orthogonal to the flow axis. However, this was not the stable state of the erythrocyte, and the erythrocyte eventually turned in the direction of the flow and regained the biconcave shape. Similar behaviours were studied in [89, 101, 104].

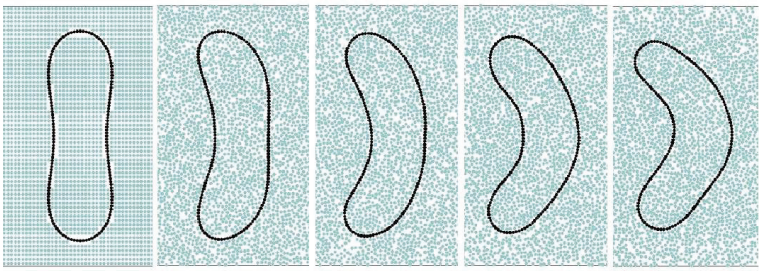

Figure 2.14: Erythrocyte model: development of the parachute shape in a narrow Poiseuille flow. Reprinted with permission from [116] – *A. Tosenberger et al.,Mathematical Modelling of Natural Phenomena, Cambridge University Press, 2011.*

2.4.2 3D model

In 3D the membrane is represented as a two-dimensional network of particles as described in [15, 16]. Similar to the 2D case, membrane particles are connected by springs (modelled by Hooke's law) to form an irregular polyhedron with triangular sides. Forces acting to the membrane particles are chosen analogically to [63]. The first force acts between any two neighbouring vertices and describes the ability of the corresponding joint to elongate:

$$\mathbf{F}_s = k_s \left(1 - \frac{l}{l_0}\right) \tau, \tag{2.40}$$

where l is the length of joint between two vertices, l_0 is the equilibrium length, and k_s is the stiffness coefficient, τ is the unit vector which is co-directional with the vector connecting two neighbouring particles.

To express areal incompressibility the force resisting to every triangular element area change is introduced:

$$\mathbf{F}_a = k_a \left(1 - \frac{s}{s_0}\right) l_c \hat{\mathbf{n}}, \tag{2.41}$$

where s is the area of the triangular element, s_0 is the equilibrium area, k_a is the area expansion modulus, l_c is the length of a side of a control area for a particle which is shown in Figure 2.15 (left), $\hat{\mathbf{n}}$ is the unit normal vector to this side. Such force appears in a particle from all triangle elements sharing this particle.

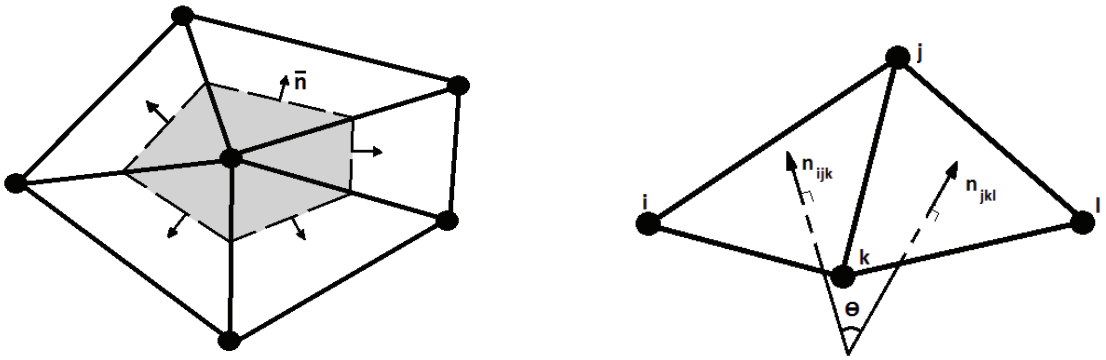

Figure 2.15: Left: the control area of a particle. Right: Two neighbouring triangular elements of the erythrocyte membrane. Reprinted with permission from [15] – *N. Bessonov et al., Russian Journal of Numerical Analysis and Mathematical Modelling, De Gruyter, 2013.*

Since an erythrocyte shows the capacity of out-of-plane bending deformation, bending springs were introduced between two neighbouring triangular elements:

$$\mathbf{F}_{b_i} = k_b \tan\left(\frac{\theta}{2}\right) \hat{\mathbf{n}}_{ijk}, \tag{2.42}$$

$$\mathbf{F}_{b_l} = k_b \tan\left(\frac{\theta}{2}\right) \hat{\mathbf{n}}_{jki}, \tag{2.43}$$

$$\mathbf{F}_{b_j} = \mathbf{F}_{b_k} = -\frac{\mathbf{F}_{b_i} + \mathbf{F}_{b_l}}{2}, \tag{2.44}$$

where θ is an angle between neighbouring triangular elements, k_b is the stiffness coefficient, $\hat{\mathbf{n}}_{ijk}$ and $\hat{\mathbf{n}}_{jkl}$ are the unit normal vectors to the corresponding triangles, see Figure 2.15 (right). A tangential function is chosen to avoid the folding of the spring at large bending deformation [120].

So far, only the membrane characteristics have been described, which alone do not ensure the erythrocyte shape. In order to obtain its shape, an additional type of force is needed to describe the volume surrounded by the shell, i.e. the volume of erythrocyte. Hence, a fourth force which acts to a triangular element is introduced:

$$\mathbf{F}_v = k_v \left(1 - \frac{v}{v_0}\right) s\hat{\mathbf{n}}, \tag{2.45}$$

where v is the polyhedron volume, v_0 is the relaxation volume, and k_v is the coefficient which is equivalent to the bulk modulus, s is the area of triangular element and $\hat{\mathbf{n}}$ is its unit normal vector.

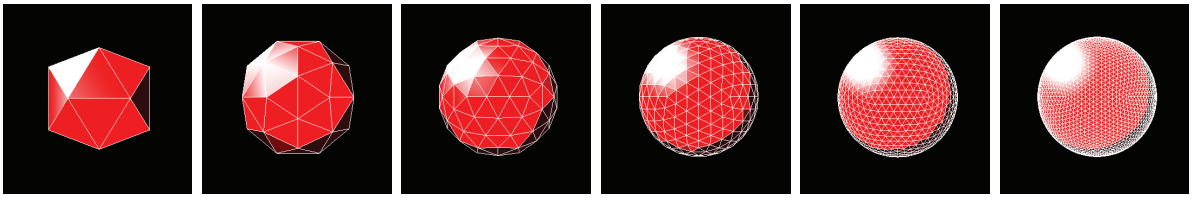

Figure 2.16: First six steps of sphere triangulation used at the initial step of erythrocyte simulation.

The erythrocyte is known to be deformable, easily changing shape under the influence of external forces. However, the area of their membrane, as well as its volume remains almost constant in a healthy erythrocyte. Therefore, values of stiffness coefficients in the model are chosen correspondingly. The values k_v and k_a are larger, making the membrane more resistant to changes in its area, while k_s is lower to allow the shape changes. The typical values of parameters used in [15, 16] are as follows: $k_s = 0.410^{-11}$ N, $k_a = 510^{-4}$ N/m, $k_v = 2$ N/m^2, $k_b = 2.410^{-11}$ N.

Figure 2.16 shows the initial step of the 3D erythrocyte method - sphere triangulation. Depending on the values of parameters it is possible to obtain both biconcave and parachute membrane shape without external forces acting on the membrane (Figure 2.17).

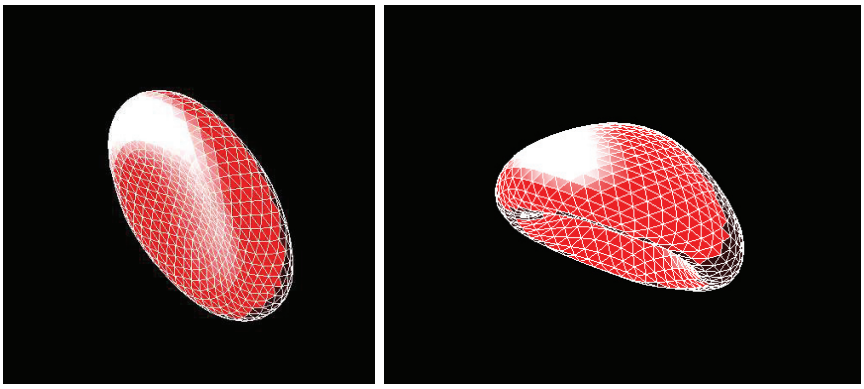

Figure 2.17: Biconcave (left) and parachute (right) erythrocyte shapes obtained by the model (2.40)-(2.45) in DPD. The two shapes are obtained with different values of parameters, without any external forces acting on the membrane.

Chapter 3

Discrete model of platelet aggregation in flow

3.1 Description

In this section a discrete model of platelet aggregation in blood plasma flow is described. It serves as the first step towards the development of a blood coagulation model. In this model we do not consider the blood coagulation pathways. DPD method is used to describe blood plasma flow inside a 2D longitudinal cross-section of a blood vessel. Platelets are also modelled as soft DPD particles, similar to the plasma particles. The radius and mass of all particles (plasma and platelets) are chosen to correspond to the physical size and the mass of platelets. In our simulation the physical radius is set to 1μm and the mass is chosen in such a way that the particle density corresponds to the density of the blood plasma ($\approx 10^3 \text{kg/m}^3$). The interactions between all particles are then governed by DPD as described in Section 2.1 with additional adhesion force acting between aggregated platelets. By virtue of clot mechanical properties [19, 54, 106, 126], the adhesion force is modelled as a pairwise force between two platelets expressed in the form of Hooke's law:

$$\mathbf{F}_{ij}^{A} = k^{A} \left(1 - \frac{r_{ij}}{d_C}\right) \hat{\mathbf{r}}_{ij}, \tag{3.1}$$

where k^A is the force strength constant and d_C is the force relaxation distance which is equal to two times the physical radius of a platelet. As binding of platelets occurs due to their surface adhesion receptors, two platelets in a flow connect when they come in physical contact, i.e. $r_{ij} \leq d_C$ (connection criterium). Platelets remain connected until their distance does not exceed some critical value d_D (disconnection criterium) which is greater then d_C. In discrete model simulations d_D was set to 1.5 times of the platelet diameter.

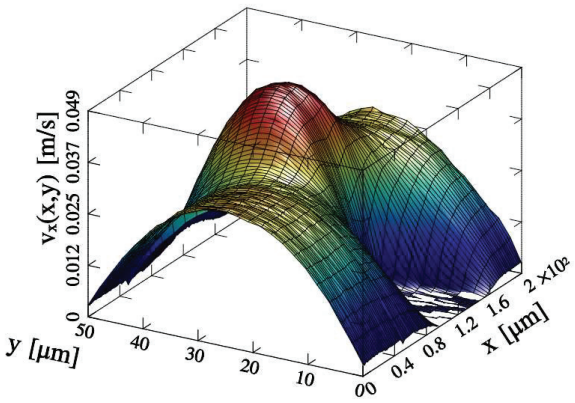

Figure 3.1: Velocity profile in a simulation of flow in a blood vessel with a large clot: velocity near the clot increases due to narrowing in the blood vessel. Reprinted with permission from [118] – *A. Tosenberger et al., Journal of Theoretical Biology, Elsevier, 2013.*

3.2 Time dependent platelet adhesion force

Platelet adhesion is a complex multi-step process which involves adhesion receptors of at least two different types and the process of platelet activation [77, 112, 113]. First, a platelet from the flow binds with platelets at the injury site through weak GPIba bonding, then it activates and forms a stable adhesion through firm integrin bonding. The latter step cannot take place without the first one due to kinetic restrictions, and the first step is reversible and cannot result in stable adhesion. Since the kinetics of receptor binding is not explicitly introduced in the model, time evolution of the adhesion force needs to be taken into account. As adhesion becomes stronger with time, a constant coefficient k^A in the equation (3.1) is substituted with a time dependent function f^A:

$$\mathbf{F}_{ij}^A = f^A(t_{ij}) \left(1 - \frac{r_{ij}}{d_C}\right) \hat{\mathbf{r}}_{ij}, \tag{3.2}$$

where f^A is a function depending on time and t_{ij} is the duration of the connection between platelets i and j. Two cases were studied: the first, in which the function f^A is linear, and the second, in which f^A is a step function.

In the linear case the function f^A is defined in the following way:

$$f^A(t_{ij}) = a_A t_{ij} + b_A, \tag{3.3}$$

where b_A is the initial adhesion force strength, and a_A is the increase rate of the adhesion force. In the step function case, f^A is defined as follows:

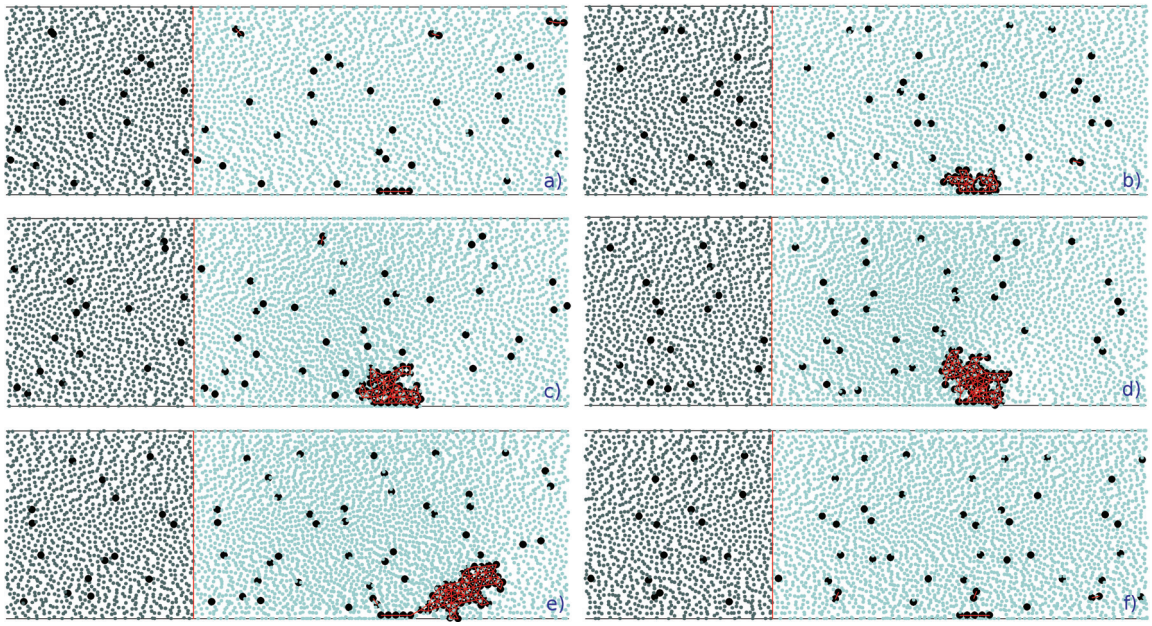

Figure 3.2: Snapshots of clot growth in a simulation with a constant platelet adhesion force coefficient. When the clot becomes sufficiently large, the force exerted by blood plasma breaks the clot and it is taken downstream by the flow. Reprinted with permission from [117] – *A. Tosenberger et al., Russian J. Numer. Anal. Math. Modelling, De Gruyter, 2012.*

$$f^A(t_{ij}) = \begin{cases} f_w^A, & \text{if } t_{ij} < t_c, \\ f_s^A, & \text{if } t_{ij} \geq t_c, \end{cases} \tag{3.4}$$

where f_w^A is the strength coefficient of the weaker connection, f_s^A is the strength coefficient of the stronger connection and t_c is the time needed for the weak connection to transform into the stronger one. In the model t_c can be considered as the mean activation time upon the initial binding of platelets.

3.3 Results

The values of parameters are chosen in such a way that they correspond to the vessel of $50\mu m$ in diameter and $150\mu m$ long (of which, the first $50\mu m$ is Particle Generation Area, followed by $100\mu m$ of Simulation Area, as shown in Figure 2.12). The density and the viscosity of the simulated medium are chosen to correspond to the density and viscosity of blood plasma [128]. The average velocity of the flow is chosen to be $24mm/s$. To initiate clotting, at the beginning of the simulation, several stationary platelets are positioned next to the lower vessel wall in the Simulation Area.

In order to verify the DPD parameters and the method's applicability for non-symmetric flows, density and velocity analysis were done in all simulations. This analysis was done by averaging the data through a short period of time as described in Section 2.2.1. As it is shown in Figure 2.1 (Section 2.2.1), in the simulation without a clot the density profile was uniform and the velocity profile was parabolic. With the clot growth, the velocity profile would change with the increase of velocity in the clot region due to the narrowing of the vessel (Figure 3.1).

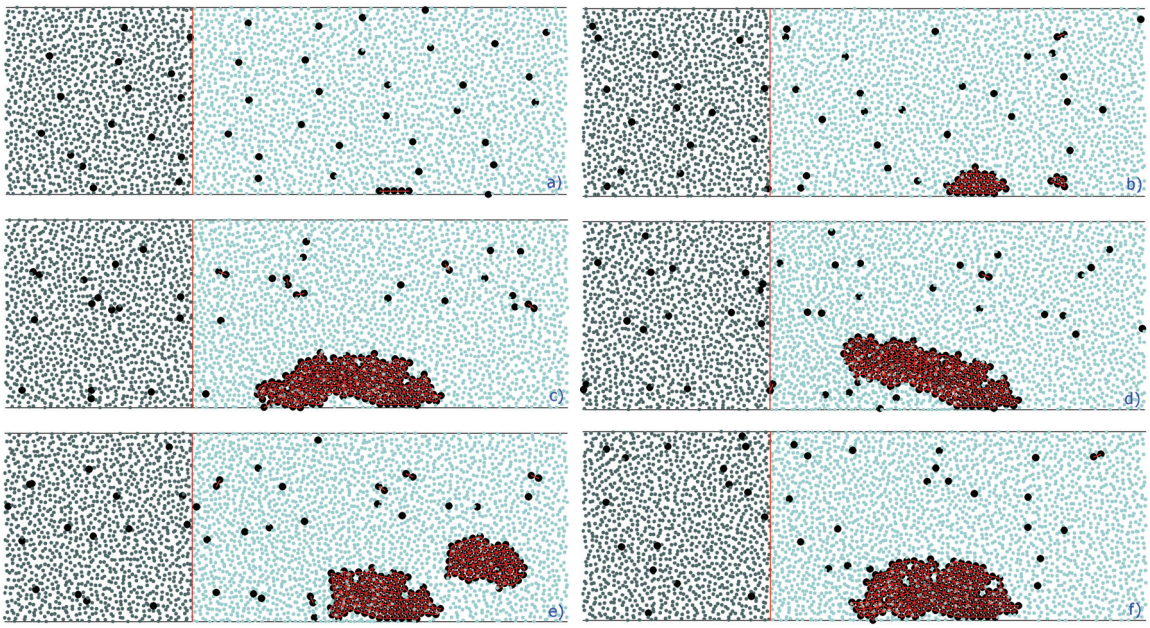

Figure 3.3: Snapshots of clot growth for a linear time dependent adhesion force (older connections are depicted with darker red colour): a) initial clot, b) small group of platelets connected with still weak adhesion forces, c), d) and e) clot rupture, f) continuation of clot growth. Reprinted with permission from [117] – *A. Tosenberger et al., Russian Journal of Numerical Analysis and Mathematical Modelling, De Gruyter, 2012.*

3.3.1 Constant coefficient of adhesion force strength

The discrete model was used to study platelet aggregation in flow and its dependence on the platelet adhesion force. Due to clot growth and increased flow pressure on the clot, a clot rupture can occur.

In the case of a constant coefficient of adhesion force (equation (3.1)), three basic types of clot growth were observed. For too small values of k^A platelets would not attach to the initial clot, while for too big values the clot would constantly grow without breaking. The most interesting behaviour was observed with medium values - the clot would grow to a

certain size, and when the stress on the clot from the flow would overcome the strength of adhesion forces, established between the aggregated platelets, the clot would break and would be taken by the flow. The snapshots of this process and its stages are shown in Figure 3.2, while the clot growth in this case can be seen in Figure 3.5. In simulations with a constant adhesion force clot breaking mostly occurred near the initial clot.

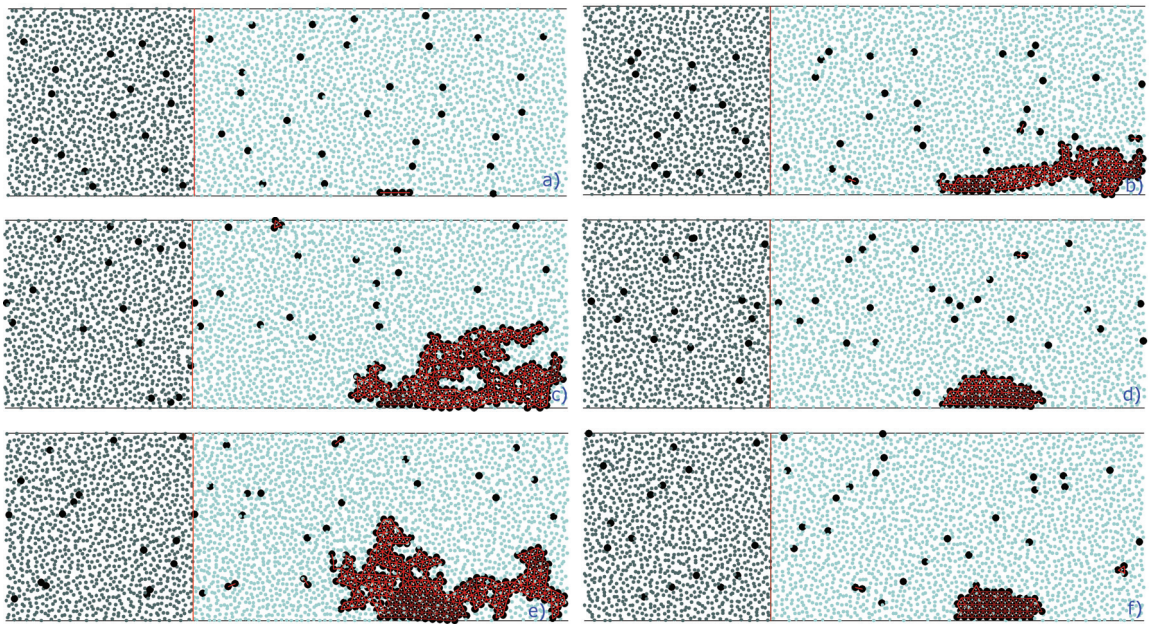

Figure 3.4: Snapshots of clot growth for step time dependent adhesion force with the adhesion resistance condition (older connections are depicted with darker red colour): a) initial clot, b) and c) elongated clot with mainly weak connections, d) clot core with mainly strong connections after rupture, e) continued clot growth, f) fully formed clot core after rupture. Reprinted with permission from [117] – *A. Tosenberger et al., Russian Journal of Numerical Analysis and Mathematical Modelling, De Gruyter, 2012.*

3.3.2 Time dependent platelet adhesion force

The use of time dependent platelet adhesion force allowed the creation of a more stable part of the clot, in which the forces between platelets are stronger than the ones between the newly connected platelets in the outer part of the clot. We will refer to this more stable part of the clot as the clot core. In the first case the time dependent platelet adhesion was modelled with a linear function (equation (3.3)). The most important stages of simulation obtained by this model are presented in Figure 3.3. Based on several platelets initially placed near the boundary the clot begins to grow. As the clot grows, the connections between platelets become stronger depending on time of their attachment to the clot. When the clot becomes large enough, and the stress on it from the flow becomes too high, the part with weaker

connections breaks off, leaving the more stable part of the clot still connected to the blood vessel wall. However, as it can be seen in Figure 3.3, the shape of the remaining part of the clot does not correspond exactly to biological observations.

In the second case, the force ageing was introduced by a step function (equation (3.4)), which can be easier to justify from the biological point of view - the transformation from weak connections between platelets to strong ones is rapid compared to the total time needed to complete the coagulation process. The key moments of the simulation done with a step function model can be seen in Figure 3.4. The clot grows and at the same time the core of the clot forms. After removing the exterior part of the clot by the flow, the clot core stays attached to the blood vessel wall.

The three graphs presented in Figure 3.5 show the clot growth in time for the three models studied above. The first graph corresponds to the model with the constant adhesion force coefficient. It shows how with each clot rupture, the whole clot is taken by the flow, leaving behind only the initial clot. The second graph in Figure 3.5 shows how the linear model after rupture leaves a clot core attached to the blood vessel wall. However, it also shows that the clot has a tendency to continue to grow after a rupture occurs. Finally on the last graph we can see the cloth growth for the step-function model. It shows how after some time the clot core forms, and that after several following ruptures, the core remains the same.

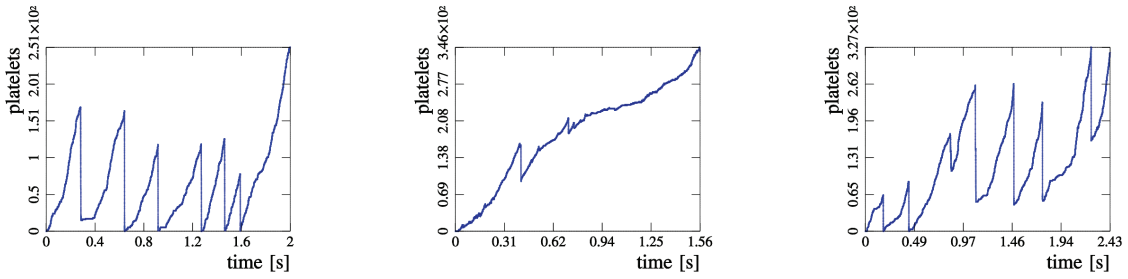

Figure 3.5: Clot growth and breakage for three different platelet adhesion force models (from left to right): constant force coefficient, force coefficient as a linear function, force coefficient as a step function. Reprinted with permission from [117] – *A. Tosenberger et al., Russian Journal of Numerical Analysis and Mathematical Modelling, De Gruyter, 2012.*

3.3.3 Arrest of clot growth

At the next step of this modelling, the biological effect of the fibrin net covering the clot core is taken into account, i.e. platelets covered by fibrin polymers become resistant to new bindings of platelets that are circulating in the flow [71]. In this model the blood coagulation pathways are not explicitly described. Thus, in the terms of the step function model, aggregated platelets which are bound by the stronger force can be considered as

being part of the clot core. Therefore, the resistance effect is modelled as the inability of the aggregated platelets to form new connections once they have established a stronger connection with any other platelet.

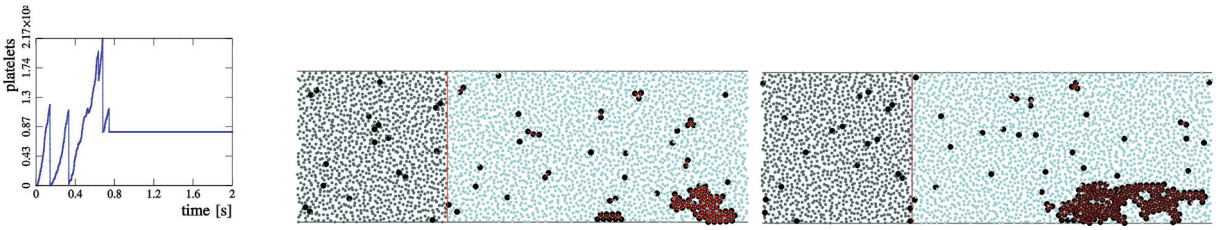

Figure 3.6: Clot growth and breakage for the step-function model with the added resistance of the clot core to adhesion of new platelets. Clot mass as a function of time (left) and final form of the clot for two sets of parameters (middle and right). Reprinted with permission from [117] – *A. Tosenberger et al., Russian Journal of Numerical Analysis and Mathematical Modelling, De Gruyter, 2012.*

In this case, it is necessary to introduce an additional repulsing force between the platelets of the core and the new platelets coming from the flow. Indeed, now there exists a possibility of two platelets being in physical contact without being connected. To prevent such pairs of platelets from occupying the same space, an additional force is added between them. This force exists only if two non-connected platelets are in physical contact, i.e., the distance between their centres is less than the platelet diameter.

Figure 3.6 shows the platelet clot growth for this modified step-function model. At the first stage of clot growth, its mass increases linearly in time. Then the clot ruptures and does not change any more because new platelets cannot connect to the platelets of the clot core (Figure 3.6, left). The stages of clot growth simulated by the enhanced step model are shown on Figure 3.4, while two other final forms of the clot for different values of parameters are shown in Figure 3.6 (middle and right).

Biologically, the processes of platelet aggregation and fibrin net formation are related but are not the same. The first process involves biochemical reactions between platelets, while the second process is based on reactions between proteins that occur in blood plasma. Therefore, in the next stage of modelling the discrete model of platelet aggregation in flow, described in this chapter, will be enhanced to account for concentrations of blood factors in flow and the related reactions of blood coagulation. This has required a development of hybrid models, which are described in the following chapter.

Chapter 4

Hybrid model of blood coagulation in flow

4.1 One equation model

In this section two hybrid models of clot growth in flow are described. They couple discrete and continuous approaches. The discrete part describes blood plasma flow in a vessel and platelet aggregation by use of DPD method similar to the discrete model described in Chapter 3. The continuous part models blood coagulation pathways in flow, describing the concentrations of blood factors with a system of partial differential equations. The discrete and continuous parts are coupled via the flow velocity profile $\mathbf{v}$, measured in the discrete (DPD) part of the model, and concentration profiles obtained by the continuous (PDE) part of the model. The scheme of coupling of discrete and continuous parts of the model is shown in Figure 4.1.

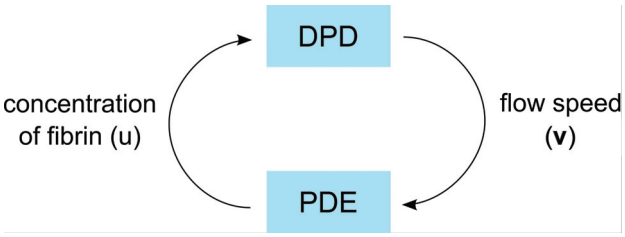

Figure 4.1: The scheme of coupling of discrete (DPD) and continuous (PDE) parts of the model.

DPD is a spatially continuous method, while the PDE system is solved numerically on a mesh. Thus a bilinear interpolation is used to calculate the fibrin concentration for the place which a particle occupies. The same interpolation method is used to calculate flow velocity in the points of the PDE numerical mesh.

4.1.1 Fibrin concentration

Following results described in Chapter 3 the step function was chosen to represent inter-platelet bonds in the hybrid model. The discrete model presented in Section 3.3.2 describes blood plasma flow, platelet aggregation, the strengthening of inter-platelet bonds due to platelet activation, possible breakage of the platelet clot and the eventual arrest of the platelet clot growth due to two effects - increase of shear flow rate near the growing platelet clot and resistance of clot core to binding of free platelets from the flow. As the discrete model does not contain a description of blood coagulation factors, the clot core was defined as the collection of activated platelets. However, the formation of the fibrin mesh is responsible for the creation of the clot core and the clot growth arrest. Hence, the next step in modelling is to describe more precisely the biological mechanisms which regulate the process of blood coagulation. Therefore, proteins which control the process of coagulation are modelled by partial differential equations. This enables the description of their production, diffusion in the flow, and interaction with the blood flow velocity field via the advection term. Because of the complexity of the coagulation process, the modelling began by introducing just one reaction-diffusion-advection equation as the continuous part of the model, where the PDE describes the concentration of fibrin in the flow:

$$\frac{\partial u}{\partial t} = \alpha \Delta u - \nabla \cdot (\mathbf{v}u) + \beta u \left(1 - u\right). \tag{4.1}$$

Here u is the protein concentration, $\mathbf{v}$ is the flow velocity, α is the diffusion coefficient, β is the reaction term coefficient. Use of one equation to describe the concentration of fibrin as the final blood factor in the coagulation regulatory network is a major simplification of the coagulation pathways. However, as a step towards a more complete model it allows studying of the interaction of the platelet aggregation and the protein concentration in the flow.

To simulate the resistance of an already formed clot to the binding of free platelets from the flow, the critical concentration of fibrin u_c is introduced. If the concentration is less then u_c, a platelet can bind with another platelet, if not, it will be resistant to adhesion [71]. Accordingly, the platelet is considered to be a part of the clot core if it is in the clot and the fibrin concentration has been larger than u_c at the position of that platelet.

The equation (4.1) describes fibrin concentration in flow and the fibrin polymer concentration is not modelled directly. As an effect, when a part of the clot ruptures, the fibrin concentration at that place can be taken by flow. After the rupture occurs, the concentration of fibrin at the place of the rupture is no longer protected by the clot, and it is therefore taken away by the flow. In the case when the previous concentration is higher than the critical level u_c, after the clot rupture and decrease in fibrin concentration the platelets that were before considered to be covered by fibrin polymer, and therefore part of the clot core adhesion resistant, would change their state to platelets not covered by fibrin polymer. As fibrin net should not degrade in the middle of the clot growth, in this model the previously

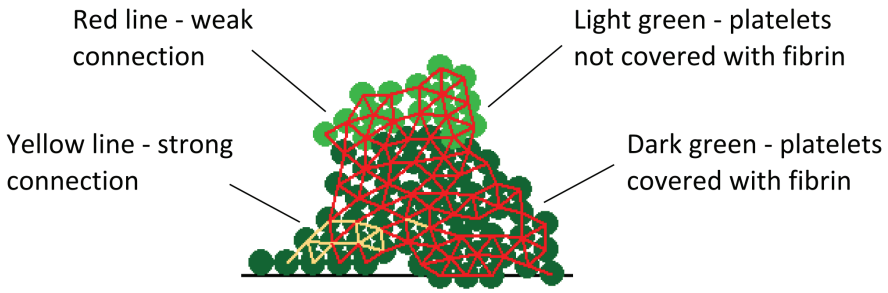

Figure 4.2: Clot structure. Connections between platelets are shown as intervals between their centers - red lines correspond to weak connections, yellow to strong ones. Dark green platelets are covered by fibrin. Reprinted with permission from [118] – *A. Tosenberger et al., Journal of Theoretical Biology, Elsevier, 2013.*

described situation is avoided by use of platelet memory - once the platelet has been covered by fibrin polymer (concentration higher that u_c) it will remain in this state independently of the future level of fibrin.

4.1.2 Clot growth

In simulations with the first hybrid model the values of parameters were chosen in such a way that they correspond to a vessel of $50\mu m$ in diameter and $150\mu m$ long. The density and the viscosity of the simulated medium were chosen to correspond to the density and viscosity of blood plasma [128] ($\approx 1.24m$Pa·s). The average velocity of the flow is chosen to be $24mm/s$. As in the discrete model, at the beginning of the simulation several stationary platelets are positioned next to the lower vessel wall in order to initiate platelet aggregation. As it was the case in the discrete model the size of all DPD particles was set to correspond to the size of platelets ($\approx 1\mu$m in diameter). Figure 4.2 shows a typical clot structure obtained in simulations. There are two types of platelet connections: weak (red lines between their centers) and strong (yellow lines). Strong connections appear if a platelet has already weak connections during some time. Hence platelet activation and emergence of strong connections is modelled as a time delay. The disconnection distance d_D for inter-platelet connections was set to 1.3 times of the platelet diameter. Platelets covered by fibrin are shown with dark green color, while platelets not covered by fibrin with light green.

Several stages of the clot growth and the evolution of the fibrin concentration profile protected by the clot are shown in Figure 4.3 and Figure 4.4. In the beginning of clot growth, platelets aggregate at the injury site due to weak connections (Figure 4.3, a). The injury site is modelled as several platelets attached to the vessel wall. They initiate clot growth. Since the flow velocity is sufficiently high, the concentration u of fibrin remains low (Figure 4.4, a). The platelet clot continues to grow due to weak connections and the flow speed inside it decreases. It makes it possible for the coagulation reaction to start, and fibrin concentration

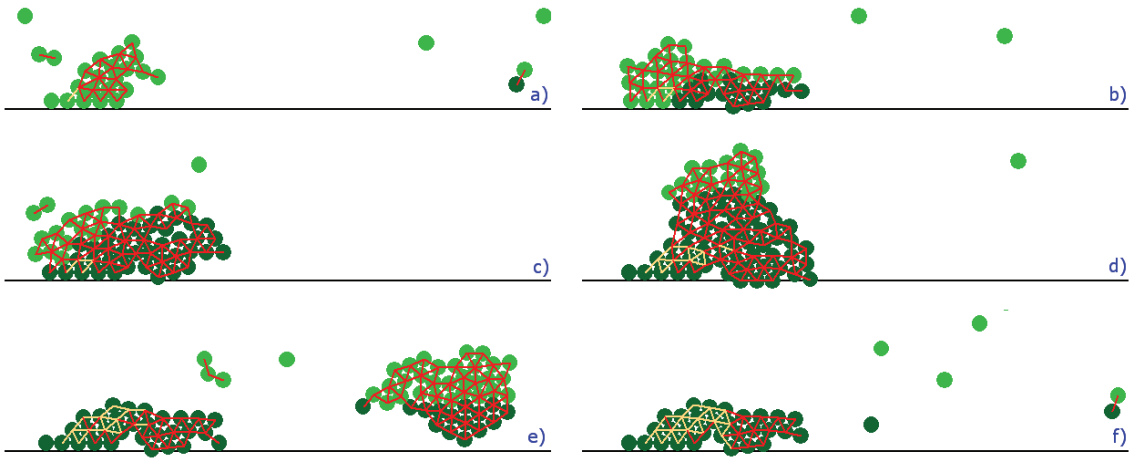

Figure 4.3: Snapshots of the clot growth for the hybrid model: a) the clot begins to form, b) fibrin begins to cover the growing clot, c) clot core is covered by fibrin but the clot continues to grow, d) the clot reaches its critical size, e) the clot ruptures and its outer part is taken by the flow, f) the core of the clot remains captured in the fibrin mesh, which prevents the clot from growing further. Reprinted with permission from [118] – *A. Tosenberger et al., Journal of Theoretical Biology, Elsevier, 2013.*

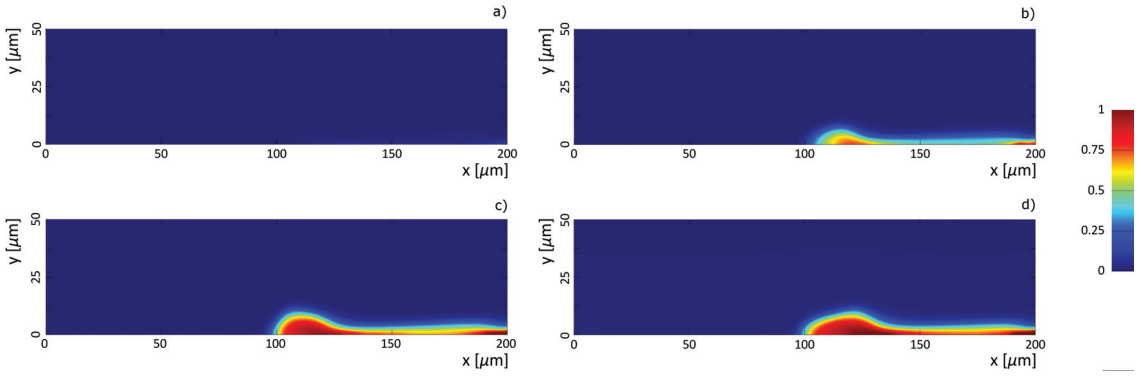

Figure 4.4: The evolution of the concentration profile in the hybrid model (from a) to d)) with non-dimensional concentration scale on the right. As the clot grows, it protects fibrin from being taken away by the flow. Reprinted with permission from [118] – *A. Tosenberger et al., Journal of Theoretical Biology, Elsevier, 2013.*

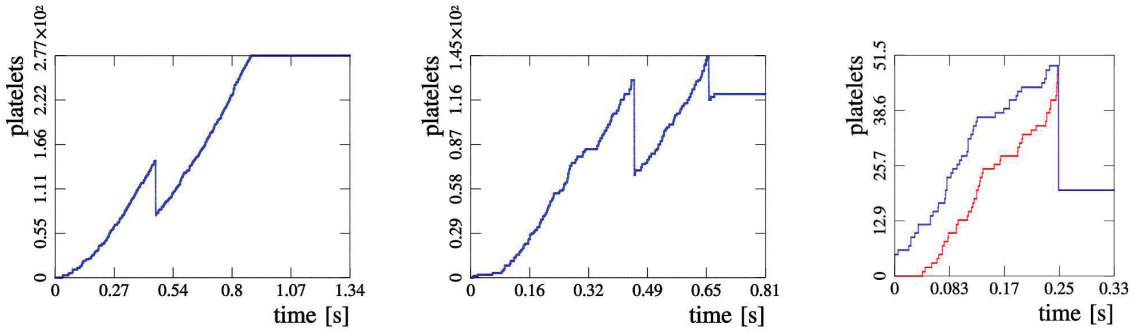

Figure 4.5: Two cases of clot growth arrest in hybrid model: the fibrin mesh covers the whole clot and stops its growth (left), the clot cap breaks and a part of it is removed by the flow leaving the clot core captured in the fibrin mesh (middle). On the right, an example of the clot growth (blue) is shown together with the clot core (red). In order to reduce simulation time the number of platelets per unit volume is greatly increased and the time delay t_c in the equation (4.22) is decreased for the same rate. As a consequence, the clot growth in simulation is accelerated (see time scales on the graphs). This does not influence the results from the qualitative point of view. Reprinted with permission from [118] – *A. Tosenberger et al., Journal of Theoretical Biology, Elsevier, 2013.*

gradually increases (Figures 4.3, b and 4.4, b). This process continues while the clot becomes sufficiently large (Figures 4.3, c, d and 4.4, c, d). Fibrin covers a part of the clot and strong platelet connections appear inside it. Flow pressure exerts mechanical stresses on the clot and weak connections can rupture. In this case the clot breaks and its outer part is removed by the flow (Figures 4.3, e). Its remaining part is covered by fibrin and it cannot attach new platelets. The final clot form is shown in (Figures 4.3, f).

The described process of clot growth shows several important sub-processes of blood coagulation. Inside the early platelet aggregate the flow velocity is significantly decreased, hence the blood factor concentration is being protected from the flow. This allows for the coagulation cascade to commence inside the clot, resulting in the creation of the clot core. As the clot core evolves, it also supports further clot growth, as without it the platelet aggregate would reach a certain size and then rupture prematurely, leaving the wound unhealed. Figure 4.4 shows an example of the evolution of the fibrin concentration profile which is protected by a growing clot. Furthermore, the model shows a possible way of clot growth arrest. As the clot grows, the vessel becomes narrower and the pressure induced on the clot by the flow increases. Once the pressure becomes too high the outer weakly bound part of clot can rupture, leaving only the clot core which is adhesion-resistant, thus stopping the clot growth.

In simulations a wide range of model parameters was studied to account for possible behaviours of the model, including the parameters of the reaction-diffusion equation (equation (4.1)) and parameters related to platelet aggregation (equation (4.22)). The following ranges of values were tested: $f_w^A \in [0.8, 10]$ nN $(= 10^{-9}\text{N})$, $f_s^A \in [5, 50]$ nN, $t_c \in [100, 300]$

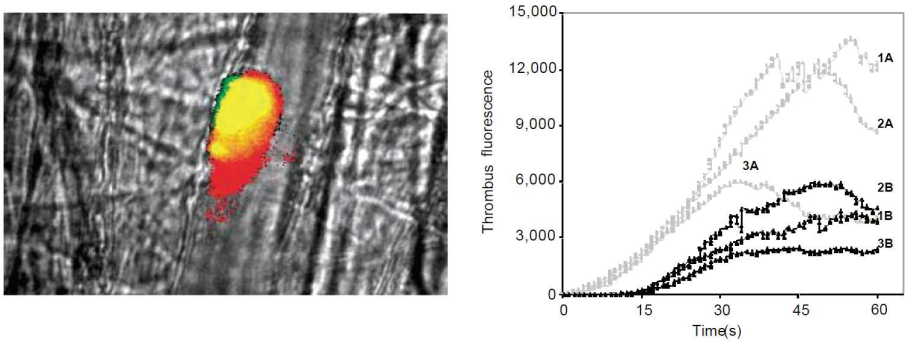

Figure 4.6: Experimental results from Falati et al. (2002) [43]: on the left, platelets (red) and fibrin (green) and their co-localization (yellow) in a forming clot (flow direction is from top to bottom); on the right, the time course of incorporation of platelets (A) and fibrin (B) into arterial thrombi for three separate cases (denoted by 1,2,3). Reprinted and adapted by permission from Macmillan Publishers Ltd: Nature Medicine (Falati et al., Nature Medicine 8: 1175 - 1180, 2002), © (2002).

ms, $\alpha \in [0.006, 0.06]$ $m\text{m}^2/\text{min}$, $\beta \in [0.0006, 0.042]$ $m\text{m}^2/\text{min}$, $u_c \in [0.1, 0.9]$. The values of the parameters related to inter-platelet bonds (f_w^A, f_s^A, t_c) are close to the values observed in a study by Pivkin et al. [98]. As protein regulatory network is approximated by a single reaction-diffusion-advection equation, its parameters are not directly related to experimentally observed values.

However, taking into account the time scaling explained in Section 3.1.2 (increased platelet density and reduced t_c), the values of diffusion coefficient α used in simulations are close to the data in [75, 84].

Depending on the choice of parameters, several clot growth patterns can be obtained. In the first case, when the diffusion coefficient is too large and the reaction coefficient is too small, the concentration can be removed by the flow before the clot starts growing and protects the concentration. The second regime is when the concentration production and diffusion rates are such that fibrin gradually covers the clot, but it is slower than the clot growth. In that case, when the clot becomes too large to sustain the pressure from the flow, the cap of the clot breaks, leaving the core of the clot covered with fibrin, which stops further clot growth (Figure 4.5 middle). In the third case, when the rates of concentration production and propagation in the flow are high, the clot grows without rupture until it is completely covered by fibrin (Figure 4.5 left). The graph on the right side of Figure 4.5 shows the growth of the clot and the clot core in time. The clot growth (excluding the clot growth initiation and stop stages) is almost linear, while the clot core grows approximatively at the same rate as the clot itself. This is also observed in the experimental results obtained by Falati et al. [43] shown in Figure 4.6 (right). Figure 4.6 (left) shows that, while the clot grows, the formation of fibrin happens inside the clot, and it is protected by the aggregated platelets.

The second of the three described model behaviours corresponds well to the hypothesis that the clot growth is stopped by the rupture of its covering layer. Figure 4.3 shows an example in which the clot core is covered by fibrin, and the clot growth is stopped after the rupture of its cap.

4.2 Three equations model

4.2.1 Coagulation pathway model

At the next stage of modelling a simplified phenomenological model, shown in Figure 4.7, was used to describe the protein blood coagulation regulatory network. The model consists of self-accelerated production of thrombin from prothrombin, and the fibrin cascade which is influenced by the thrombin concentration. Instead of one reaction-diffusion-advection equation from the previously described model, a system of differential equations is developed in order to account for the main characteristics of blood coagulation pathway.

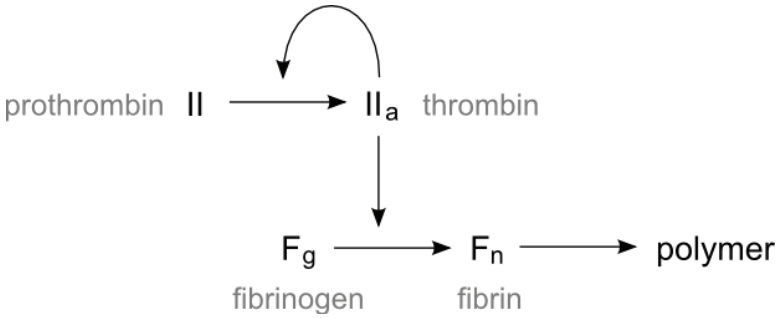

Figure 4.7: The simplified pathway of blood coagulation, as it is described in the model. The full pathway of blood coagulation in vivo is presented in Figure 1.7 in Section 1.2. Reprinted with permission from [118] – *A. Tosenberger et al., Journal of Theoretical Biology, Elsevier, 2013.*

Thrombin reaction. The thrombin reaction can be described in a simple form as follows:

$$T + II \rightarrow 2T, \tag{4.2}$$

where T is the concentration of thrombin and II the concentration of prothrombin. It takes into account the self-accelerating properties of thrombin production. Then kinetic equations

$$\frac{dT}{dt} = k_1 T \cdot (II), \qquad \frac{d(II)}{dt} = -k_1 T \cdot (II) \tag{4.3}$$

give the balance of mass $T + (II) = C_0$, where C_0 is the initial concentration of factor II. Therefore the thrombin reaction can be written as:

$$\frac{dT}{dt} = k_1 T(C_0 - T). \tag{4.4}$$

If diffusion of thrombin and prothrombin occurs with the same diffusion coefficient, then the balance of mass is preserved. The same is valid for advection.

Instead of the reaction (4.2), the following reaction can be considered:

$$II \to T, \tag{4.5}$$

with the reaction constant $k_1 = k_1(T)$ which depends on the concentration of thrombin. This leads to an equation similar to (4.4), where the product $k_1 T$ is replaced by the function $k_1(T)$:

$$\frac{dT}{dt} = k_1(T)(C_0 - T). \tag{4.6}$$

In order to describe thrombin degradation, which is not taken into account in the equation (4.6), an approximate equation can be considered

$$\frac{dT}{dt} = k_1(T)(C_0 - T) - \sigma T, \tag{4.7}$$

which describes thrombin degradation but does not follow precisely from kinetic equations. Such approximation is used in combustion theory and it allows one to consider a bistable case with two stable stationary points. In order to study blood coagulation in flow (in vivo), diffusion and advection terms are added to the equation (4.7):

$$\frac{dT}{dt} + \nabla \cdot (\vec{\mathbf{v}} \cdot T) = D_T \Delta T + k_1(T)(C_0 - T) - \sigma T, \tag{4.8}$$

where D_T is the thrombin diffusion coefficient, $\vec{\mathbf{v}}$ is the velocity field. As blood plasma is considered to be incompressible, i.e. with zero divergence, the advection can be simplified, thus obtaining the following equation for thrombin concentration:

$$\frac{dT}{dt} + \vec{\mathbf{v}} \cdot \nabla T = D_T \Delta T + k_1(T)(C_0 - T) - \sigma T, \tag{4.9}$$

Fibrin reactions. Consider, next, the reactions

$$F_g \to F_n \to F_p, \tag{4.10}$$

where F_p is fibrin polymer. Unlike thrombin which is produced locally at the injury site and inside the the clot, fibrinogen is synthesized in the liver and constantly circulates in the blood stream. The availability of thrombin, as an enzyme, is necessary to produce fibrin from fibrinogen. Therefore, it is important to take into account the flow influence on both concentrations - thrombin and fibrinogen. We omit fibrin in the reaction scheme (4.10) and consider instead a simplified reaction $F_g \to F_p$. Then, the reaction can be represented by the following model:

$$\frac{\partial F_g}{\partial t} + \vec{\mathbf{v}} \cdot \nabla F_g = D_{F_g} \Delta F_g - k_3(T) F_g, \tag{4.11}$$

$$\frac{\partial F_p}{\partial t} = k_3(T) F_g, \tag{4.12}$$

where D_{F_g} is the fibrinogen diffusion coefficient, and $k_3(T)$ is the reaction constant which depends on the concentration of thrombin. The equation (4.11) describes fibrinogen diffusion in flow, and the equation (4.12) describes the concentration of fibrin polymers which form an insoluble network and thus do not diffuse or flow.

Coagulation pathway model. By combining the equation(4.9) for thrombin concentration, and equations (4.11) and (4.12) for fibrinogen and fibrin polymer concentrations respectively, one obtains the following model:

$$\begin{aligned} \frac{dT}{dt} + \vec{\mathbf{v}} \cdot \nabla T &= D_T \Delta T + k_1(T)(C_0 - T) - \sigma T, \\ \frac{\partial F_g}{\partial t} + \vec{\mathbf{v}} \cdot \nabla F_g &= D_{F_g} \Delta F_g - k_3(T) F_g, \\ \frac{\partial F_p}{\partial t} &= k_3(T) F_g. \end{aligned} \tag{4.13}$$

In order to model the self-amplifying thrombin reaction, the reaction function $k_1(T)$ is defined as follows:

$$k_1(T) = k_1^0 \frac{T^2}{T_0 + T}, \tag{4.14}$$

where k_1^0 and T_0 are constants. The function (4.14) is based on the Michaelis–Menten equation, but at low thrombin concentration it has a lower gradient, as shown in Figure 4.8. While the thrombin equation (equations (4.13) would form a monostable problem with the Michaelis-Menten term, with the term from equation (4.14) it is forms bistable problem. Thus, if the thrombin concentration is too low, with time it will converge to zero.

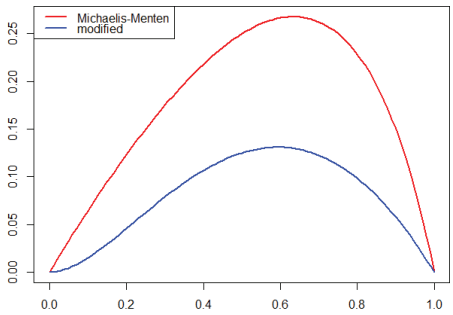

Figure 4.8: Comparison of reaction terms in Michaelis–Menten equation (red) and equation (4.13) (blue) for the same values of coefficients.

The fibrin reaction rate coefficient $k_3(T)$ is for simplicity taken to be linear:

$$k_3(T) = k_3^0 T. \tag{4.15}$$

In both the initiation and the amplification phase of blood coagulation in vivo a complex pathway precedes the prothrombin-thrombin reaction. In the initiation phase this part of the pathway is initiated by tissue factor which is normally present in sub-endothelial fibroblasts, injured vascular endothelium and activated monocytes. Once the vessel wall is injured tissue factor enters the blood flow nearby and starts the coagulation cascade. In the amplification phase thrombin concentration acts as enzyme in the activation of cofactors which accelerate the prothrombin-thrombin reaction, thus causing an explosive increase in thrombin concentration. The self-amplification effect of the thrombin reaction is modelled by equation (4.14). In order to model the localized generation of thrombin near the vessel injury site, in the model the initial value of the thrombin concentration is set to zero in the whole domain except on the part of boundary where the injury site is located and where the concentration is set to a non zero value (equation (4.17)). As the thrombin concentration equation (equation (4.9)) is bistable, the initial non-zero concentration at the boundary has to be high enough to start the thrombin accumulation, otherwise the concentration will quickly decrease to zero. At all domain boundaries Neumann boundary conditions are used:

$$\frac{\partial T}{\partial x}\Big|_{x=0,L} = \frac{\partial T}{\partial y}\Big|_{y=0,D} = 0 \tag{4.16}$$

$$T(x,y,t)\Big|_{t=0} = \begin{cases} 1, & \text{if } x \in [w_B, w_E] \text{ and } y = 0, \\ 0, & \text{if } x \notin [w_B, w_E] \text{ or } y \neq 0, \end{cases} \tag{4.17}$$

where $[0, L] \times [0, D]$ is the simulation domain, i.e. a part of blood vessel of the length L and diameter D, and where $[w_B, w_E] \times \{0\}$ is the part of domain representing the vessel injury site.

The primary function of thrombin is the conversion of fibrinogen to fibrin. Fibrinogen, being synthesised in the liver by hepatocytes, is constantly present in a healthy bloodstream. Therefore, in the model, the initial concentration of fibrinogen is set to some value F_g^0 in the whole domain and at the inflow boundary Dirichlet boundary conditions are used, while the remaining boundaries are described with zero Neumann boundary conditions:

$$\frac{\partial F_g}{\partial x}\Big|_{x=L} = \frac{\partial F_g}{\partial y}\Big|_{y=0,D} = 0, \tag{4.18}$$

$$F_g\Big|_{x=0} = F_g^0, \tag{4.19}$$

$$F_g(x,y,t)\Big|_{t=0} = F_g^0. \tag{4.20}$$

4.2.2 Platelet aggregation

The first hybrid model described only two levels of inter-platelet bonding strengths – the weaker adhesion bond and the stronger bond between activated platelets. In the second hybrid model the fibrin polymer concentration is introduced. To describe the effects of the fibrin net on the aggregated platelets two new conditions are added. The first one is the adhesion resistance effect present in platelets that are coated in fibrin polymers. Instead of the critical concentration constant u_c used in the first hybrid model, a similar constant c_{F_g} is introduced. c_{F_g} denotes the critical fibrin polymer (F_p) concentration, above which it is considered that the fibrin net has been formed. Hence, platelets that are considered to be covered by the fibrin net become adhesion resistant. The second effect of the fibrin net is that it reinforces the platelet aggregate. Therefore, a third level of strength of inter-platelet bonds is introduced in the model describing the aggregated platelets covered by the fibrin net. Following the description, the adhesion force is modelled as a pairwise force between two platelets expressed in the form of Hooke's law:

$$\mathbf{F}_{ij}^{A} = f^{A}(t_{ij}) \left(1 - \frac{r_{ij}}{d_C}\right) \hat{\mathbf{r}}_{ij}, \tag{4.21}$$

where f^A is the force strength coefficient and d_C is the force relaxation distance which is equal to two times the physical radius of the platelets. As platelet binding occurs due to their surface adhesion receptors, two platelets in a flow connect when they come in physical contact, i.e. $r_{ij} \leq d_C$ (connection criterium). Platelets remain connected until their distance does not exceed a critical value d_D (disconnection criterium) which is greater than d_C. We set d_D equal to 1.3 times of the platelet diameter. The force strength coefficient f^A in equation (4.21) is modelled in the following way to describe three strengths of inter-platelet bonds:

$$f^{A}(t_{ij}) = \begin{cases} f_1^A & \text{if } F_p(i) \text{ or } F_p(j) < c_{F_p}, \quad \text{and} \quad t_{ij} < t_c, \\ f_2^A & \text{if } F_p(i) \text{ or } F_p(j) < c_{F_p}, \quad \text{and} \quad t_{ij} \geq t_c, \\ f_3^A & \text{if } F_p(i) \text{ and } F_p(j) \geq c_{F_p}, \end{cases} \tag{4.22}$$

where $f_1^A < f_2^A < f_3^A$ are the three strengths of inter-platelet connections, representing respectively a weak bond due to GPIb receptors, a medium bond due to platelet activation and a strong bond due to the reinforcement by the fibrin polymer net. t_c is the time needed for platelet activation measured from the moment when the connection is established. As the platelet activation process is not at the focus of this study at the moment, the activation period serves as a basic approximation of the platelet activation process due to the contact and proximity of other activated platelets. $F_p(i)$ and $F_p(j)$ are levels of fibrin polymer F_p at positions of particles i and j respectively. c_{F_p} is the critical level of fibrin polymer. A platelet is considered to be a part of the clot core if it is in the clot and the fibrin concentration has been larger than c_{F_p} at the position of that platelet. Therefore, the clot core is a part of the clot covered by a concentration of F_p larger than c_{F_p}. As the platelets that are coated with fibrin are adhesion resistant, the same condition is applied in the model on the platelets in the core which cannot establish new bonds. In the case of physical contact between two platelets that are not connected, one of which is non-adhesive, an additional repulsing force has to be introduced between them in order to prevent them from occupying the same space.

4.2.3 Parameters

A typical clot structure is shown in Figure 4.9. There are three types of platelet connections, weak (light red lines between their centres), medium (dark red lines) and strong (black lines). Medium connections appear if platelets are weakly connected during the time period t_c. Hence we model the platelet activation and emergence of medium connections as a time

delay. Platelets covered by fibrin are shown with dark green color, platelets not covered by fibrin with light green.

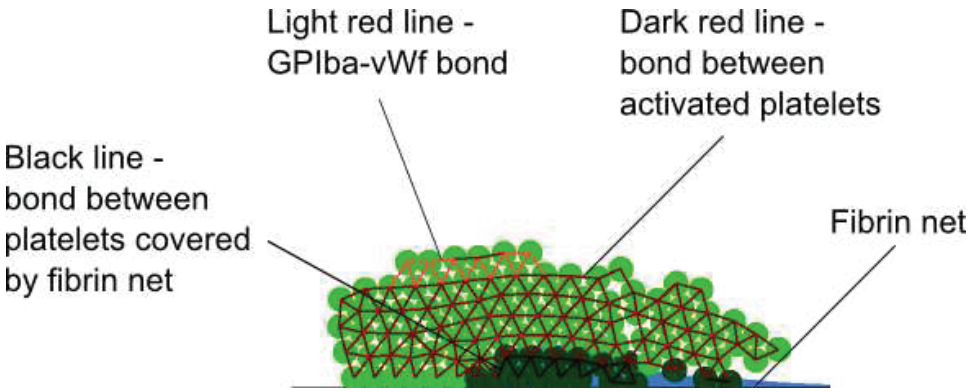

Figure 4.9: Clot structure. Connections between platelets are shown as red intervals between their centres. Light red lines correspond to weak GPIb connections, dark red to medium connections between activated platelets, and black to strong connections between platelets covered by the fibrin net. Dark green platelets are covered by the fibrin net, which is marked by blue color.

In the basic simulation the values of parameters were chosen in such a way that they correspond to the vessel of $50\mu m$ in diameter and 200 to 300 μm long. The density and the viscosity of the simulated medium were chosen to correspond to the density and viscosity of blood plasma [128] ($\approx 1.24 m$Pa·s). The average velocity of the flow is chosen to be 18.75 mm/s, which in a vessel of $50\mu m$ in diameter produces a wall shear rate of 1500 s^{-1}. To initiate clotting, at the beginning of the simulation, several stationary platelets are positioned next to the lower vessel wall. Table 4.1 lists all the values of parameters chosen for the basic simulation. The values are considered in the following system of physical units: μm=10^{-6}m, pg=$10^{-14}kg$, and 10^{-2}s. As the pathways model is phenomenological, the concentration scale is left in the undimensional form. In the table the values of all parameters are expressed in both forms - as used in the simulations and interpreted in the standard SI units system.

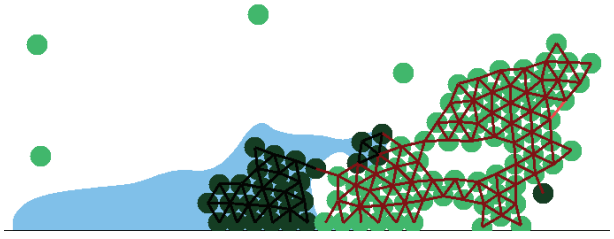

Figure 4.10: Fibrin net generated outside of the platelet aggregate due to high production of thrombin and its significant propagation outside of the growing clot.

For any given flow properties, depending on the values of parameters of concentration

DOMAIN	Value	Physical	Description
L	200	200 μm	length of the simulated blood vessel
L_{GA}	50	50 μm	length of the Particle Generation Area (GA)
D	50	50 μm	diameter of the simulated blood vessel
G_x	7200	72 m/s^2	external force in x direction used to induce flow
$\bar{v}_x$	187.5	18.75 mm/s	average flow velocity
w_x		1500 s^{-1}	wall shear rate
DPD	Value	Physical	Description
a_{ij}	600000		conservative force coefficient
γ	3550		dissipative force coefficient
σ	20000		random force coefficient
r_c	5		force cut-off radius
k	1		exponent in the equation (2.6)
k_BT	1		the Boltzmann constant times temperature
n	0.36		particle number density
m	0.463		particle mass
dt_{DPD}	0.001		DPD time step
PDE	Value	Physical	Description
dx	0.5	0.5 μm	spatial step
dt_{PDE}	0.01	0.1 ms	PDE time step
D_T	0.5	0.003 mm/min	thrombin diffusion coefficient
k_1^0	5.5	$3.3 \cdot 10^4$ min^{-1}	thrombin reaction term coefficient
T_0	0.1		thrombin reaction term coefficient
C_0	1		thrombin reaction term coefficient
σ	2	$1.2 \cdot 10^4$ min^{-1}	thrombin degradation coefficient
D_{F_g}	0.5	0.003 mm/min	fibrinogen diffusion coefficient
k_3^0	0.001	6 min^{-1}	fibrinogen reaction term coefficient
c_{F_p}	0.8		critical fibrin polymer level
OTHER	Value	Physical	Description
f_1^A	$3 \cdot 10^6$	0.3 nN	weak inter-platelet bond coefficient
f_2^A	$8 \cdot 10^6$	0.8 nN	activated inter-platelet bond coefficient
f_3^A	$1 \cdot 10^8$	10 nN	fibrin net reinforced bond coefficient
t_c	10	0.1 s	platelet activation period
τ	10	0.1 s	DPD-PDE data exchange period
p	0.017	$3.672 \cdot 10^12$ L^{-1}	platelet frequency

Table 4.1: Values of all parameters in the basic simulation.

equations, there exist two limiting concentration propagation scenarios. In the first scenario the thrombin concentration decreases due to diffusion, degradation and outflow until it rests at zero value in the whole domain. As the final result, the fibrin net does not form. In the second scenario the thrombin generation is to high, resulting in the thrombin propagation outside of the platelet aggregate and finally in a rapid formation of a fibrin net outside of the platelet clot (Figure 4.10). In order to study the interaction of clot growth and fibrin polymer formation, in the basic simulation the values of parameters of concentration equations are chosen so that the limiting scenarios do not occur. Some of the parameters, like the diffusion coefficients, were taken from the continuous coagulation pathways model by Krasotkina et al. [75].

4.2.4 Model behaviour

Several stages of the clot growth and the evolution of thrombin, fibrinogen and fibrin polymer concentration profiles protected by the clot are shown in Figure 4.11 and Figure 4.12. In the beginning of clot growth, platelets aggregate at the injury site due to weak connections. The injury site is modelled as several platelets attached to the vessel wall. They initiate platelet clot growth. The platelets gradually become activated enabling the aggregate to grow. The flow velocity inside the newly formed platelet aggregate decreases, and becomes insignificant compared to the bulk flow velocity. This makes it possible for the coagulation reactions to commence, and the thrombin concentration gradually increases due to the self-accelerated reaction (equations (4.13) and (4.14)). With thrombin present, the production of fibrin polymer from fibrinogen (and implicitly fibrin) begins, and fibrin polymer accumulates inside the platelet clot. When F_p concentration exceeds the critical level c_{F_p}, it is considered that the fibrin net and with it the clot core have been formed at that place. By this mechanism, a fibrin net forms inside the platelet clot and reinforces the inter-platelet bonds, creating the clot core and allowing the further growth of the clot. The growing clot narrows the blood vessel. As a result, the pressure from the flow on the clot (or rather its top) is being increased. The platelet aggregates, which are on the outer part of the clot and are not yet covered by the fibrin net, come under a much higher pressure and are taken by the flow one by one. This leaves the part of the clot covered by fibrin net revealed to the flow. As the platelets covered by fibrin polymer are non-adhesive [71], the platelet clot growth is stopped. The clot core can also remain covered by a thin layer of activated platelets. Nonetheless, the growth of the clot is stopped as new platelets cannot attach due to the increased flow speed. The arrest of the platelet clot growth, and the flow around it stop the growth of the fibrin net (clot core).

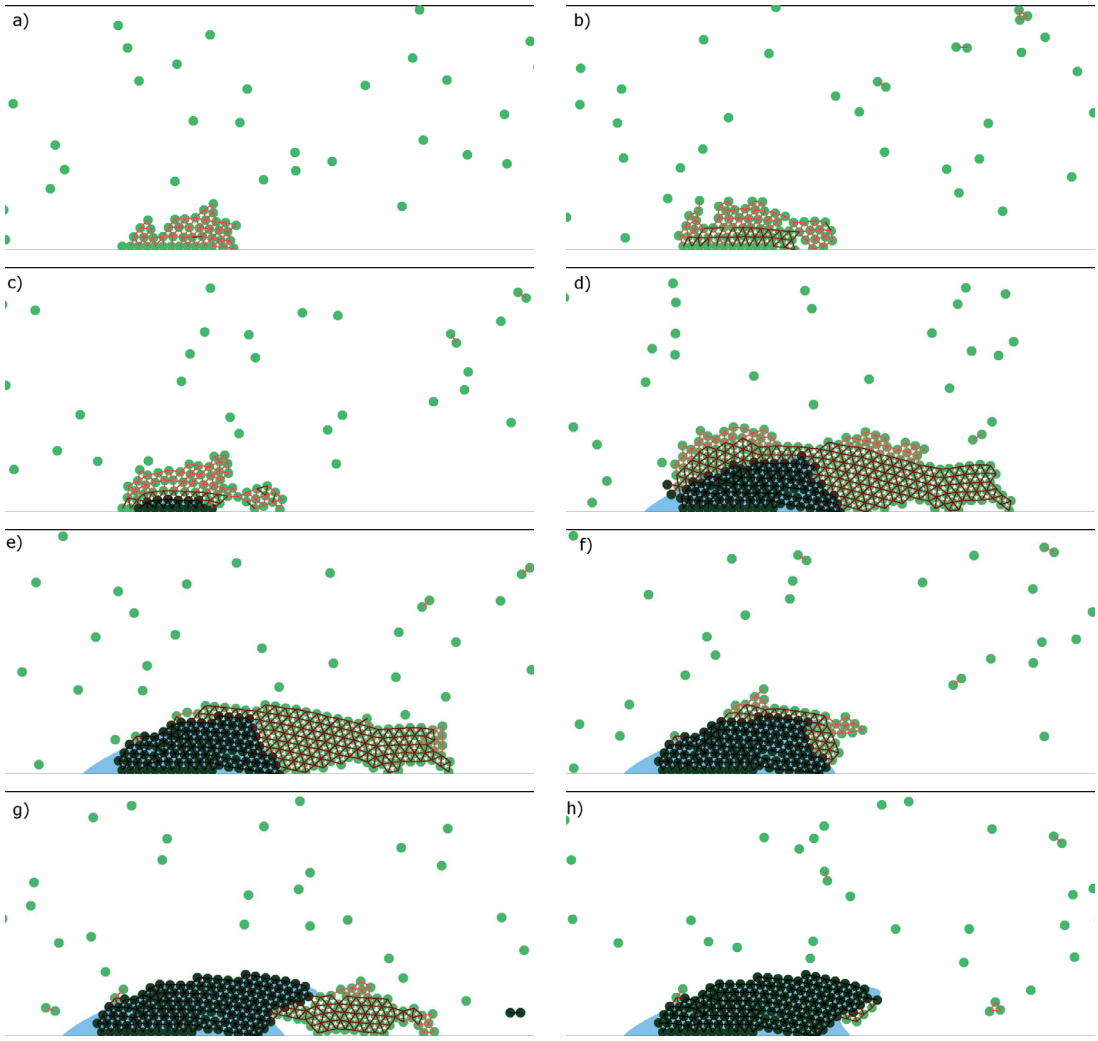

Figure 4.11: Example of a clot growth with indicated fibrin polymer level. Snapshots of the clot growth for the hybrid model: a) the clot begins to grow by the formation of a platelet aggregate, b) some of the platelets activate allowing the clot to grow larger, c) fibrin begins to cover the growing clot allowing the clot to grow further, d) the clot reaches its critical size, e,f,g) parts of clot not covered by the fibrin net rupture and are taken by the flow, h) the last rupture leaves only the adhesion resistant clot core, which prevents the clot from growing further.

In simulations the platelet concentration is set to $3.672 \cdot 10^{12}$ L^{-1} which is 9.17 to 24.48 times higher than the experimentally observed concentration [92]. This is done to obtain a full clot evolution in less simulation time. However, in the model platelets are uniformly distributed in the vessel cross-section, while in vivo they are concentrated closer to the vessel wall because they are pushed there by erythrocytes [15, 16]. Hence, the acceleration of clot growth in simulations is lower then the nominal increase in the platelet concentration. All

this does not change the qualitative clot evolution, but affects all measurements expressed in time that are related to platelets. The most important values that are affected are the core growth rate (expressed in platelets per second) and the platelet activation time t_c.

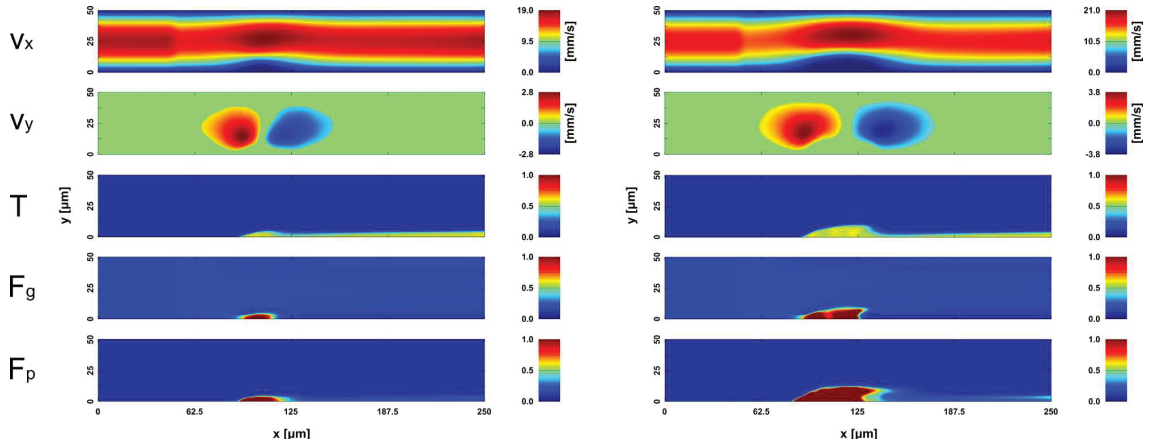

Figure 4.12: Velocity and concentration profiles for two stages of clot growth: clot in growth (left) and after the growth arrest (right). From top to bottom: the component of velocity tangential to the vessel wall, the component of velocity orthogonal to the vessel wall, thrombin concentration, fibrinogen concentration, fibrin polymer concentration.

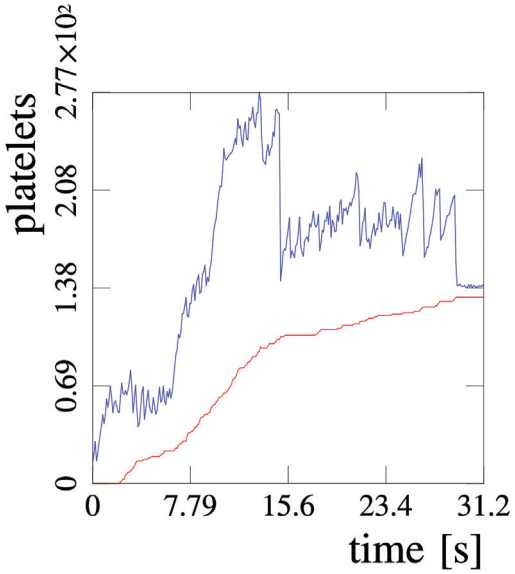

Figure 4.13: Platelet clot (blue) and clot core (red) growth in time. Oscillations in the platelet clot size occur because a part of the clot or individual platelets can be detached by the flow.

4.2.5 PDE parameters

As mentioned before (in Section 4.2.3), for the basic simulation the values of parameters of the concentration equations were chosen following several criteria. Firstly, the diffusion coefficients were set to correspond to the values used in the continuous coagulation pathways model by Krasotkina et al. [75]. Secondly, the model takes into account only the effect the fibrin polymer concentration has on platelets, while its influence on blood plasma is not modelled. Because of that the model cannot describe correctly the evolution of fibrin net without the platelet aggregate. Therefore, the remaining parameters were set in such a way that the thrombin concentration does not propagate counterflow, as the counterflow propagation would result in the formation of a fibrin net outside of the platelet clot. This effect occurred in simulations in which the flow velocity was varied, which are described later in Section 4.2.7. Thirdly, the values were adjusted so that the fibrin net generation and the formation of the clot core occur in a time frame which is close to the experimentally observed clot growth times [43]. The values are listed in the Table 4.1.

Taking the chosen values as a starting point, a study was carried out to see the influence of each parameter on clot growth and fibrin net formation. Figure 4.14 and Figure 4.15 show the final clot core size and the clot core height for different values of each of the parameters of the concentration equations. The clot core height is measured at the place where the clot core is the widest, and the value is normalized by the vessel diameter. The diffusion coefficient study (Figure 4.14 a)), where both the thrombin and the fibrinogen coefficient were varied together, shows that as the rate of diffusion increases the clot core size decreases. For a higher diffusion rate more thrombin is taken away by the flow, while the thrombin concentration protected by the platelet aggregate rises more slowly due to loss of the diffused part. As a result the fibrin polymer production is slower, and finally the final core size is lower at the moment when the weakly aggregated part of the clot ruptures leaving only the non-adhesive part. On the other hand, too small diffusion coefficients enable the more rapid generation of thrombin and, eventually, its counterflow propagation, leading to the formation of a fibrin net in the flow.

The variation of the thrombin reaction term coefficient k_1^0 (Figure 4.14 b)) shows that for the low values the core is unable to develop as the thrombin concentration quickly goes to zero due to the degradation factor γ. For the two highest values of k_1^0 shown on the graph the core size is similar to the basic case, but the thrombin propagates counterflow, again resulting in the formation of a fibrin net outside of the clot.

The graph for the fibrin production coefficient k_3^0 (Figure 4.14 c)) shows that in the case of too low production rate the size of the core decreases. This is due to slow fibrin net formation which results in a smaller core size at the moment when the weakly bound part of the clot is detached by the flow. The higher values of k_3^0 result in approximately constant core size since the reaction is rapid enough to consume all the available fibrinogen quickly at places where thrombin level is high.

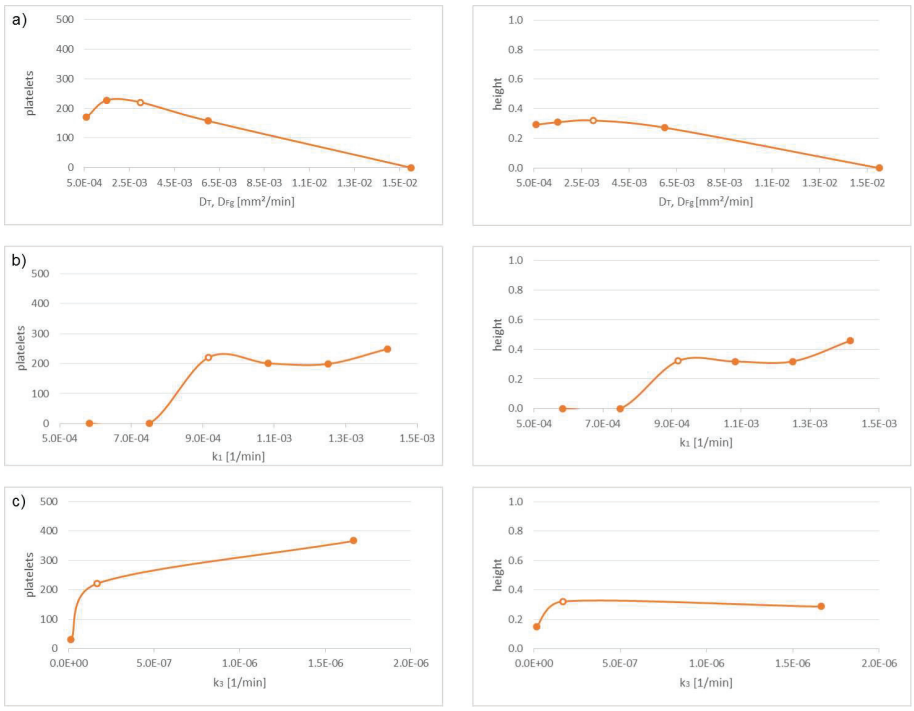

Figure 4.14: Variation of values of PDE parameters: a) diffusion coefficients of thrombin D_T and fibrinogen D_{F_g} (varied together), b) thrombin reaction rate coefficient k_1^0 and c) fibrin polymer reaction rate coefficient k_3^0. Graphs on the left side show final clot size expressed in number of platelets, while the graphs on the right side show the maximal height of the final clot, normalized by the vessel diameter. Empty points denote the result of the single basic simulation with values of parameters given in Table 4.1 (see Appendix).

The study of the influence of the thrombin degradation coefficient σ (Figure 4.15 a)) shows that a too high rate of degradation results in a rapid reduction of thrombin concentration to the zero value, thus disabling the core development. On the other hand, the lower values result in the counterflow thrombin propagation. The rapid thrombin degradation effect is also present in the case of higher T_0 values.

Figure 4.15 b) shows the effect of the variation of initial fibrinogen concentration, which is also the normal fibrinogen concentration in the undisturbed flow. The graph shows that the core size increases with the increase of the value of F_g^0. This is the effect of a more rapid core development, which is still slower than the growth of the platelet aggregate. For a too low value of F_g^0 the fibrin clot is unable to develop as the whole platelet aggregate breaks off before the fibrin net is able to form. It is notable that in all of the parameter variations the core height graph is similar to the corresponding core size graph. This indicates that the clot core height and length ratio remains similar in all cases and is not strongly affected by the underlying coagulation pathways model.

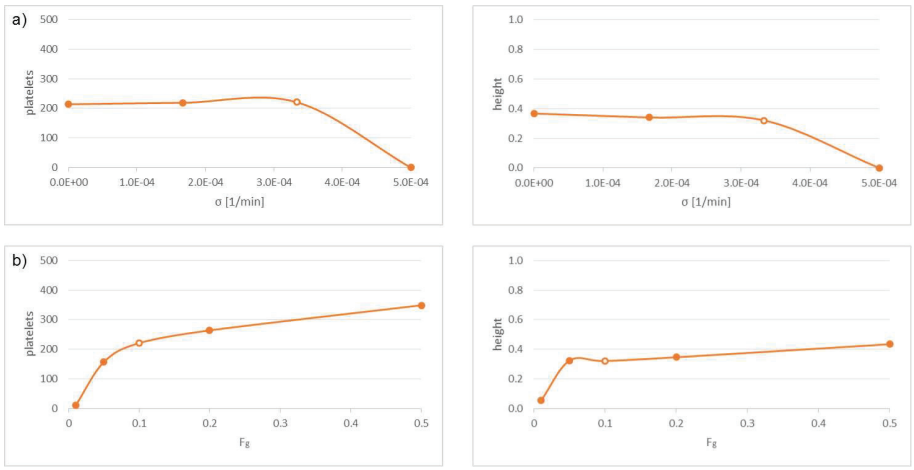

Figure 4.15: Variation of values of PDE parameters (continuation): a) thrombin degradation coefficient σ , b) initial fibrinogen concentration F_g^0. Graphs on the left side show final clot size expressed in number of platelets, while the graphs on the right side show the maximal height of the final clot, normalized by the vessel diameter. Empty points denote the result of the single basic simulation with values of parameters given in Table 4.1 (see Appendix).

4.2.6 Platelet bond strength

A series of simulations was done to investigate the influence of inter-platelet bond strengths on the clot growth. As f_3^A represents a bond between platelets situated in the clot core, covered by the fibrin net, it is considered almost unbreakable. Therefore, it was kept at a large constant value of $10nN(= 1 \cdot 10^{-8}N)$ in all simulations. Strength coefficients of the other two types of bonds, f_1^A and f_2^A, were varied in ranges of 0.3 to 0.6, and 0.8 to 1 nN respectively. For each combination of values of f_1^A and f_2^A the activation period t_c was varied in order to find the minimal and the maximal activation time for which a clot core successfully develops. Taking into account the experimental studies [8, 81], the ratio of a single GPIb bond and a single bond between activated platelets was set to $3 : 8$. This ratio can serve as a point of reference, but it is subject to change because the strength of GPIb bonds depends on the shear rate at the moment of contact [8, 81]. Another reason is that the number of bonds established between two platelets is not known. Some attempts have been made to establish an estimate of the number of bonds [25, 125, 127], however they have not been experimentally confirmed.

	f2 [nN]							
	0.8				1			
	f1 [nN]				f1 [nN]			
tc [s]	0.3	0.4	0.5	0.6	0.3	0.4	0.5	0.6
0.01	52	23	0	20	160	42	31	19
0.1	218	193	40	18	303	278	15	25
0.2	0	203	59	20	0	321	50	19
0.3	0	208	207	19	0	244	114	26
0.4	0	0	132	22	0	0	249	27
0.5	0	0	39	21	0	0	219	24
0.6	0	0	0	19	0	0	223	62
0.7				21			161	48
0.8							13	33

	f2 [nN]							
	0.8				1			
	f1 [nN]				f1 [nN]			
tc [s]	0.3	0.4	0.5	0.6	0.3	0.4	0.5	0.6
0.01	0.118	0.087	0.000	0.057	0.245	0.119	0.075	0.054
0.1	0.319	0.328	0.120	0.054	0.334	0.434	0.147	0.054
0.2	0.000	0.358	0.215	0.055	0.000	0.429	0.180	0.056
0.3	0.000	0.373	0.361	0.056	0.000	0.380	0.373	0.070
0.4	0.000	0.000	0.254	0.054	0.000	0.000	0.403	0.099
0.5	0.000	0.000	0.114	0.054	0.000	0.000	0.340	0.084
0.6	0.000	0.000	0.000	0.054	0.000	0.000	0.436	0.138
0.7				0.056			0.201	0.150
0.8							0.054	0.060

Table 4.2: Detailed results of simulations for variation of values of parameters for inter-platelet bonds f_1^A, f_2^A and activation time t_c parameters.

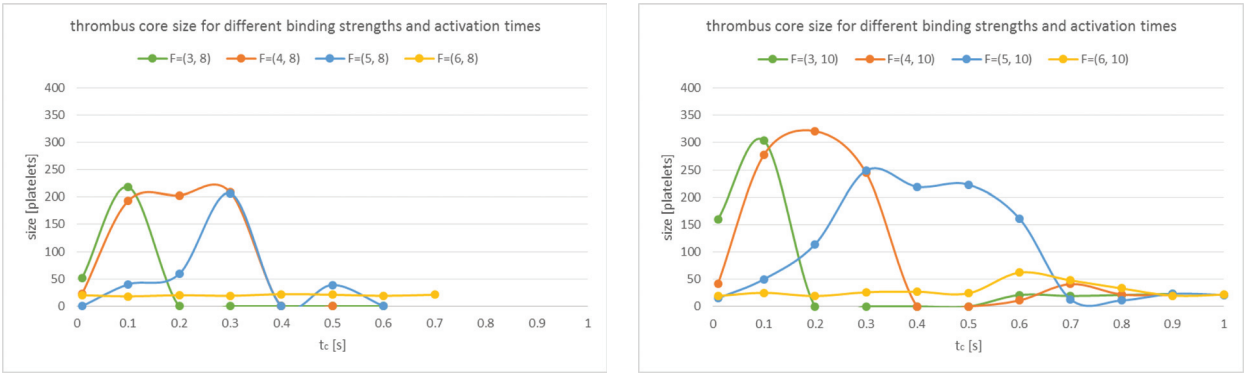

Figure 4.16: Variation of strength of platelet forces. The graph on the left side shows clot core sizes for $f_2^A = 0.8$ nN, while the right one shows results for $f_2^A = 1$ nN. In each case f_1^A was varied for values of 0.3, 0.4, 0.5 and 0.6 nN and the activation time was varied between 0.1 and 1 s.

Two graphs in Figure 4.16 show the clot core sizes for f_2^A of 0.8 and 1 nN respectively. On each of them four curves present the results for f_1^A of 0.3, 0.4, 0.5 and 0.6 nN for different activation times t_c. For each combination of values of parameters f_1^A and f_2^A three types of behaviour were observed. The first type corresponds to the case when the activation period t_c is too low. In this case newly aggregated platelets are activated too quickly and the "activated" part of the clot grows too fast. This results in the breakage of the platelet aggregate before the development of the fibrin net, i.e. clot core. The results show that the minimal activation time for which the clot core forms increases significantly as the value of f_1^A increases. Additionally, the higher value of f_2^A decreases the minimal activation time as it allows the "activated" platelet aggregate to grow larger before breaking.

The second type of behaviour corresponds to the case where the activation time is in the range of values for which a clot core is able to normally develop. The results show that the higher value of f_2^A allows a higher core size maximum for the same f_1^A value. However,

maxima for the different values of f_2^A are not achieved for the same activation times.

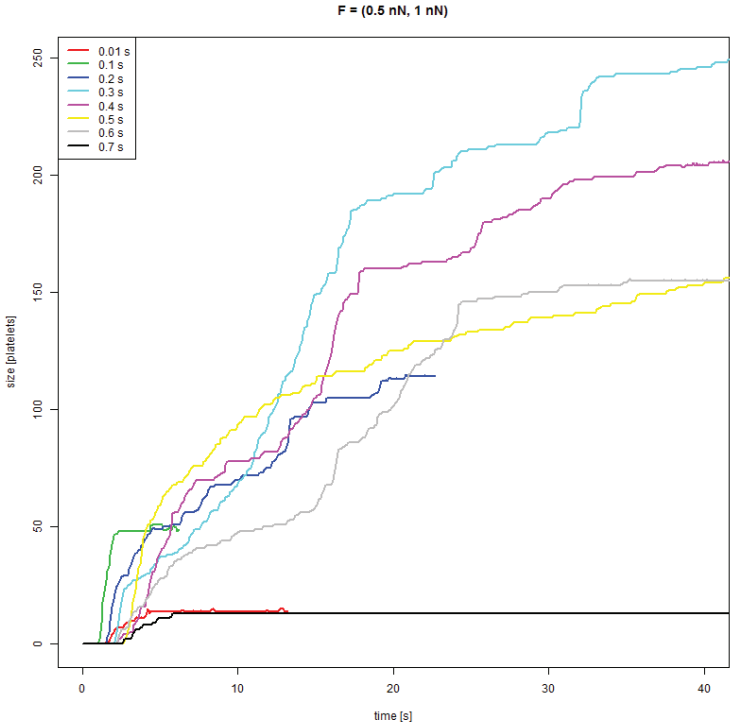

Figure 4.17: Clot core growth in first 40 s for values of f_1^A and f_2^A of 0.5 and 1 nN respectively. Each graph corresponds to a different value of activation time t_c - from 0.01 to 0.7 seconds.

The third type of behaviour occurs when the activation time is too long, which prevents the formation of the clot core. As the activation time is too long, the weakly bound platelet aggregates grow to quickly and they break off before any consisting platelets can activate. Hence no activation occurs, and the clot cannot sustain flow pressure.

Figure 4.17 shows clot core growth in first 40 seconds for $f_1^A = 0.4$ nN, $f_2^A = 1$ nN, and activation times from 0.01 to 0.7 seconds. For values of the activation time 0.01 and 0.7 seconds the clot was unable to develop. In the case of a too rapid activation, as the adhering platelets activate immediately after the adhesion, the platelet aggregate rapidly grows and breaks off while clot core is still too small. In the case of the long activation time, aggregated platelets cannot sustain the increase of the flow shear rate at the surface of the growing clot, and thus do not get activated, leaving again an underdeveloped core. Generally speaking, a shorter activation time will have for an effect a faster growth of the platelet aggregate. The growth rate of the fibrin net is bounded by the growth rate of the platelet aggregate, but also by the values of parameters of the system (4.13). Thus, when the platelet aggregate growth is too rapid the fibrin net growth rate becomes bounded by the underlying regulatory network, and the weaker parts of the clot break-off sooner, leaving the smaller core. This

effect is visible in Figure 4.17 for activation times of 0.1 and 0.2 seconds, while t_c of 0.01 represents a critical case. At the activation time of 0.3 seconds the clot core reaches its maximal value. At longer activation times the clot core growth rate follows more closely the growth rate of the platelet aggregate. As the role of the fibrin clot is also to reinforce the inter-platelet bonds, and thus to support the clot growth, the clot and the core are able to grow to a larger size. However, if the activation time is longer the weakly bound aggregates at the surface need more time to activate and are thus less prone to the increase of the flow shear rate in the narrowing vessel. Hence, the core growth rate decreases as the activation time increases from the value of 0.3 seconds, where the maximum is achieved.

4.2.7 Flow velocity influence

The behaviour of the model was tested in flows of different speeds and in three vessels of different diameters - 25, 50 and 75 μm. In order to have comparable conditions in the near wall region, for all three vessels flow velocities were set to correspond to wall shear rates of 250, 500, 1000, 1500, 2000 and 2500 s^{-1}. In order to avoid that in faster flows the initial level of thrombin concentration at the injury site is immediately taken away by the flow, the level of thrombin at the injury site was kept at value of 1 for the first 5 seconds of the simulation. The Figure 4.18 shows the clot core size and the clot core height for each vessel diameter and each wall shear rate.

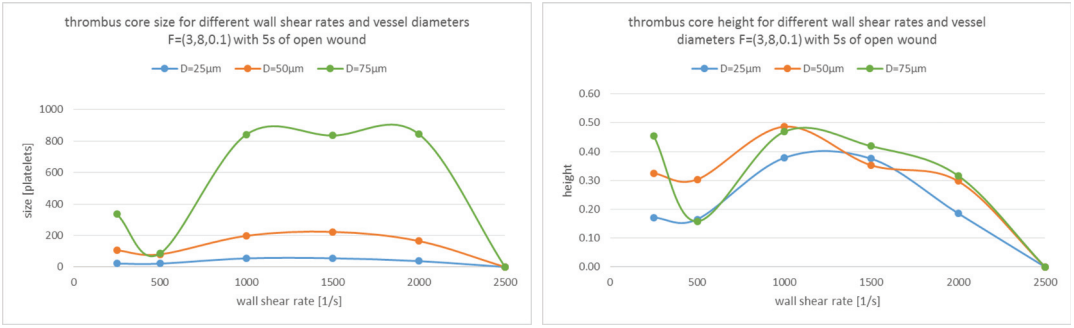

Figure 4.18: Variation of flow shear rate (i.e. flow mean velocity) from 250 to 2500 s^{-1} for vessel diameters of 25 (blue), 50 (red), and 75 μm (green). The graph on the left shows the final clot size expressed in number of platelets, while the graph on the right shows the maximal height of the final clot, normalized by the vessel diameter.

Results of the clot core size show that a larger vessel enables the development of a larger core. For wall shear rates of 1000, 1500 and 2000 s^{-1} the clot and its core were able to fully develop and grow to a larger size. For the chosen values of parameters the shear rate of 2500 s^{-1} was too high for the clot to form – platelet aggregates would break-off too soon and the concentration of thrombin was completely washed away. At the wall shear rate of 500 s^{-1} the clot core was able to develop, however its size was smaller in all three vessels with

different diameters. Finally, for the wall shear rate of 250 s^{-1}, the low flow velocity allowed the counterflow propagation of thrombin, and thus the formation of a fibrin net in the bulk flow, outside of the clot. The results for the clot core height show that in cases when the clot core was able to grow to a larger size, at wall shear rates of 1000, 1500 and 2000 s^{-1}, the core height decreased with the increase of the flow speed. Figure 4.19 shows the final clot stages for different wall shear rates in a vessel of 50 μm in diameter. In Figure 4.20 the final clot stages are shown for the different vessel diameters at the wall shear rate of 1500 s^{-1}.

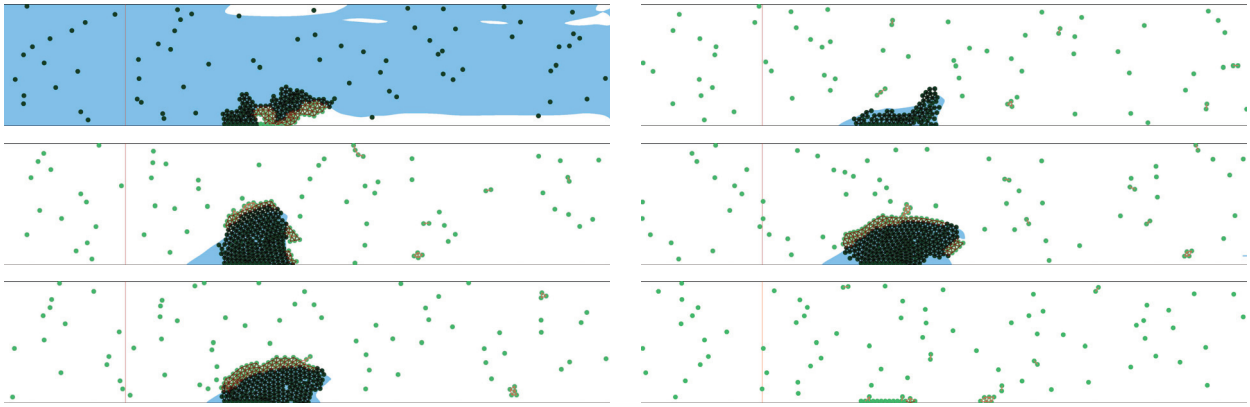

Figure 4.19: Final stages of clot growth in the vessel of 50 μm in diameter for different wall shear rates: a) 250 s^{-1}, b) 500 s^{-1}, c) 1000 s^{-1}, d) 1500 s^{-1}, e) 2000 s^{-1} and f) 2500 s^{-1}.

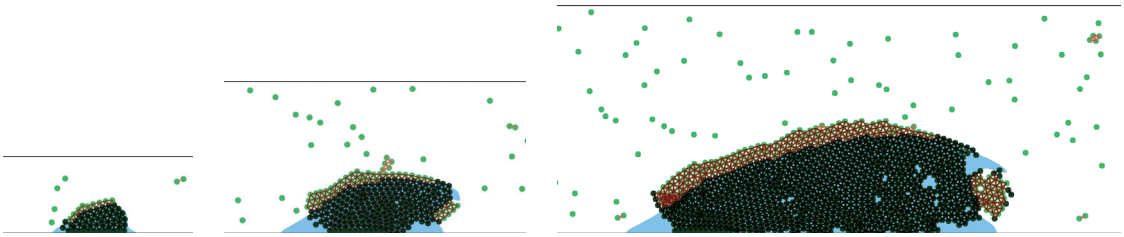

Figure 4.20: Final stages of clot growth for a wall shear rate of 1500 s^{-1} in a vessel of: a) 25, b) 50 and c) 75μm in diameter.

w.s.r.	D = 25µm		D = 50µm		D = 75µm	
[1/s]	plt.	height	plt.	height	plt.	height
250	21	0.171	106	0.325	359	0.602
500	21	0.165	80	0.303	85	0.158
1000	54	0.378	198	0.486	841	0.469
1500	55	0.375	223	0.353	859	0.419
2000	37	0.186	165	0.297	845	0.316
2500	0	0.000	0	0.000	0	0.000

Table 4.3: Detailed results of simulations for variation of wall shear rate in vessels of diameter of 25, 50 and 75 μm.

Chapter 5

Mathematical analysis of a model problem for atherosclerosis

5.1 Introduction

Atherosclerosis is a condition which can take several decades to develop and show first noticeable symptoms. For a long period of time monocytes slowly accumulate in the vessel wall intima, as a response to oxidized Low-Density Lipoprotein (LDL) molecules. This process has a twofold effect. First, the vessel wall slowly thickens as monocytes accumulate in the wall intima, which gradually narrows the lumen of the vessel. This can lead to an immune response and can start a chronic inflammation with auto-amplifying effects. Second, in a case of inflammation, the large amount of accumulated monocytes (i.e. foam cells) results in structural changes of vessel wall, so called remodelling, and development of the atherosclerotic plaque. Therefore, we can consider two aspects of atherosclerosis development: inflammation and vessel remodelling.

The vessel remodelling aspect of atherosclerosis is biologically closely related to blood coagulation. In the process of vessel wall remodelling, muscle cells proliferate and migrate towards the inner surface of the vessel wall. This results in formation of a fibrous cap over the lipid deposit, so called atherosclerotic plaque. The mechanical properties of the plaque significantly differ from the properties of a healthy vessel wall. The surface of the plaque is more rigid and prone to rupture due to flow pressure and reduced surface elasticity. Structural changes together with the narrowed lumen and increased flow pressure, make the vessel wall highly susceptible to rupture, which would initiate blood coagulation on top of the plaque. Formation of blood clot on the already narrowed part of the vessel can lead either to complete occlusion of the vessel or to rupture of the blood clot, both of which usually have tragic consequences. From modelling point of view, hybrid models similar to ones described in Chapter 4 can be used to model the remodelling aspect of atherosclerosis.

Such models would be able to describe the structure of the atherosclerotic plaque and its interaction with blood flow, and would allow the study of plaque rupture.

As it was mentioned in Introduction chapter (Section 1.3.2) previous efforts were made to model the inflammatory aspect of atherosclerosis. The next step in this modelling approach is to develop a 2D model of inflammation, which takes into account the vessel intima thickness and the recruitment of monocytes from blood flow to vessel wall. In the previous model [37, 38], described in Section 1.3.2, equations (1.4)-(1.5), the existence of travelling wave is proven for the monostable case. In this chapter we study the bistable case. In order to prove travelling wave existence, we develop mathematical tools which will, in future works, applied to develop the bistable model of inflammation in atherosclerosis. Thus, we consider a simplified problem, which will have the same mathematical properties as the future model, and for it prove the travelling wave existence in a bistable case. To do so we use Leray-Schauder method, with topological degree and a priori estimates.

5.2 Formulation of the problem

In this work we consider the reaction-diffusion equation

$$\frac{\partial v}{\partial t} = \Delta v + f(v), \tag{5.1}$$

with nonlinear boundary conditions:

$$y = 0 : \frac{\partial v}{\partial y} = 0, \quad y = 1 : \frac{\partial v}{\partial y} = g(v) \tag{5.2}$$

in the infinite strip $\Omega = \{-\infty < x < \infty, 0 < y < 1\}$. Such models arise in various applications including mathematical models of atherosclerosis [38] and other inflammatory diseases. In this case, the variable v corresponds to the concentration of white blood cells in the tissue. The nonlinear boundary condition describes the cell influx through the boundary. This influx depends on cell concentration in the tissue. This self-amplifying mechanism can result in the development of chronic inflammation and spreading of the inflammation in space. In the context of atherosclerosis, domain Ω corresponds to the blood vessel wall (intima) where the disease develops.

We will study the existence of a travelling wave solution of this problem. This is a solution of the form $v(x, y, t) = u(x - ct, y)$. It satisfies the equation

$$\Delta u + c\frac{\partial u}{\partial x} + f(u) = 0 \tag{5.3}$$

with the boundary conditions

$$y = 0 : \frac{\partial u}{\partial y} = 0, \quad y = 1 : \frac{\partial u}{\partial y} = g(u). \tag{5.4}$$

Here c is an unknown constant, the wave speed. Everywhere below we will assume that the functions f and g are continuous together with their third derivatives. In some cases, these conditions can be weakened.

The case where $g(u) \equiv 0$ is well studied in the literature. In particular, it can have a one-dimensional solution, which depends only on the variable x along the axis of the strip. In this case, we obtain the reaction-diffusion equation

$$u'' + cu' + f(u) = 0, \tag{5.5}$$

where prime denotes the derivative with respect to x. Suppose that $f(u_\pm) = 0$ for some u_+ and u_-. Let us recall that the case where $f'(u_\pm) < 0$ is called bistable. If one of these two derivatives is negative and another one is positive, then it is a monostable case. If there exists a solution of equation (5.5) with the limits $u(\pm\infty) = u_\pm$, then it is unique in the bistable case; in the monstable case, there is a continuous family of solutions. The existence of such solutions is determined by the function $f(u)$ (see [122] and the references therein).

In this work we study problem (5.3), (5.4) with a function g different from zero. We will look for solutions with the limits

$$\lim_{x\to\pm\infty} u(x, y) = u_\pm(y), \quad 0 < y < 1, \tag{5.6}$$

where $u_\pm(y)$ are some functions which satisfy the problem in the cross section:

$$u'' + f(u) = 0, \quad 0 < y < 1, \quad u'(0) = 0, \quad u'(1) = g(u(1)). \tag{5.7}$$

As above, we introduce the bistable and the monostable cases. Consider problem (5.7) linearized about solutions $u_\pm(y)$ and the corresponding eigenvalue problems:

$$v'' + f'(u_\pm(y))v = \lambda v, \quad 0 < y < 1, \quad v'(0) = 0, \quad v'(1) = g'(u_\pm(1))v(1). \tag{5.8}$$

If both of them have all eigenvalues in the left-half plane, then we call it the bistable case. If one of these problems has all eigenvalues in the left-half plane and another one has some eigenvalues in the right-half plane, then it is the monostable case.

Investigation of problem (5.3), (5.4) relies on the properties of the corresponding operators. It will be shown that in the bistable case where the essential spectrum of the corresponding linearized operator lies in the left-half plane, the operator satisfies the Fredholm property. Moreover we can introduce a topological degree. These tools allow us to use various methods to prove the existence of solutions. We will use the Leray-Schauder method based on the topological degree and a priori estimates of solutions. It is a continuation of the

previous work [6] where more restrictive conditions on the functions f and g were imposed. It was assumed that they had the same zeros.

Let us note that a reaction-diffusion system of equations with nonlinear boundary conditions suggested as a model of atherosclerosis was studied in [38] in the monostable case. The method of proof is different in this case and it cannot be applied in the bistable case. However we can expect that it is applicable for the scalar equation in the monostable case. The scalar equation with nonlinear boundary condition and with $f(u) \equiv 0$ was considered in [78]. However, behavior of solutions at infinity in [78] was not specified. In this work we study problem (5.3), (5.4) in the bistable case.

5.3 Solutions in the cross-section

5.3.1 General case

In this section we will study the problem

$$\frac{d^2w}{dy^2} + f(w) = 0, \quad w'(0) = 0, \quad w'(L) = g(w(L)) \tag{5.9}$$

in the interval $0 < y < L$. We will suppose here that the functions f and g are continuous together with their first derivatives. We can reduce the second-order equation to the system of two first-order equations

$$w' = p, \quad p' = -f(w),$$

and then to the equation

$$\frac{dp}{dw} = -\frac{f(w)}{p} \ .$$

We can solve this equation analytically. We will consider for simplicity only monotone solutions and denote $w_+ = \max w(y)$, $w_- = \min w(y)$. In the case of decreasing solutions $w_+ = w(0)$, $w_- = w(L)$, and the boundary conditions become

$$p(w_+) = 0, \quad p(w_-) = g(w_-)$$

(Figure 5.1). Under the assumption that

$$\int_w^{w_+} f(u)du \geq 0, \quad w_- \leq w \leq w_+,$$

we obtain

$$p(w) = -\sqrt{2\int_{w}^{w_+} f(u)du}. \tag{5.10}$$

From the second boundary condition

$$g(w_-) = -\sqrt{2\int_{w_-}^{w_+} f(u)du}. \tag{5.11}$$

Thus, for any given w_+ such that $f(w_+) > 0$, we find w_- as a solution of equation (5.11). Further, we solve the differential equation (5.10), where $p(w) = w'$, and obtain

$$L = \int_{w_-}^{w_+} \frac{dv}{\sqrt{2\int_{v}^{w_+} f(u)du}}\,.$$

Hence we found the length of the interval as a function of the maximal value of solution. Depending on the functions f and g, solution can exist, it can be unique or non-unique, or it may not exist. The case of increasing solutions can be studied in a similar way. The spectrum of the problem linearized about the solutions can be completely in the left-half plane or it can be partially in the right-half plane.

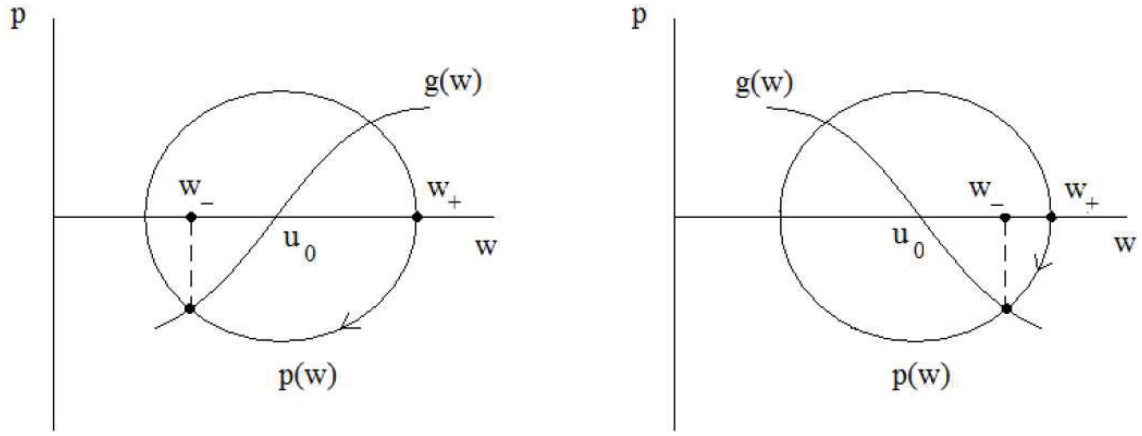

Figure 5.1: Graphical solution of problem (5.7). The function $p(w) = w'(y)$ satisfies the boundary conditions, $p(w_+) = 0, p(w_-) = g(w_-)$. Two examples presented here, with an increasing and a decreasing function g are discussed in the text. Reprinted with permission from [7] – *N. Bessonov et al., Mathematical Modelling of Natural Phenomena, Cambridge University Press, 2013.*

5.3.2 Constant solutions

Existence

In the next section, when we study the wave existence, we will consider problems which depend on parameters. So we will discuss here problem (5.9) where $g = \delta g_0$ and δ is a positive parameter. Suppose that functions $f(y)$ and $g(y)$ are continuous together with their first derivatives and such that

$$f(u_\pm) = g(u_\pm) = 0, \quad f'(u_\pm) < 0, \;\; g'(u_\pm) < 0 \tag{5.12}$$

for some u_+ and u_-, and that these functions have a single zero u_0 in the interval $u_+ < u < u_-$,

$$f(u_0) = g(u_0) = 0, \quad f'(u_0) > 0, \;\; g'(u_0) > 0. \tag{5.13}$$

Lemma 5.1. *Let functions f and g satisfy conditions (5.12), (5.13). Then there exists L_0 such that problem (5.9) with $u_+ < w(0) < u_-$ has only constant solutions for any $L \le L_0$ and any positive δ.*

Proof. The trajectory $p(w)$ corresponding to the solution of this problem is shown schematically in Figure 5.1 (left). If we take $w(0) = w_+$, then $w_- < u_0$, and the value of L is limited from below. It is similar for the symmetric case where $p(w) > 0$.

Let us note that it is different if $g'(u_0) < 0$ (Figure 5.1 (right)). The points w_- converges to w_+ as $\delta \to 0$, and L also converges to 0. □

Stability

Let us discuss stability of constant solutions. We begin with the case where $f(u) \equiv 0$. Then from the first boundary condition in (5.7) we obtain $u = \text{const}$, from the second one, $g(u) = 0$. Denote a zero of the function g by u^*. Let us analyze the eigenvalue problem

$$v'' = \lambda v, \;\; v'(0) = 0, \;\; v'(1) = g'(u^*)v(1). \tag{5.14}$$

Since the principal eigenvalue of this problem is real [123] (in fact, they are all real because the problem is self-adjoint), it is sufficient for what follows to consider real λ. It can be easily verified that $\lambda = 0$ is not an eigenvalue of this problem if $g'(u^*) \neq 0$. Let us find conditions when the eigenvalue λ is positive. Set $\mu = \sqrt{\lambda}$ for a positive λ. Then from the equation and the first boundary condition we obtain

$$v(y) = k(e^{\mu y} + e^{-\mu y}).$$

From the second boundary condition it follows that

$$\mu = g'(u^*)\,\frac{e^{\mu}+e^{-\mu}}{e^{\mu}-e^{-\mu}}\,.$$

This equation has a positive solution for $g'(u^*) > 0$, that is for $u^* = u_0$. In this case there is a positive eigenvalue of problem (5.14). All eigenvalues are negative for $u^* = u_\pm$ since $g'(u_\pm) < 0$.

If $f(u)$ is different from zero, then the corresponding eigenvalue problem, instead of (5.14), writes

$$v'' + f'(u^*)v = \lambda v, \quad v'(0) = 0, \quad v'(1) = g'(u^*)v(1). \tag{5.15}$$

If $f'(u^*) > 0$, then the principal eigenvalue of this problem is greater than the principal eigenvalue of problem (5.14), and it remains positive. This is the case for $u^* = u_0$. If $u^* = u_\pm$, then the eigenvalues are negative.

5.4 Property of the operators

5.4.1 Fredholm property

Consider the operator corresponding to problem (5.3), (5.4) and linearized about a solution $u(x, y)$:

$$Av = \Delta v + c\frac{\partial v}{\partial x} + a(x, y)v, \quad (x, y) \in \Omega, \tag{5.16}$$

$$Bv = \begin{cases} \frac{\partial v}{\partial y} & , \quad y = 0 \\ \frac{\partial v}{\partial y} - b(x)v & , \quad y = 1 \end{cases}, \tag{5.17}$$

where $\Omega = \{-\infty < x < \infty, \;\; 0 < y < 1\}$, and

$$a(x, y) = f'(u(x, y)), \quad b(x) = g'(u(x, 1)).$$

The operator $L = (A, B)$ acts from the space $E = C^{2+\alpha}(\bar{\Omega})$ into the space $F = C^{\alpha}(\bar{\Omega}) \times C^{1+\alpha}(\partial\Omega)$. Consider the limiting operators

$$A^{\pm}v = \Delta v + c\frac{\partial v}{\partial x} + a_{\pm}(y)v, \quad (x, y) \in \Omega, \tag{5.18}$$

$$B^{\pm}v = \begin{cases} \frac{\partial v}{\partial y} & , \quad y = 0 \\ \frac{\partial v}{\partial y} - b_{\pm}v & , \quad y = 1 \end{cases} \tag{5.19}$$

and the corresponding equations

$$A^{\pm}v = 0, \quad B^{\pm}v = 0. \tag{5.20}$$

Here

$$a_{\pm}(y) = \lim_{x \to \pm\infty} a(x, y), \quad b_{\pm} = \lim_{x \to \pm\infty} b(x).$$

Denote by $\tilde{v}(\xi, y)$ the partial Fourier transform of $v(x, y)$ with respect to x. Then from (5.20) we obtain

$$\tilde{v}'' + (-\xi^2 + ci\xi + a_{\pm}(y))\tilde{v} = 0, \quad 0 < y < 1, \tag{5.21}$$

$$\tilde{v}'(\xi, 0) = 0, \quad \tilde{v}'(\xi, 1) = b_{\pm}\tilde{v}(\xi, 1). \tag{5.22}$$

Since we consider the bistable case, then the eigenvalue problem

$$v'' + a_{\pm}(y)v = \lambda v, \quad 0 < y < 1, \quad v'(0) = 0, \quad v'(1) = b_{\pm}v(1) \tag{5.23}$$

has all eigenvalues in the left-half plane. Therefore for each $\xi \in \mathbb{R}$, problem (5.21), (5.22) has only zero solution. Hence $v(x, y) \equiv 0$, and thus we have proved that limiting problems do not have nonzero bounded solutions. This is also true for the formally adjoint operator. Therefore the operator L satisfies the Fredholm property. It remains also true if the operator acts from $W^{2,2}_{\infty}(\Omega)$ into $L^2_{\infty}(\Omega) \times W^{1/2,2}_{\infty}(\partial\Omega)$ ([124], page 163) where the ∞-spaces are defined as follows. Let E be a Banach space with the norm $\|\cdot\|$ and ϕ_i be a partition of unity. Then E_{∞} is the space of functions for which the expression

$$\|u\|_{\infty} = \sup_i \|u\phi_i\|$$

is bounded. This is the norm in this space.

Theorem 5.2. *If both problems (5.23) have all eigenvalues in the left-half plane, then the operator $L = (A, B)$ acting from $C^{2+\alpha}(\bar{\Omega})$ into $F = C^{\alpha}(\bar{\Omega}) \times C^{1+\alpha}(\partial\Omega)$ or from $W^{2,2}_{\infty}(\Omega)$ into $L^2_{\infty}(\Omega) \times W^{1/2,2}_{\infty}(\partial\Omega)$ satisfies the Fredholm property.*

5.4.2 Properness and topological degree

Consider the nonlinear operator in the domain Ω

$$T_0(w) = \Delta w + c\frac{\partial w}{\partial x} + f(w), \quad (x,y) \in \Omega, \tag{5.24}$$

and the boundary operator

$$Q_0(w) = \begin{cases} \frac{\partial w}{\partial y} & , \quad y = 0 \\ \frac{\partial w}{\partial y} - g(w) & , \quad y = 1 \end{cases}. \tag{5.25}$$

Let $w = u+\psi$, where $\psi(x,y)$ is an infinitely differentiable function such that $\psi(x,y) = u_+(y)$ for $x \geq 1$ and $\psi(x,y) = u_-(y)$ for $x \leq -1$. Set

$$T(u) = T_0(u+\psi) = \Delta u + c\frac{\partial u}{\partial x} + f(u+\psi) + \Delta\psi + c\,\frac{\partial \psi}{\partial x}\,, \quad (x,y) \in \Omega, \tag{5.26}$$

$$Q(u) = Q_0(u+\psi) = \begin{cases} \frac{\partial u}{\partial y} & , \quad y = 0 \\ \frac{\partial u}{\partial y} - g(u+\psi) + \frac{\partial \psi}{\partial y} & , \quad y = 1 \end{cases}. \tag{5.27}$$

We consider the operator $P = (T, Q)$ acting in weighted spaces,

$$P = (T,Q) : W^{2,2}_{\infty,\mu}(\Omega) \to L^2_{\infty,\mu}(\Omega) \times W^{1/2,2}_{\infty,\mu}(\partial\Omega).$$

with the weight function $\mu(x) = \sqrt{1+x^2}$. The norm in the weighted space is defined as follows:

$$\|u\|_{\infty,\mu} = \|u\mu\|_\infty.$$

In the bistable case where all eigenvalues of problems (5.8) lie in the left-half plane, the operator P is proper in the weighted spaces and the topological degree can be defined [124].

5.5 A priori estimates

5.5.1 Auxiliary results

We begin with some auxiliary results. Consider the problem

$$\Delta u + c\frac{\partial u}{\partial x} + f(u) = 0, \tag{5.28}$$

$$y = 0 : \frac{\partial u}{\partial y} = 0, \quad y = 1 : \frac{\partial u}{\partial y} = g(u). \tag{5.29}$$

We look for the solutions with the limits

$$\lim_{x\to\pm\infty} u(x, y) = u_{\pm}(y), \quad 0 < y < 1 \tag{5.30}$$

at infinity, $u_-(y) > u_+(y)$. The proofs of the following lemmas are similar to those in [6].

Lemma 5.3. *Let $U_0(x, y)$ be a solution of problem (5.28), (5.29) such that $\frac{\partial U_0}{\partial x} \le 0$ for all $(x, y) \in \bar{\Omega}$. Then the last inequality is strict.*

Lemma 5.4. *Let $u_n(x, y)$ be a sequence of solutions of problem (5.28), (5.29) such that $u_n \to U_0$ in $C^1(\bar{\Omega})$, where $U_0(x, y)$ is a solution monotonically decreasing with respect to x. Then for all n sufficiently large $\frac{\partial u_n}{\partial x} < 0$, $(x, y) \in \bar{\Omega}$.*

We will now determine the sign of the speed of the wave connecting a stable and an unstable solutions. This result will be used below for estimates of solutions.

Lemma 5.5. *Suppose $u_0(y)$ is a solution of problem (5.7) in the cross section of the domain, and $u_+(y) < u_0(y) < u_-(y)$. Assume, next, that the corresponding eigenvalue problem*

$$v'' + f'(u_0)v = \lambda v, \quad v'(0) = 0, \quad v'(1) = g'(u_0(1))v(1) \tag{5.31}$$

has some eigenvalues in the right-half plane. If a monotone with respect to x function $w(x, y)$ satisfies the problem

$$\Delta w + c\frac{\partial w}{\partial x} + f(w) = 0, \tag{5.32}$$

$$y = 0 : \frac{\partial w}{\partial y} = 0, \quad y = 1 : \frac{\partial w}{\partial y} = g(w), \tag{5.33}$$

$$\lim_{x\to-\infty} w(x, y) = u_-(y), \quad \lim_{x\to\infty} w(x, y) = u_0(y), \tag{5.34}$$

then $c > 0$. If

$$\lim_{x\to-\infty} w(x, y) = u_0(y), \quad \lim_{x\to\infty} w(x, y) = u_+(y),$$

instead of (5.34), then $c < 0$.

Lemma 5.6. *If problem (5.28)-(5.30) has a solution* w*, then the value of the speed admits the estimate* $|c| \le M$*, where the constant* M *depends only on* $\max_{u\in[u_+,u_-]} |f'(u)|, |g'(u)|$.

5.5.2 Functionalization of the parameter

Let $w_0(x, y)$ be a solution of problem (5.28)-(5.30). Then the functions

$$w_h(x, y) = w_0(x + h, y), \quad h \in \mathbb{R}$$

are also solutions of this problem. The existence of the family of solutions does not allow one to use directly the topological degree because there is a zero eigenvalue of the linearized problem and a uniform a priori estimate of solutions in the weighted spaces does not occur.

In order to overcome this difficulty, we replace the unknown parameter c, the wave speed, by a functional $c(w_h)$. This approach was suggested in [76] for periodic solutions of ordinary differential systems of equations, and then used for travelling waves in [122]. This functional determines a function of h, $s(h) = c(w_h)$. We will construct this functional in such a way that $s'(h) < 0$ and $s(h) \to \pm\infty$ as $h \to \mp\infty$. Then instead of the family of solutions we obtain a single solution for the value of h for which $c = s(h)$.

Let

$$\rho(w_h) = \int_\Omega (w_0(x + h, y) - u_+(y))r(x)dxdy,$$

where $r(x)$ is an increasing function satisfying the conditions:

$$r(-\infty) = 0, \quad r(+\infty) = 1, \quad \int_{-\infty}^{0} r(x)dx < \infty.$$

Since $w_0(x, y)$ is a decreasing function of x, then $\rho(w_h)$ is a decreasing function of h, and

$$\rho(w_h) \to \begin{cases} 0 & , \quad h \to +\infty \\ +\infty & , \quad h \to -\infty \end{cases}.$$

Hence the function $s(h) = c(w_h) = \ln \rho(w_h)$ possesses the required properties.

5.5.3 Estimates of solutions

We consider next the problem

$$\Delta w + c\frac{\partial w}{\partial x} + f_\tau(w) = 0, \tag{5.35}$$

$$y = 0 : \frac{\partial w}{\partial y} = 0, \quad y = 1 : \frac{\partial w}{\partial y} = g_\tau(w), \tag{5.36}$$

$$w(\pm\infty, y) = u_\pm(y), \tag{5.37}$$

where the functions f and g depend on the parameter $\tau \in [0, 1]$. Everywhere below we will assume that the functions $f_\tau(w), g_\tau(w)$ are bounded and continuous together with their derivatives of the third order with respect to w and of the second order with respect to τ. These conditions allow the construction of the topological degree [124].

The proof of the following lemma is given in the appendix.

Lemma 5.7. *Suppose that solution $w(x, y)$ of problem (5.35)-(5.37) satisfies the estimate $|w| \le M$ with some positive constant M, and*

$$|f_\tau^{(i)}(w)|, \ \ |g_\tau^{(i)}(w)| \le K \ \text{ for } \ |w| \le M, \quad i = 0, 1, 2, 3,$$

where K is a positive constant. Then the Hölder norm $C^{2+\alpha}(\bar\Omega)$, $0 < \alpha < 1$ of the solution is bounded by a constant which depends only on K, M and c.

Denote by w_τ a solution of problem (5.35)-(5.37). We need to obtain a uniform estimate of the solution $u_\tau = w_\tau - \psi$ in the norm of the space $W^{2,2}_{\infty,\mu}(\Omega)$. Here $\psi(x, y)$ is an infinitely differentiable function such that $\psi(x, y) = u_+(y)$ for $x \ge 1$ and $\psi(x, y) = u_-(y)$ for $x \le -1$. Since $u \in C^{2+\alpha}(\bar\Omega)$, then the norm $W^{2,2}_\infty(\Omega)$ of the solution is also uniformly bounded. However, the boundedness of the norm in the weighted space does not follow from this and should be proved. In order to obtain the estimate, it is sufficient to prove that the solution is bounded in the weighted space, that is

$$\sup_{(x,y)\in\Omega} |(w_\tau(x, y) - \psi(x, y))\mu(x)| \le M \tag{5.38}$$

with some constant M independent of τ. If this estimate is satisfied, then the derivatives of the solution up to the order two are also bounded. Indeed, the function $u_\tau = w_\tau - \psi$ satisfies the problem

$$\Delta u + c\frac{\partial u}{\partial x} + f(u + \psi) + \gamma(x, y) = 0,$$

$$y = 0 : \frac{\partial u}{\partial y} = 0, \quad y = 1 : \frac{\partial u}{\partial y} = g(u + \psi),$$

where $\gamma(x, y) = \Delta\psi + c\frac{\partial \psi}{\partial x}$. Then the function $v_\tau = u_\tau \mu$ satisfies the problem

$$\Delta v + (c - 2\mu_1)\frac{\partial v}{\partial x} + (-c\mu_1 + 2\mu_1^2 - \mu_2)v + (f(u + \psi) - f(\psi))\mu + (\gamma + f(\psi))\mu = 0, \quad (5.39)$$

$$y = 0 : \frac{\partial v}{\partial y} = 0, \quad y = 1 : \frac{\partial v}{\partial y} = (g(u + \psi) - g(\psi))\mu + g(\psi)\mu, \quad (5.40)$$

where

$$\mu_1 = \frac{\mu'}{\mu}, \quad \mu_2 = \frac{\mu''}{\mu}$$

are bounded infinitely differentiable functions converging to zero at infinity. Since

$$|(f(u + \psi) - f(\psi))\mu| \le \sup_s |f'(s)||u\mu|, \quad |(g(u + \psi) - g(\psi))\mu| \le \sup_s |g'(s)||u\mu|,$$

then, by virtue of (5.38), the functions

$$\Phi(u, x) = (f(u + \psi) - f(\psi))\mu + (\gamma + f(\psi))\mu, \quad \Psi(u, x) = (g(u + \psi) - g(\psi))\mu + g(\psi)\mu$$

are bounded together with their second derivatives. Therefore solutions of problem (5.39), (5.40) are uniformly bounded in the space $C^{2+\alpha}(\Omega)$. Then the norm $W^{2,2}_\infty(\Omega)$ is also bounded.

It remains to prove estimate (5.38). Consider first of all the behavior of solutions at the vicinity of infinity. By virtue of the Fredholm property, $|w_\tau(x, y) - u_\pm(y)|$ decay exponentially as $x \to \pm\infty$. The decay rate is determined by the principal eigenvalue of the corresponding operators in the cross-section of the cylinder. They can be estimated independently of τ.

Let $\epsilon > 0$ be small enough, $N_-(\tau)$ and $N_+(\tau)$ be such that $|w_\tau(x, y) - u_+(y)| \le \epsilon$ for $x \ge N_+(\tau)$ and $|w_\tau(x, y) - u_-(y)| \le \epsilon$ for $x \le N_-(\tau)$. For a polynomial weight function $\mu(x)$ there exists a constant K independent of $\tau \in [0, 1]$ such that

$$|w_\tau(x, y) - u_\pm(y)|\mu(x) \le K, \quad x \gtrless N_\pm(\tau), \quad \tau \in [0, 1].$$

Since the functions $w_\tau(x, y)$ are uniformly bounded, then (5.38) will follow from the uniform boundedness of the values $N_\pm(\tau)$.

First, let us note that the difference between them is uniformly bounded. Indeed, if this is not the case and $N_+(\tau) - N_-(\tau) \to \infty$ as $\tau \to \tau_0$ for some τ_0, then there are two solutions of problem (5.35), (5.36) for $\tau = \tau_0$, w_1 and w_2 with the limits

$$w_1(x,y) \to \begin{cases} u_-(y) & , \quad x \to -\infty \\ u_0(y) & , \quad x \to +\infty \end{cases}, \quad w_2(x,y) \to \begin{cases} u_0(y) & , \quad x \to -\infty \\ u_+(y) & , \quad x \to +\infty \end{cases}.$$

These solutions are obtained as limits of the solution w_τ as $\tau \to \tau_0$. In order to obtain them, consider a sequence of functions $w_{\tau_k}(x,y)$, $\tau_k \to \tau_0$ and two sequences of shifted functions: $w_{\tau_k}(x + N_-(\tau_k), y)$ and $w_{\tau_k}(x + N_+(\tau_k), y)$. The first sequence gives in the limit the first solution, the second limit gives the second solution.

The existence of such solutions contradicts Lemma 5.5 since the first one affirms that the speed is positive while the second one that it is negative.

Next, if one of the values $|N_\pm(\tau)|$ tends to infinity as $\tau \to \tau_0$, then the modulus $|c(w_h)|$ of the functional introduced in Section 4.1 also tends to infinity as $\tau \to \tau_0$. This contradicts a priori estimates of the wave speed. Thus, we have proved the following theorem.

Theorem 5.8. *Let the functions $f_\tau(w), g_\tau(w)$ be bounded and continuous together with their derivatives of the third order with respect to w and of the second order with respect to τ. If there exists a solution w_τ of problem (5.35)-(5.37) such that $u_\tau = w_\tau - \psi \in W^{2,2}_{\infty,\mu}(\Omega)$, then the norm $\|u_\tau\|_{W^{2,2}_{\infty,\mu}(\Omega)}$ is bounded independently of τ and of the solution w_τ.*

5.6 Leray-Schauder method

5.6.1 Model problem

Consider the problem

$$\Delta w + c\frac{\partial w}{\partial x} + f(w) = 0, \tag{5.1}$$

$$y = 0 : \frac{\partial w}{\partial y} = 0, \quad y = 1 : \frac{\partial w}{\partial y} = 0, \tag{5.2}$$

$$w(\pm\infty, y) = u_\pm, \tag{5.3}$$

where we put 0 instead of $g(w)$ in the boundary condition, u_+ and u_- are some numbers such that $f(u_\pm) = 0$, $f'(u_\pm) < 0$. Suppose that there exists a single zero u_0 of the function

f in the interval (u_+, u_-), $f'(u_0) > 0$. Less restrictive conditions on the function f can also be considered. In this case the problem

$$w'' + cw' + f(w) = 0, \quad w(\pm\infty) = u_\pm$$

has a solution $w_0(x)$ for a unique value of c (see, e.g., [122]). This function is also a solution of problem (5.1)-(5.3). The uniqueness of this solution as a solution of the two-dimensional problem is proved in the following lemma.

Lemma 5.9. *There exists a unique monotone in x solution of problem (5.1)-(5.3) up to translation in space.*

Proof. Suppose that there exist two different monotone solutions of problem (5.1)-(5.3), (w_1, c_1) and (w_2, c_2). We recall that the corresponding values of the speed c can be different. Consider the equation

$$\frac{\partial v}{\partial t} = \Delta v + c_1 \frac{\partial v}{\partial x} + f(v) \tag{5.4}$$

with the boundary condition (5.2). The function $w_1(x, y)$ is a stationary solution of this problem. It is proved in [123] that it is globally stable with respect to all initial conditions $v(x, y, 0)$, which are monotone with respect to x and such that the norm $\|v(x, y, 0) - w_1(x, y)\|_{L^2(\Omega)}$ is bounded.

Consider the initial condition $v(x, y, 0) = w_2(x, y)$. It is monotone and the L^2 norm of the difference $w_2 - w_1$ is bounded since these functions approach exponentially their limits at infinity. According to the stability result, the solution converges to $w_1(x+h, y)$ with some h. On the other hand, the solution writes $u(x, y, t) = w_2(x - (c_2 - c_1)t, y)$, and it cannot converge to w_1. This contradiction proves the lemma. □

We consider next the problem (5.35)-(5.37) and the corresponding operators

$$T_\tau(u) = \Delta(u + \psi) + c(u + \psi)\frac{\partial(u + \psi)}{\partial x} + f_\tau(u + \psi), \quad (x, y) \in \Omega, \tag{5.5}$$

$$Q_\tau(u) = \begin{cases} \frac{\partial u}{\partial y} & , \quad y = 0 \\ \frac{\partial u}{\partial y} - g_\tau(u + \psi) & , \quad y = 1 \end{cases}, \tag{5.6}$$

$$P_\tau = (T_\tau, Q_\tau) : W^{2,2}_{\infty,\mu}(\Omega) \to L^2_{\infty,\mu}(\Omega) \times W^{1/2,2}_{\infty,\mu}(\partial\Omega).$$

Suppose that $g_\tau(u) \equiv 0$ for $\tau = 0$. Then the equation

$$P_\tau(u) = 0 \tag{5.7}$$

has a unique solution $u_0 = w_0 - \psi$ for $\tau = 0$. The index of this solution, that is the topological degree of this operator with respect to a small neighborhood of the solution, equal 1. Indeed, the index equals $(-1)^\nu$, where the ν is the number of positive eigenvalues of the linearized operator [122], [124]. In the case under consideration, the linearized operator has all eigenvalues in the left-half plane [123].

5.6.2 Wave existence

As above, we assume that the functions $f_\tau(w), g_\tau(w)$ are bounded and continuous together with their derivatives of the third order with respect to w and of the second order with respect to τ. We begin with a general result on wave existence.

Theorem 5.10. *Let the problem*

$$\frac{d^2w}{dy^2} + f_\tau(w) = 0, \quad w'(0) = 0, \;\; w'(L) = g_\tau(w(L)) \tag{5.8}$$

have solutions $u^\tau_\pm(y)$ such that

$$u^\tau_+(y) < u^\tau_-(y), \quad 0 \le y \le L$$

and the eigenvalue problems

$$\frac{d^2v}{dy^2} + f'_\tau(u^\tau_\pm)v = \lambda v, \quad v'(0) = 0, \;\; v'(L) = g'_\tau(u^\tau_\pm)v(L) \tag{5.9}$$

have all eigenvalues in the left-half plane for any $\tau \in [0,1]$. Suppose that for any other solution $u^\tau_0(y)$ of problem (5.8), the eigenvalue problem

$$\frac{d^2v}{dy^2} + f'_\tau(u^\tau_0)v = \lambda v, \quad v'(0) = 0, \;\; v'(L) = g'_\tau(u^\tau_0)v(L) \tag{5.10}$$

has some eigenvalues in the right-half plane. If the problem

$$\Delta w + c\frac{\partial w}{\partial x} + f_\tau(w) = 0, \tag{5.11}$$

$$y = 0 : \frac{\partial w}{\partial y} = 0, \quad y = L : \frac{\partial w}{\partial y} = g_\tau(w), \tag{5.12}$$

$$\lim_{x\to\pm\infty} w(x,y) = u_{\pm}^{\tau}(y), \quad 0 < y < L, \tag{5.13}$$

considered in the domain $\Omega = \{-\infty < x < \infty,\ \ 0 < y < L\}$*, has a unique solution monotone with respect to* x *for* $\tau = 0$*, then it also has a unique monotone solution for any* $\tau \in [0,1]$*.*

Proof. The proof of the theorem is based on the Leray-Schauder method. We consider equation (5.7). The topological degree for the operator $P_\tau(u)$ is defined (Section 3).

Denote by Γ_m the ensemble of solutions of equation (5.7) for all $\tau \in [0,1]$ such that for any $u \in \Gamma_m$ the function $w = u + \psi$ is monotone with respect to x. Let Γ_n be the set of all solutions for which the function $w = u + \psi$ is not monotone with respect to x. Then the distance d between these two sets in the space $E = W^{2,2}_{\infty,\mu}(\Omega)$ is positive. Indeed, suppose that this is not true. Then there exist two sequences $u_k \in \Gamma_m$ and $v_k \in \Gamma_n$ such that $\|u_k - v_k\|_E \to 0$ as $k \to \infty$. From Lemma 5.4 it follows that the functions $w_k = v_k + \psi$ are monotone with respect to x for k sufficiently large. This contradiction shows that the convergence cannot occur.

From Theorem 5.8, applicable for solutions from Γ_m, it follows that the set Γ_m is bounded in E. Moreover, by virtue of properness of the operator P_τ it is compact. Hence there exists a bounded domain $G \subset E$ such that $\Gamma_m \subset G$ and $\Gamma_n \cap \bar{G} = \oslash$.

Consider the topological degree $\gamma(P_\tau, G)$. Since

$$P_\tau(u) \neq 0, \quad u \in \partial G,$$

then it is well defined. Since $\gamma(P_0, G) = 1$ (Section 6.1), then $\gamma(P_\tau, G) = 1$ for any $\tau \in [0,1]$. Hence problem (5.11)-(5.13) has a monotone solution for any $\tau \in [0,1]$.

It remains to verify its uniqueness. We recall that

$$\gamma(P_\tau, G) = \sum_i \text{ ind } u_i,$$

where ind u_i is the index of a solution u_i and the sum is taken with respect to all solutions $u_i \in G$. Since $\gamma(P_\tau, G) = 1$ and ind $u_i = 1$ (cf. Section 5.1), then the solution is necessarily unique. □

The previous theorem uses some assumptions about the solutions $u_{\pm}^{\tau}$ and u_0^{τ} of problem (5.8) in the cross-section. We will now consider some particular cases where these conditions can be verified.

Theorem 5.11. *Let* u_+ *and* u_- *be some constants and the following conditions be satisfied:*

1. $f(u_\pm) = 0,\ f'(u_\pm) < 0\ \ ,\ \ g(u_\pm) = 0,\ g'(u_\pm) < 0\ ,$

2. $f(u_0) = 0,\ f'(u_0) > 0\ ,\ \ g(u_0) = 0,\ g'(u_0) > 0$ *for some* $u_0 \in (u_+, u_-)$*, and there are no other zeros of these functions in this interval.*

Then for all positive L *sufficiently small, the problem*

$$\Delta w + c\frac{\partial w}{\partial x} + f(w) = 0, \tag{5.14}$$

$$y = 0 : \frac{\partial w}{\partial y} = 0, \quad y = L : \frac{\partial w}{\partial y} = g(w), \tag{5.15}$$

$$\lim_{x\to\pm\infty} w(x, y) = u_\pm \tag{5.16}$$

considered in the domain $\Omega = \{-\infty < x < \infty,\ \ 0 < y < L\}$ *has a unique solution monotone with respect to* x*.*

This theorem follows from the previous one, where we set $g_\tau = \tau g$, and from Lemmas 5.4 and 5.9

Theorem 5.12. *Let the function* $g(w)$ *satisfy conditions of the previous theorem. Then for all positive* L*, the problem*

$$\Delta w + c\frac{\partial w}{\partial x} = 0, \tag{5.17}$$

$$y = 0 : \frac{\partial w}{\partial y} = 0, \quad y = L : \frac{\partial w}{\partial y} = g(w), \tag{5.18}$$

$$\lim_{x\to\pm\infty} w(x, y) = u_\pm \tag{5.19}$$

considered in the domain $\Omega = \{-\infty < x < \infty,\ \ 0 < y < L\}$ *has a unique solution monotone with respect to* x*.*

Proof. The proof consists of two steps. First, we consider sufficiently small L and use the result of the previous theorem as a starting point for the deformation $f_\tau = (1 - \tau)f$. For $\tau = 1$ we obtain $f_\tau(w) \equiv 0$. At the next step, we increase the width L of the domain. It is equivalent to the change of variables $y = \sigma\eta$ in the equation and in the boundary condition. The problem in the cross-section has only constant solutions. We can use the results of Section 2.2 about their stability and Theorem 5.10. □

In the last theorem we consider the case of small boundary conditions where the solution is close to a one-dimensional solution.

Theorem 5.13. *Suppose that* $f(u_\pm) = 0,\ f'(u_\pm) < 0$ *and for some* c_0 *there exists a monotone solution* $w(x)$ *of the problem*

$$w'' + c_0 w' + f(w) = 0, \quad w(\pm\infty) = u_\pm.$$

Then for all ϵ *sufficiently small, the problem*

$$\Delta w + c\frac{\partial w}{\partial x} + f(w) = 0, \tag{5.20}$$

$$y = 0 : \frac{\partial w}{\partial y} = 0, \quad y = L : \frac{\partial w}{\partial y} = \epsilon g(w), \tag{5.21}$$

$$\lim_{x\to\pm\infty} w(x,y) = u_\pm^\epsilon(y) \tag{5.22}$$

considered in the domain $\Omega = \{-\infty < x < \infty,\ 0 < y < L\}$ *has a unique solution monotone with respect to* x. *Here* $u_\pm^\epsilon(y)$ *are solutions of the problem*

$$\frac{\partial w}{\partial y} + f(w) = 0, \quad w'(0) = 0,\ w'(L) = \epsilon g(w(L)),$$

$u_\pm^\epsilon(y) \to u_\pm$ *as* $\epsilon \to 0$ *uniformly in* y.

The proof of this theorem follows from the property of topological degree: a solution with nonzero index persists under small deformation of the operator.

Conclusion and Perspectives

Conclusions. This thesis is devoted to discrete and continuous modelling of blood flows and related phenomena such as blood coagulation and atherosclerosis. The main results of the dissertation are as follows:

1. Modelling of blood flow with a discrete particle method was carried out. Blood plasma flow was modelled by Dissipative Particle Dynamics (DPD) in 2D. Various implementations of blood flow model and boundary conditions in DPD were introduced and investigated in order to obtain a correct description of the fluid flow appropriate for the investigation of blood coagulation. A complex combination of simulation domain partition and boundary conditions was developed that is suitable for modelling of blood coagulation. Furthermore, a model of the erythrocyte membrane suitable for use in the DPD method was proposed and investigated.

2. A discrete model of platelet aggregation in flow was proposed. The DPD method was used to model blood plasma flow and platelets suspended in it. Platelet clot growth in flow was studied, depending on inter-platelet adhesion forces. Finally, a possible mechanism of platelet clot growth arrest in flow was suggested.

3. Two hybrid models of platelet and fibrin clot were proposed and investigated. They combine discrete (DPD) and continuous (PDE) methods, describing platelets suspended in plasma and concentrations of blood factors in flow respectfully. The first hybrid model was used to study the interaction between a platelet clot and a fibrin concentration in flow. The second hybrid model introduced a more realistic sub-model of coagulation pathways, accounting for its main characteristics. The model was used to study the interaction of platelet and fibrin clot, showing a possible mechanism by which the platelet clot stops growing and limits the further growth of the fibrin net. Furthermore, the influence of the flow speed on the clot formation was investigated in the scope of this model.

4. A mathematical analysis of a model of chronic inflammation related to atherosclerosis was carried out. A problem describing the propagation of a reaction-diffusion wave in the 2D case with nonlinear boundary conditions was studied. The existence of waves in the bistable case was proven using the Leray-Schauder method and a priori estimates of solutions.

5. Numerical implementations of the discrete and hybrid models describing blood flow and blood coagulation were done in the framework of this thesis. Due to the significant computational cost of such models, different optimisation techniques were used. The numerical code was parallelized on both Central Processing Unit (CPU) and Graphical Processing Unit (GPU), and the performances were compared.

Perspectives. The models developed in the thesis concern blood flows and cell interactions with the focus on blood coagulation. They offer many possibilities for future research and development:

- Studies of the properties of blood cells and their interactions in flow, such as the blood cell distribution in flow [15, 16].
- Further advances in the modelling of blood coagulation with a more complete model suitable for medical applications:
  - modelling of blood coagulation in 3D and quantitative comparison with experimental results,
  - investigation of the influence of erythrocyte distribution on clot growth in flow,
  - introduction of a more complete model of blood coagulation pathways and a consequent study of the sensitivity of the model and its impact on clot formation in flow,
  - modelling of the initiation of the coagulation process in flow, as an important first step in the blood coagulation process,
  - modelling of primary fibrinolysis, the process of blood clot decomposition in normal conditions, and secondary fibrinolysis due to a medical disorder, medical treatment, or other cause,
  - modelling of pathological clot growth related to many diseases and disorders, such as atherosclerosis or arthritis.
  - investigation of pulsatile flow influence on clot growth in flow.
- Modelling of atherosclerosis and atherosclerotic plaque development by the same approach (DPD-PDE hybrid method).

We intend to study these questions in the future works.

Publications

The results of the thesis are presented in the following publications:

1. A. Tosenberger, F. Ataullakhanov, N. Bessonov, M. Panteleev, A. Tokarev, V. Volpert, *Modelling of clot growth in flow with a DPD-PDE method*, Journal of Theoretical Biology 337, (2013), pp. 30-41.
2. V. Volpert, N. Bessonov, N. Eymard, A. Tosenberger, *Modèle multi-échelle de la dynamique cellulaire*, Le vivant discret et continu, Editions Matériologiques (Ed.), (2013), ISBN : 978-2-919694-23-5.
3. N. Bessonov, E. Babushkina, S.F. Golovashchenko, A. Tosenberger, F. Ataullakhanov, M. Panteleev, A. Tokarev, V. Volpert, *Numerical Modelling of Cell Distribution in Blood Flow*, Math. Model. Nat. Phenom., 2014, in press.
4. N. Apreutesei, A. Tosenberger, V. Volpert, *Existence of Reaction-Diffusion Waves with Nonlinear Boundary Conditions*, Math. Model. Nat. Phenom. 8(3), (2013), pp. 2-17.
5. N. Bessonov, E. Babushkina, S.F. Golovashchenko, A. Tosenberger, F. Ataullakhanov, M. Panteleev, A. Tokarev, V. Volpert, *Numerical Simulations of Blood Flows With Non-uniform Distribution of Erythrocytes and Platelets*, Russian J. Numer. Anal. Math. Modelling 28(5), (2013), pp. 443-458.
6. A. Tosenberger, F. Ataullakhanov, N. Bessonov, M. Panteleev, A. Tokarev, V. Volpert, *Modelling of clot growth and growth stop in flow by the method of dissipative particle dynamics*, Russian J. Numer. Anal. Math. Modelling 27(5), (2012), pp. 507-522.
7. P. Kurbatova, N. Eymard, A. Tosenberger, V. Volpert, N. Bessonov, *Application of Hybrid Discrete-Continuous Models in Cell Population Dynamics*, (English summary) BIOMAT 2011, 1-10, World Sci. Publ., Hackensack, NJ, (2012).
8. V. Volpert, N. Bessonov, N. Eymard, A. Tosenberger, *Modélisation multi-échelle en dynamique cellulaire*, Proceedings of Ecole de Printemps 2012 de la Société Francophone de Biologie Théorique, Saint-Flour, France, (2012).
9. A. Tosenberger, V. Salnikov, N. Bessonov, E. Babushkina, V. Volpert, *Particle Dynamics Methods of Blood Flow Simulations*, Math. Model. Nat. Phenom. 6(5), (2011), pp. 320-332.

Bibliography

[1] A.G. Alenitsyn, A.S. Kondratyev, I. Mikhailova, I. Siddique, *Mathematical Modeling of clot Growth in Microvessels*, Journal of Prime Research in Mathematics 4,(2008), pp. 195-205.

[2] M.P. Allen, D.J. Tidesley, *Computer Simulation of Liquids*, Clarendon, Oxford, (1987).

[3] T. AlMomani, H.S. Udaykumar, J.S. Marshall, K.B. Chandran, *Micro-scale dynamic simulation of erythrocyte-platelet interaction in blood flow*, Annals of Biomedical Engineering 36(6), (2008), pp. 905-920.

[4] M. Anand, K. Rajagopal, K.R. Rajagopal, *A Model for the Formation, Growth, and Lysis of Clots in Quiescent Plasma. A Comparison Between the Effects of Antithrombin III Deficiency and Protein C Deficiency*, J Theor Biol. 253(4), (2008), pp. 725-738.

[5] M. Anand, K. Rajagopal, K.R. Rajagopal, *A Model for the Formation and Lysis of Blood Clots*, Pathophysiol Haemost Thromb 34(2-3), (2005), pp. 109-120.

[6] N. Apreutesei, V. Volpert, *Reaction-diffusion waves with nonlinear boundary conditions*, Networks and Heterogeneous Media, (2013), in press.

[7] N. Apreutesei, A. Tosenberger, V. Volpert, *Existence of Reaction-Diffusion Waves with Nonlinear Boundary Conditions*, Mathematical Modelling of Natural Phenomena 8(3), (2013), pp. 2-17.

[8] M. Arya, A.B. Kolomeisky, G.M. Romo, M.A. Cruz, J.A. López, B. Anvari, *Dynamic force spectroscopy of glycoprotein Ib-IX and von Willebrand factor*, Biophys J. 88(6), (2005), pp. 4391-4401.

[9] F.I. Ataullakhanov, M.A. Panteleev, *Mathematical modeling and computer simulation in blood coagulation* Pathophysiol Haemost Thromb 34, (2005), pp. 60-70.

[10] M. V. Autieri, *Pro- and Anti-Inflammatory Cytokine Networks in Atherosclerosis* ISRN Vascular Medicine Volume 2012, (2012), 17 pages, doi:10.5402/2012/987629.

[11] J.A. Backer, C.P. Lowe, H.C.J. Hoefsloot, P.D. Iedema, *Poiseuille Flow to Measure the Viscosity of Particle Model Fluids*, J Chem Phys. 122(15), (2005), doi:10.1063/1.1883163.

[12] P. Bagchi, *Mesoscale simulation of blood flow in small vessels*, Biophysical Journal 92(6), (2007), pp. 1858-1877.

[13] I.A. Barynin, I.A. Starkov, M.A. Khanin, *Mathematical Models in Hemostasis Physiology*, Izv Akad Nauk Ser Biol. 1, (1999), pp. 59-66 (in Russian).

[14] Begent N., Born G. V., *Growth rate in vivo of platelet thrombi, produced by iontophoresis of ADP, as a function of mean blood flow velocity*, Nature 227(5261), (1970), pp. 926-930.

[15] N. Bessonov, E. Babushkina, S.F. Golovashchenko, A. Tosenberger, F. Ataullakhanov, M. Panteleev, A. Tokarev, V. Volpert, *Numerical Simulations of Blood Flows With Non-uniform Distribution of Erythrocytes and Platelets*, Russian Journal of Numerical Analysis and Mathematical Modelling 28(5), (2013), pp. 443-458.

[16] N. Bessonov, E. Babushkina, S.F. Golovashchenko, A. Tosenberger, F. Ataullakhanov, M. Panteleev, A. Tokarev, V. Volpert, *Numerical Modelling of Cell Distribution in Blood Flow*, Mathematical Modelling of Natural Phenomena, in print

[17] T. Bodnar, A. Sequeira, *Numerical Simulation of the Coagulation Dynamics of Blood*, Computational and Mathematical Methods in Medicine 9(2), (2008), pp. 83-104.

[18] K. Boryczko, D.A. Yuen, W. Dzwinel, *Finely Dispersed Particles, Micro-, Nano-, and Atto-Engineering*, CRC Press, (2005).

[19] A.E.X. Brown, R.I. Litvinov, D.E. Discher, P.K. Purohit, J.W. Weisel, *Multiscale Mechanics of Fibrin Polymer: Gel Stretching with Protein Unfolding and Loss of Water*, Science 325(5941), (2009), pp. 741-744.

[20] J.R. Jr Buchanan, C. Kleinstreuer, *Simulation of particle-hemodynamics in a partially occluded artery segment with implications to the initiation of microemboli and secondary stenoses*, J Biomech Eng. 120(4), (1998), pp. 446-454.

[21] C. Bui, V. Lleras, O. Pantz, *Dynamics of red blood cells in 2d*, ESAIM: Proc. 28, (2009), pp. 182-194.

[22] J.-P. Cazenave, P. Ohlmann, D. Cassel, A. Eckly, B. Hechler, C. Gachet, *Washed Platelet Suspensions From Human and Rodent Blood*, Platelets and Megakaryocytes, Methods In Molecular Biology 272, (2004), pp 13-28.

[23] Centers for Disease Control and Prevention (CDC), *State-specific Mortality from Sudden Cardiac Death - United States, 1999.*, MMWR Morb Mortal Wkly Rep. 51(6), (2002), pp. 123-126.

[24] S. Chen, G.D. Doolen, *Lattice Boltzmann Method for Fluid Flows*, Annual Review of Fluid Mechanics 30, (1998), pp. 329-364.

[25] L.A. Coburn, *Studies of Platelet GPIb-alpha and von Willebrand Factor Bond Formation Under Flow*, PhD thesis at Georgia Institute of Technology and Emory University, (May 2010).

[26] Colman R. W., Clowes A. W., Goldhaber S. Z., Marder V. J., George J. N., *Hemostasis and ThrombosisBasic Principles and Clinical Practice*, Lippincott Williams & Wilkins, (2006).

[27] Covic L., Singh C., Smith H., Kuliopulos A., *Role of the PAR4 thrombin receptor in stabilizing platelet-platelet aggregates as revealed by a patient with Hermansky-Pudlak syndrome*, Thromb. Haemost. 87(4), (2002), pp. 722-727.

[28] L. Crowl, A.L. Fogelson, *Analysis of Mechanisms for Platelet Near-wall Excess Under Arterial Blood Flow Conditions*, Journal of Fluid Mechanics 676, (2011), pp. 348-375.

[29] L.M. Crowl, A.L. Fogelson, *Computational model of whole blood exhibiting lateral platelet motion induced by red blood cells*, Int j numer method biomed eng. 26(3-4), (2010), pp. 471-487.

[30] Dale G. L., Friese P., Batar P., Hamilton S. F., Reed G. L., Jackson K. W., Clemetson K. J., Alberio L., *Stimulated platelets use serotonin to enhance their retention of procoagulant proteins on the cell surface*, Nature. 415(6868), (2002), pp. 175-179.

[31] B. Das, P.C. Johnson, A.S. Popel, *Effect of nonaxisymmetric hematocrit distribution on non-Newtonian blood flow in small tubes*, Biorheology. 35(1), (1998), pp. 69-87.

[32] M.J. Davies, *The pathophysiology of acute coronary syndromes*, Heart 83, (2000), pp. 361-366.

[33] M.M. Dupin, I. Halliday, C.M. Care, L. Alboul, L.L. Munn, *Modeling the flow of dense suspensions of deformable particles in three dimensions*, Physical Review E 75 (066707), (2007).

[34] W. Dzwinel, K. Boryczko, D.A. Yuen, *Modeling Mesoscopic Fluids with Discrete-Particles. Methods, Algorithms and Results*, Heteroaggregate Finely Dispersed Systems of Biological Interest, A.M. Spasic and J.P. Hsu eds., Taylor & Francis, CRC Press, (2006), pp. 715-778.

[35] N. El Khatib, S. Gnieys, V. Volpert *Atherosclerosis Initiation Modeled as an Inflammatory Process*, Math. Model. Nat. Phenom. 2(2), (2007), pp. 126-141.

[36] N. El Khatib, S. Gnieys, B. Kazmierczak, V. Volpert *Mathematical Modelling of Atherosclerosis as an Inflammatory Disease*, Phil. Trans. R. Soc. A 367(1908), (2009), pp. 4877-4886.

[37] N. El Khatib, *Modelisation Mathematique de l'Atherosclerose*, PhD thesis at Université Claude Bernard - Lyon 1, (2009).

[38] N. El Khatib, S. Gnieys, B. Kazmierczak, V. Volpert , *Reaction-Diffusion Model of Atherosclerosis Development*, Journal of Mathematical Biology, Springer, (2011).

[39] P. Español, M. Revenga, *Smoothed Dissipative Particle Dynamics*, Phys. Rev. E, 67(026705), (2003).

[40] P. Español, *Dissipative Particle Dynamics revisited*, In Dónal Mac Kernan, editor, Challenges in Molecular Simulations, SIMU Newsletter 4, chapter III. Centre Européen de Calcul Atomique et Moléculaire, (2002).

[41] P. Español, *Statistical Mechanics of Coarse-Graining*, in Mikko Karttunen, Ilpo Vattulainen, and Ari Lukkarinen, editors, Lecture notes of SoftSimu2002 - Novel Methods in Soft Matter Simulations, Lecture Notes in Physics. Springer, (2003).

[42] P. Español, P. Warren *Statistical Mechanics of Dissipative Particle Dynamics*, Europhys. Lett. 30 (4), (1995), pp. 191-196.

[43] S. Falati, P. Gross, G. Merrill-Skoloff, B.C. Furie, B. Furie, *Real-time in Vivo Imaging of Platelets, Tissue Factor and Fibrin During Arterial clot Formation in the Mouse*, Nat Med 8, (2002), pp. 1175-1180.

[44] D.A. Fedosov, *Multiscale Modeling of Blood Flow and Soft Matter*, PhD dissertation at Brown University, (2010).

[45] D.A. Fedosov, I.V. Pivkin, G.E. Karniadakis, *Velocity Limit in DPD Simulations of Wall-bounded Flows*, J. Comp. Phys. 227, (2008), pp. 2540-2559.

[46] D. Fedosov, B. Caswell, G.E. Karniadakis, *General coarse-grained red blood cell models: I. Mechanics*, (2009), arXiv:0905.0042 [q-bio.CB].

[47] D. Fedosov, B. Caswell, G.E. Karniadakis, *A Multiscale Red Blood Cell Model with Accurate Mechanics, Rheology, and Dynamics*, Biophysical Journal 98, (2010), pp. 2215-2225.

[48] D.A. Fedosov, H. Lei, B. Caswell, S. Suresh, G.E. Karniadakis, *Multiscale Modeling of Red Blood Cell Mechanics and Blood Flow in Malaria*, PLoS Computational Biology 7(12), (2011), doi: 10.1371/journal.pcbi.1002270.

[49] N. Filipovic, M. Kojic, A. Tsuda, *Modelling Thrombosis Using Dissipative Particle Dynamics Method*, Phil. Trans. R. Soc. A 366(1879), (2008), pp. 3265-3279.

[50] A.L. Fogelson, R.D. Guy, *Immersed-Boundary-Type Models of Intravascular Platelet Aggregation*, Comput. Methods Appl. Mech. Eng. 197, (2008), pp. 2087-2104.

[51] A.L. Fogelson, *Cell-based Models of Blood Clotting*, Single-Cell-Based Models in Biology and Medicine (ed. by A.R.A. Anderson, M.A.J. Chaplain, K.A. Rejniak), Mathematics and Biosciences in Interaction, Birkhäuser Verlag Basel, (2007), pp. 243-269.

[52] A.L. Fogelson, *Plateletwall interactions in continuum models of platelet thrombosis: formulation and numerical solution*, Mathematical Medicine and Biology 21,(2004), pp. 293-334.

[53] M.M. Frojmovic, R.F. Mooney, T. Wong, *Dynamics of Platelet Glycoprotein IIb-IIIa Receptor Expression and Fibrinogen Binding. I. Quantal Activation of Platelet Subpopulations Varies With Adenosine Diphosphate Concentration*, Biophys J. 67(5), (1994), pp. 2060-2068.

[54] J.-L. Gennisson, S. Lerouge, G. Cloutier, *Assessment by Transient Elastography of the Viscoelastic Properties of Blood During Clotting*, Ultrasound in Med. & Biol. 32(10), (2006), pp. 1529-1537.

[55] R.A. Gingold, J.J. Monaghan, *Smoothed particle hydrodynamics: theory and application to non-spherical stars*, Mon. Not. R. Astron. Soc. 181, (1977), pp. 375-389.

[56] R.D. Groot, P.B. Warren, *Dissipative Particle Dynamics: Bridging the Gap Between Atomistic and Mesoscopic Simulation*, J. Chem. Phys. 107(11), (1997), pp. 4423-4435.

[57] R.D. Groot, *Applications of Dissipative Particle Dynamics*, Novel Methods in Soft Matter Simulations, Lecture Notes in Physics 640, ed: M. Karttunen, A. Lukkarinen, I. Vattulainenpp, (2004), pp. 5-38.

[58] R.D. Guy, A.L. Fogelson, J.P.Keener, *Fibrin Gel Formation in a Shear Flow*, Math Med Biol. 24(1), (2007), pp. 111-130.

[59] A.C. Guyton, J.E. Hall, *Textbook of Medical Physiology (Ninth Edition)*, W.B. Saunders, Philadelphia, (1996).

[60] J.M. Haile, *Molecular Dynamics Simulation: Elementary Methods*, Wiley Professional, (2001), ISBN: 978-0-471-18439-3.

[61] P.J. Hoogerbrugge, J.M.V.A. Koelman, *Simulating Microscopic Hydrodynamic Phenomena with Dissipative Particle Dynamics*, Europhys. Lett. 19(2), (1992), pp. 155-160.

[62] S.M. Hosseini, J.J. Feng, *A particle-based model for the transport of erythrocytes in capillaries*, Chem. Eng. Sci. 64, (2009), pp. 4488-4497.

[63] Y. Imai, H. Kondo, T. Ishikawa, C.T. Lim, T. Yamaguchi, *Modeling of hemodynamics arising from malaria infection*, Journal of Biomechanics 43, (2010), pp. 1386-1393.

[64] S.P. Jackson, W.S. Nesbitt, E. Westein, *Dynamics of Platelet clot Formation*, J Thromb Haemost 7 Suppl 1, (2009), pp. 17-20.

[65] S.P. Jackson, *The Growing Complexity of Platelet Aggregation*, Blood 109(12), (2007), pp. 5087-5095.

[66] C.J. Jen, S.J. Hu, H.J. Wu, T.S. Lin, C.W. Mao, *Platelet-Fibrin Interaction in the Suspension and Under Flow Conditions*, Adv Exp Med Biol. 281, (1990), pp. 277-285.

[67] C.J. Jen, J.S. Lin, *Direct Observation of Platelet Adhesion to Fibrinogen- and Fibrin-coated Surfaces*, Am J Physiol. 261(5 Pt 2), (1991), pp. 1457-1463.

[68] C.J. Jen, Y.W. Tai, *Morphological Study of Platelet Adhesion Dynamics Under Whole Blood Flow Condition*, Platelets 3(3), (1992), pp. 145-153.

[69] Y.L. Chiu, Y.L. Chou, C.Y. Jen, *Platelet Deposition Onto Fibrin-coated Surfaces Under Flow Conditions*, Blood Cells 13(3), (1988), pp. 437-450.

[70] Jobe S. M., Wilson K. M., Leo L., Raimondi A., Molkentin J. D., Lentz S. R., Di P. J., *Critical role for the mitochondrial permeability transition pore and cyclophilin D in platelet activation and thrombosis*, Blood. 111(3), (2008), pp. 1257-1265.

[71] M.M. Kamocka, J. Mu, X. Liu, N. Chen, A. Zollman, B. Sturonas-Brown, K. Dunn, Z. Xu, D.Z. Chen, M.S. Alber, E.D. Rosen, *Two-photon Intravital Imaging of clot Development*, J Biomed Opt 15(1), (2010), 016020.

[72] M. Karttunen, I. Vattulainen, A. Lukkarinen, *A Novel Methods in Soft Matter Simulations*, Springer, Berlin, (2004).

[73] E.E. Keaveny, I.V. Pivkin, M. Maxey, G.E. Karniadakis, *A comparative study between dissipative particle dynamics and molecular dynamics for simple- and complex-geometry flows*, The Journal of Chemical Physics 123, (2005), 104107.

[74] Kotova Y. N., Ataullakhanov F. I., Panteleev M. A., *Formation of coated platelets is regulated by the dense granule secretion of adenosine 5'diphosphate acting via the P2Y12 receptor*, J Thromb. Haemost. 6(9), (2008), pp. 1603-1605.

[75] Y.V. Krasotkina, E.I. Sinauridze, F.I. Ataullakhanov, *Spatiotemporal Dynamics of Fibrin Formation and Spreading of Active Thrombin Entering Non-recalcified Plasma by Diffusion*, Biochimica et Biophysica Acta 1474, (2000), pp. 337-345.

[76] M.A. Krasnoselskii, P.P. Zabreiko, *Geometrical methods of nonlinear analysis*, Springer-Verlag, New York, (1984).

[77] S. Kulkarni, S.M. Dopheide, C.L. Yap, C. Ravanat, M. Freund, P. Mangin, K.A. Heel, A. Street, I.S. Harper, F. Lanza, S.P. Jackson, *A Revised Model of Platelet Aggregation*, J. Clin. Invest. 105(6), (2000), pp. 783-791.

[78] M. Kyed, *Existence of travelling wave solutions for the heat equation in infinite cylinders with a nonlinear boundary condition*, Math. Nachr. 281(2), (2008), pp. 253-271.

[79] R.D. Langdell, R.H. Wagner, K.M. Brinkhous, *Effect of antihemophilic factor on one-stage clotting tests; a presumptive test for hemophilia and a simple one-stage antihemophilic factor assy procedure*, J. Lab. Clin. Med. 41(4), (1953), pp. 637-647.

[80] A.J. Leger, L. Covic, A. Kuliopulos, *Protease-activated receptors in cardiovascular diseases*, Circulation 114(10), (2006), pp. 1070-1077.

[81] R.I. Litvinov, J.S. Bennett, J.W. Weisel, H. Shuman, *Multi-Step Fibrinogen Binding to the Integrin αIIbβ3 Detected Using Force Spectroscopy*, Biophys J. 89(4), (2005), pp. 2824-2834.

[82] K.R. Machlus, F.C. Lin, A.S. Wolberg, *Procoagulant Activity Induced by Vascular Injury Determines Contribution of Elevated Factor VIII to Thrombosis and clot Stability in Mice*, Blood 118, (2011), pp. 3960-3968.

[83] Z. Mallat, A. Tedgui, *Apoptose et syndromes coronariens aigus*, Medecine/Sciences 20, (2004), pp. 298-303.

[84] A.G. Marshal, *Biological Chemistry: Principles, Technics, and Applications*, John Wiley and Sons, New York, (1978), p. 159.

[85] J.L. McWhirter, H. Noguchi, G. Gompper, *Flow-induced clustering and alignment of vesicles and red blood cells in microcapillaries*, PNAS 106(15), (2009), pp. 6039-6043.

[86] N. Mohandas, P.G. Gallagher, *Red cell membrane: past, present, and future*, Blood 112, (2008), pp. 3939-3948.

[87] S. Muñoz San Martín, J.L. Sebastián, M. Sancho, G.Álvarez, *Modeling Human Erythrocyte Shape and Size Abnormalities*, arXiv:q-bio/0507024 [q-bio.QM], (2005).

[88] *State-specific mortality from sudden cardiac death*, United States, 1999, MMWR Morb Mortal Wkly Rep 51, (2002), pp. 123-126.

[89] H. Noguchi, G, Gompper, *Shape transitions of fluid vesicles and red blood cells in capillary flows*, PNAS 102(40), (2005), pp. 14159-14164.

[90] T. Orfeo, S. Butenas, K.E. Brummel-Ziedins, M. Gissel, K.G. Mann, *Anticoagulation by factor Xa inhibitors*, J Thromb Haemost 8, (2010), pp. 1745-1753.

[91] Bjarne Østerud, E. Bjørklid. *Role of Monocytes in Atherogenesis*, Physiol Rev 83, (2003), pp. 1070-1086.

[92] C.J. Pallister, M.S. Watson, *Haematology, 2nd edition*, Scion Publishing Ltd, (2011).

[93] M.A. Panteleev, N.M. Ananyeva, F.I. Ataullakhanov, E.L. Saenko, *Mathematical models of blood coagulation and platelet adhesion: clinical applications*, Curr Pharm Des 13, (2007), pp. 1457-1467.

[94] M.A. Panteleev, A.N. Balandina, E.N. Lipets, M.V. Ovanesov, F.I. Ataullakhanov, *Task-oriented Modular Decomposition of Biological Networks: Trigger Mechanism in Blood Coagulation*, Biophys J 98, (2010), pp. 1751-1761.

[95] M.A. Panteleev, M.V. Ovanesov, D.A. Kireev, A.M. Shibeko, E.I. Sinauridze, N.M. Ananyeva, A.A. Butylin, E.L. Saenko, F.I. Ataullakhanov, *Spatial Propagation and Localization of Blood Coagulation are Regulated by Intrinsic and Protein C Pathways, Respectively*, Biophys J 90, (2006), pp. 1489-1500.

[96] L.A. Parunov, O.A. Fadeeva, A.N. Balandina, N.P. Soshitova, K.G. Kopylov, M.A. Kumskova, J.C. Gilbert, R.G. Schaub, K.E. McGinness, F.I. Ataullakhanov, M.A. Panteleev, *Improvement of spatial fibrin formation by the anti-TFPI aptamer BAX499: changing clot size by targeting extrinsic pathway initiation*, J Thromb Haemost 9, (2011), pp. 1825-1834.

[97] I.V. Pivkin, G.E. Karniadakis, *A New Method to Impose No-slip Boundary Conditions in Dissipative Particle Dynamics*, J. Comp. Phys. 207 (2005), pp. 114-128.

[98] I.V. Pivkin, P.D. Richardson, G. Karniadakis, *Blood flow velocity effects and role of activation delay time on growth and form of platelet thrombi*, PNAS 103, (2006), pp. 17164-17169.

[99] I.V. Pivkin, P.D. Richardson, G.E. Karniadakis, *Effect of Red Blood Cells on Platelet Aggregation*, Engineering in Medicine and Biology Magazine, IEEE 28.2, (2009), pp. 32-37.

[100] I.V. Pivkin, G.E. Karniadakis, *Accurate Coarse-Grained Modeling of Red Blood Cells*, Physical review letters, PRL 101, 118105, (2008).

[101] C. Pozrikidis, *Modeling and Simulation of Capsules and Biological Cells*, Chapman and Hall/CRC, (2003), ISBN: 978-1-58488-359-3.

[102] A.J. Quick, M. Stanley-Brown, F.W. Bancroft, *A study of the coagulation defect in hemophilia and in jaundice*, Am J Med Sci 190, (1935), pp. 501-511.

[103] D.C. Rapaport, *The Art of Molecular Dynamics Simulation*, Cambridge Univ Pr, (1996), ISBN: 0-521-44561-2.

[104] A.M. Robertson, A. Sequeira, M.V. Kamenova, *Hemorheology*, Hemodynamical Flows. Modelling, Analysis and Simulation, Oberwolfach Seminars 37(63-120), Birkhäuser Verlag Basel, (2008).

[105] U.D. Schiller, *Dissipative Particle Dynamics. A Study of the Methodological Background*, Diploma thesis at Faculty of Physics University of Bielefeld, (2005).

[106] C. Schmitt, A.H. Henni, G. Cloutier, *Characterization of blood clot viscoelasticity by dynamic ultrasound elastography and modeling of the rheological behavior*, Journal of Biomechanics 44, (2011), pp. 622-629.

[107] A.M. Shibeko, E.S. Lobanova, M.A. Panteleev, F.I. Ataullakhanov, *Blood Flow Controls Coagulation Onset via the Positive Feedback of Factor VII Activation by factor Xa*, BMC Syst Biol 4(5), (2010).

[108] A.M. Shibeko, S.A. Woodle, T.K. Lee, M.V. Ovanesov, *Unifying the mechanism of recombinant FVIIa action: dose-dependence is regulated differently by tissue factor and phospholipids*, Blood, (2012).

[109] R. Skalak, A. Tozeren, R. Zarda, S. Chein, *Strain energy function of red blood cell membranes*, Biophysical Journal 13(3), (1973), pp. 245-264.

[110] Smith R. D., Owen W. G., *Platelet Responses to Compound Interactions with ThrombinG*, Biochemistry. 38(28), (1999), pp. 8936-8947.

[111] C.R. Sweet, S. Chatterjee, Z. Xu, K. Bisordi, E.D. Rosen, M. Alber, *Modelling Platelet - Blood Flow Interaction Using the Subcellular Element Langevin Method*, J. R. Soc. Interface 8, (2011), pp. 1760-1771.

[112] A.A. Tokarev, A.A. Butylin, F.I. Ataullakhanov, *Platelet Adhesion from Shear Blood Flow is Controlled by Near-wall Rebounding Collisions with Erythrocytes*, Biophys J 100, (2011), pp. 799-808.

[113] A.A. Tokarev, A.A. Butylin, E.A. Ermakova, E.E. Shnol, G.P. Panasenko, F.I. Ataullakhanov, *Finite Platelet Size Could Be Responsible for Platelet Margination Effect*, Biophys. J. 101(8), (2011), pp. 1835-1843.

[114] A.A. Tokarev, A.A Butylin, F.I. Ataullakhanov, *Platelet Transport and Adhesion in Shear Blood Flow: the Role of Erythrocytes*, Computer Research and Modeling, 4(1), (2012), pp. 185-200 (article in Russian).

[115] A. Tokarev, I. Sirakov, G. Panasenko, V. Volpert, E. Shnol, A. Butylin, and F. Ataullakhanov, *Continuous Mathematical Model of Platelet clot Formation in Blood Flow*, Russian Journal of Numerical Analysis and Mathematical Modelling 27(2), (2012), pp. 192-212.

[116] A. Tosenberger, V. Salnikov, N. Bessonov, E. Babushkina, V. Volpert, *Particle Dynamics Methods of Blood Flow Simulations*, Math. Model. Nat. Phenom. 6(5), (2011), pp. 320-332.

[117] A. Tosenberger, F. Ataullakhanov, N. Bessonov, M. Panteleev, A. Tokarev, V. Volpert, *Modelling of clot growth and growth stop in flow by the method of dissipative particle dynamics*, Russian Journal of Numerical Analysis and Mathematical Modelling 27(5), 2012, pp. 507-522.

[118] A. Tosenberger, F. Ataullakhanov, N. Bessonov, M. Panteleev, A. Tokarev, V. Volpert, *Modelling of clot growth in flow with a DPD-PDE method*, Journal of Theoretical Biology 337, (2013), pp. 30-41.

[119] K. Tsubota, S. Wada, H. Kamada, Y. Kitagawa, R. Lima, T. Yamaguchi, *A Particle Method for Blood Flow Simulation, Application to Flowing Red Blood Cells and Platelets*, Journal of the Earth Simulator 5, (2006), pp. 2-7.

[120] K. Tsubota, S. Wada, *Elastic force of red blood cell membrane during tank-treading motion: Consideration of the membrane's natural state*, International Journal of Mechanical Sciences 52(2), (2010), pp. 356-364.

[121] V. Volpert, *Elliptic Partial Differential Equations. Volume 2. Reaction-diffusion equations*, Birkhäuser, (2013).

[122] A. Volpert, Vit. Volpert, Vl. Volpert, *Traveling wave solutions of parabolic systems*, Translation of Mathematical Monographs 140, Amer. Math. Society, Providence, (1994).

[123] V. Volpert, A. Volpert, *Spectrum of elliptic operators and stability of travelling waves*, Asymptotic Analysis 23, (2000), pp. 111-134.

[124] V. Volpert, *Elliptic partial differential equations. Volume 1. Fredholm theory of elliptic problems in unbounded domains*, Birkhäuser, (2011).

[125] C.L. Wagner, M.A. Mascelli, D.S. Neblock, H.F. Weisman, B.S. Coller, R.E. Jordan, *Analysis of GPIIb/IIIa receptor number by quantification of 7E3 binding to human platelets*, Blood 88(3), (1996), pp. 907-914.

[126] J.W. Weisel, *Enigmas of Blood Clot Elasticity*, Science 320(5875), (2008), pp. 456-457.

[127] P.J. Wellings, *Mechanisms of Platelet Capture Under Very High Shear*, Master thesis at Georgia Institute of Technology, (2011).

[128] U. Windberger, A. Bartholovitsch, R. Plasenzotti, K.J. Korak, G. Heinze, *Whole Blood Viscosity, Plasma Viscosity and Erythrocyte Aggregation in Nine Mammalian Species: Reference Values and Comparison of Data*, Exp. Physiol. 88(3), (2003), pp. 431-440.

[129] Wolfs J. L., Comfurius P., Rasmussen J. T., Keuren J. F., Lindhout T., Zwaal R. F., Bevers E. M., *Activated scramblase and inhibited aminophospholipid translocase cause phosphatidylserine exposure in a distinct platelet fraction*, Cell Mol. Life Sci. 62(13), (2005), pp. 1514-1525.

[130] Xu Z., Kamocka M., Alber M., Rosen E. D., *Computational approaches to studying clot development*, Arterioscler. Thromb. Vasc. Biol. 31(3), (2011), pp. 500-505.

[131] Z. Xu, N. Chen, M.M. Kamocka, E.D. Rosen, M. Alber, *A Multiscale Model of clot Development*, J. R. Soc. Interface 5,(2008), pp. 705-722.

[132] Z. Xu, J. Lioi, J. Mu, M.M. Kamocka, X. Liu, D.Z. Chen, E.D. Rosen, M. Alber, *A Multiscale Model of Venous clot Formation with Surface-Mediated Control of Blood Coagulation Cascade*, Biophysical Journal 98, (2010), pp. 1723-1732.

[133] Z. Xu, N. Chen, S. Shadden, J.E. Marsden, M.M. Kamocka, E.D. Rosen, M. Alber, *Study of Blood Flow Impact on Growth of Thrombi Using a Multiscale Model*, Soft Matter 5, (2009), pp. 769-779.

[134] Z. Xu, S. Christleyy, J. Lioiz, O. Kim, C. Harveyx, W. Sun, E.D. Rosen, M. Alber, *Multiscale Model of Fibrin Accumulation on the Blood Clot Surface and Platelet Dynamics*, Methods in Cell Biology 110, (2012), pp. 367-388.

[135] Z. Xu, O. Kim, M. Kamocka, E.D. Rosen, M. Alber, *Multiscale models of thrombogenesis*, Wiley Interdiscip Rev Syst Biol Med 4, (2012), pp. 237-246.

[136] C. Yeh, A.C. Calvez, E.c. Eckstein, *An estimated shape function for drift in a platelet-transport model*, Biophysical journal 67, (1994), pp. 1252-1259.

[137] T. Yamaguchi, T. Ishikawa, Y. Imai, N. Matsuki, M. Xenos, Y. Deng, D. Bluestein, *Particle-Based Methods for Multiscale Modeling of Blood Flow in the Circulation and in Devices: Challenges and Future Directions*, Ann Biomed Eng. 38(3), (2010), pp. 1225-1235.

[138] T.N. Zaidi, L.V. McIntire, D.H. Farrell, P. Thiagarajan, *Adhesion of Platelets to Surface-bound Fibrinogen Under Flow*, Blood 88(8), (1996), pp. 2967-2972.

[139] H. Zhao, E.S.G. Shaqfeh, V. Narsimhan, *Shear-induced Particle Migration and Margination in a Cellular Suspension*, Physics of Fluids 24, (2012), 011902.

[140] J. Zhang, P.C. Johnson, A.S. Popel, *Effects of Erythrocyte Deformability and Aggregation on the Cell Free Layer and Apparent Viscosity of Microscopic Blood Flows*, Microvasc Res. 77(3), (2009), pp. 265-272.

Chapter 6

Appendix A - Hybrid model implementation

In order to develop a software for the models described in Chapters 3 and 4, C++ programming language was used. It is a standard choice for writing a computation expensive scientific software because it is an intermediate-level language which enables rapid and more robust software development while, at the same time, allows a possibility of "low-level" optimization. As an object-oriented language it enables an easier development of a modular software. However, in this work the modularity of the developed software was sacrificed to a certain level in order to increase performance. Alongside the standard capabilities of C++, additional libraries have been used. The integrated development environment (IDE) of choice was MS Visual Studio 2008, accompanied with Microsoft Foundation Classes (MFC) for the development of the graphical user interface, OpenGL for 3D graphic rendering, OpenMP for parallelization, and MathGL for the plotting of graphs. For purposes of GPGPU (General-purpose computing on graphics processing units), C++ Accelerated Massive Parallelism (C++ AMP) library was used.

6.1 Code structure

This section contains a short description of the algorithm implementing the three equation hybrid model described in Section 4.2. Additionally, the main data structures used in the implementation are listed and briefly discussed.

- **ParticleData.** Object of ParticleData class encapsulates data relevant to a single particle. It contains information on the particle's current position, current velocity, forces acting on the particle, and platelet label. Data on the force is temporary and is being reset after each step of the DPD part of the algorithm. The platelet label denotes if a particle is a plasma particle or a platelet.

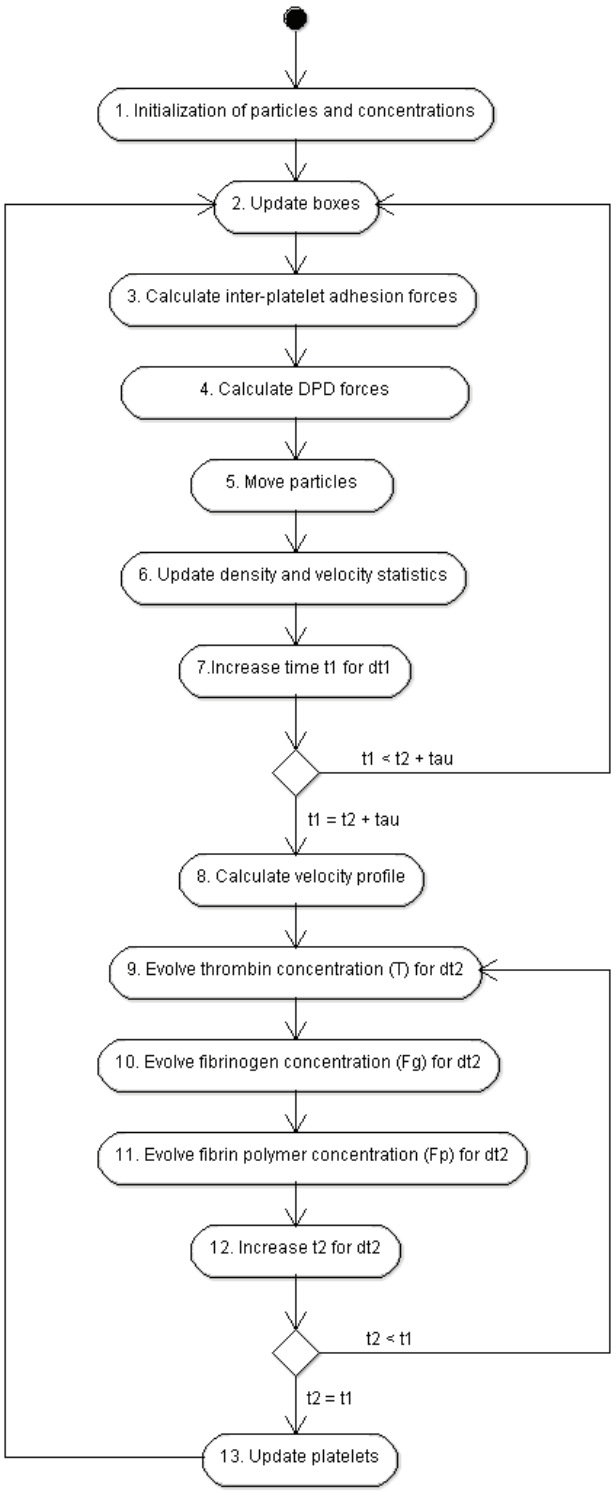

Figure 6.1: UML activity diagram of the algorithm for the three equation hybrid model.

- **CellData.** Object of CellData class contains data on a single cell (erythrocyte) membrane. The data includes a list of ids of particles that are part of the cell membrane, and supplementary data like the current cell volume. The ids of a particles is defined in the list of all particles. This structure is used in the simulation of an erythrocyte membrane. As no complex model of cells was used in the hybrid models described in Chapters 3 and 4, this structure will not be discussed further in this section.
- **BoxData.** Object of BoxData class encapsulates data related to a single box (see boxing scheme in Section 6.2.1). It contains an array of particle ids.
- **BoxPairData.** Object of BoxPairData class contains ids of two neighbouring boxes (see boxing scheme in Section 6.2.1).
- **BondData.** Object of BondData class contains ids of two connected platelet particles and a time counter which memorizes the age of the connection.
- **StatData.** Object of StatData class contains summary data on the number of particles and their velocities in some small part (or volume) of the simulation domain. The data on particles in a such volume is summarized through several steps of the DPD part of the algorithm, and is afterwards used to calculate density and velocity profiles. After, obtaining the density and velocity profiles, the data is reset.

  VelocityData. Object of VelocityData class contains an array of vectors with information on a velocity profile. The velocity profile is obtained by averaging data contained in a collection of StatData objects.

  DensityData. Object of VelocityData class contains an array with information on a density profile. Similarly to the velocity profile, the density profile is obtained by averaging data contained in a collection of StatData objects.

  ProteinData. Object of ProteinData class contains an array with information on a protein concentration profile.

The objects of classes described above were organized in the following collections:

- **Particle list.** A collection of ParticleData objects. If possible, it is preferable to store the ParticleData objects in an array, in order to achieve better simulation performance. In that case the id of the particle can be defined as the particle position in the array. If an array cannot be used because of memory limitations, a list or other, more complex collections, can be used instead. In that case each member of the list contains ParticleData object and its id. As particles are removed and created in each step of the algorithm, the performance when using the array structure can be significantly reduced. This problem can be solved by using more complex structures which have the array structure in its base, but also by using a smarter management of object insertions and removals.
- **List of boxes.** A collection of BoxData objects and their ids. The objects in the list

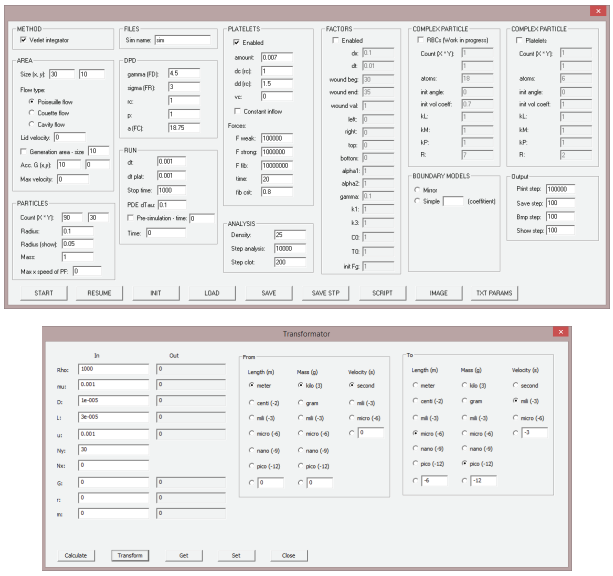

Figure 6.2: User interface for parameter input for the three equations hybrid model.

cover the whole simulation domain.

- **List of pairs of boxes.** A collection of BoxPairData objects. The list contains all pairs of neighbouring boxes (see boxing scheme in Section 6.2.1).
- **Inter-platelet connection list.** A collection of BondData objects. It contains information on all adhesive bonds that are acting between platelets.
- **List for velocity and density analysis.** A collection of StatData objects, covering the whole simulation domain. This collection serves for gathering data on particles during several steps of the DPD part of the algorithm. This data is then used to calculate density and velocity profiles.

Figure 6.1 shows the UML activity diagram of the three equation hybrid model implementation. The complexity of the problem and the extensive optimization that was done in the implementation, would make the corresponding activity diagram rather complex. Therefore, the UML diagram shown in Figure 6.1 corresponds to a more simple and less optimized version of the algorithm, where not all optimization details were considered:

1. **Initialization of particles and concentrations.** In the initialization step the simulation domain is uniformly populated with particles and their velocities that have a parabolic velocity profile corresponding to the solution of Navier-Stokes equations for the steady Poiseuille flow. The list of particles and the list of inter-platelet connections are created. A part of the particles is labelled as platelets. They are uniformly distributed and their concentration is equal to some predetermined value. Furthermore, concentration profiles for thrombin, fibrinogen and fibrin polymer are created and set to corresponding initial values. Finally, the list of boxes, corresponding to the boxing

scheme described in Section 6.2.1 is created.

2. **Update boxes.** Boxes are first emptied, then particles are separated and placed in boxes depending on their positions.

3. **Calculate inter-platelet adhesion forces.** Adhesion forces are calculated for each pair of connected platelets. If for any pair of connected platelets, their relative distance is greater than the critical distance d_D (see Section 3.1), the corresponding connection is removed from the list.

4. **Calculate DPD forces.** Following the boxing scheme described in Section 6.2.1, for each meaningful pair of boxes (Figure 6.3) DPD forces are calculated between all particles related to those boxes. If two platelets that are not connected come in physical contact, and their relative distance is smaller than the critical distance d_C (see Section 3.1), a connection between them is created and added to the list of connections.

5. **Move particles.** Each particle is moved for the corresponding total force acting on it and for the time step dt_1. If a particle interacts with the boundaries of the simulation domain, its position and velocity are adjusted following the rules for a corresponding boundary (see Section 2.3). If the Particle Generation Area is used, the particle can be removed or added to the particle list. It is removed if it crosses the SA outflow boundary. If it crosses the GA outflow boundary, its copy is added to the particle list instead. After calculating the particle's new velocity and position, the force acting on the particle resets to zero.

6. **Update density and velocity statistics.** Data for density and velocity profiles are updated with positions and velocities of particles.

7. **Increase time t_1 for dt_1.** A step of the DPD part of the algorithm ends by adding time step dt_1 to the total DPD simulation time t_1.

8. **Calculate velocity profile.** After the DPD part of the algorithm is simulated for some τ period of time, density and velocity profiles are calculated from data gathered in the same period of time.

9. **Evolve thrombin concentration (T) for dt_2.** Thrombin concentration is evolved for time step dt_2, taking into account the calculated velocity profile.

10. **Evolve fibrinogen concentration (F_g) for dt_2.** Fibrinogen concentration is evolved for time step dt_2, taking into account the calculated velocity profile and the latest thrombin concentration.

11. **Evolve fibrin polymer concentration (F_p) for dt_2.** Fibrin polymer concentration is evolved for time step dt_2, taking into account the latest fibrinogen concentration.

12. **Increase time t_2 for dt_2.** A step of the PDE part of the algorithm ends by adding time step dt_2 to the total DPD simulation time t_2.

13. **Update platelets.** Once the concentrations have been evolved for τ period of time, the status of platelets is updated. If at the platelet's position the concentration of fibrin polymer is larger than the critical concentration c_{F_p} the platelet changes its state to "non-adhesive".

6.2 Optimization

6.2.1 Boxing scheme

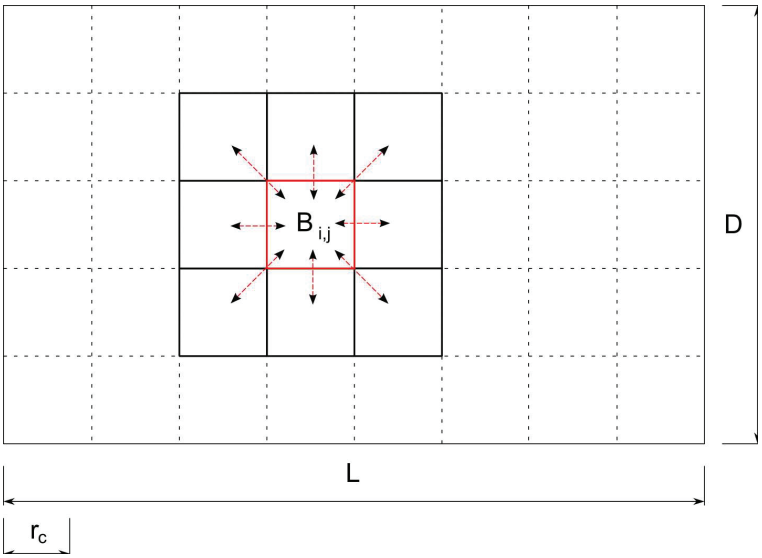

Figure 6.3: Boxing scheme: Simulation domain is divided into boxes depending on the maximal radius of inter-particle influence (r_c in DPD). Then particles from box B_{ij} are in contact with themselves and with particles from surrounding boxes. The scheme ensures that all the other particles are to far away to exert forces on particles in box B_{ij}. Reprinted with permission from [117] – *A. Tosenberger et al., Russian Journal of Numerical Analysis and Mathematical Modelling, De Gruyter, 2012.*

In DPD simulations most of the total computational time is spent on the calculations of inter-particle forces, therefore this is the part of the code where optimisation would have the largest impact. Usually, the cut-off radius of inter-particle force in DPD (r_c) is much smaller than the sizes of the simulation domain, thus the calculation of forces between all possible pairs of particles is very inefficient because most of such pairs have an inter-particle distance larger than the cut-off radius. In order to avoid as much of such pairs of particles as possible, the simulation domain, a rectangle in our 2D case, can be divided into smaller rectangles (called boxes) [18] with lengths of sides equal to $min\{x\epsilon\mathbf{R}^+|x \geq r_c \wedge \exists n\epsilon\mathbf{N} \text{ such that } L = nx\}$ and $min\{y\epsilon\mathbf{R}^+|y \geq r_c \wedge \exists n\epsilon\mathbf{N} \text{ such that } D = ny\}$, where L is the length of the domain, and D is

its height. Construction of a such rectangular subdivision ensures that for each particle p we can find its corresponding box $B_{i,j}$ and that all particles which have non-zero inter-particle force with particle p are contained in the box $B_{i,j}$ and 8 surrounding boxes. This eliminates most of the pairs of particles which have a zero inter-particle force, and therefore drastically reduces the computation time. Furthermore, the described domain subdivision enables one to easily paralellize the process of calculation of inter-particle forces by dividing the set of all pairs of "connected" boxes into multiple disjunct subsets.

Another possibility to decrease the simulation time it to increase the time step. DPD, due to its definition of the conservative force as a finite function and due to the existence of dissipating forces, enables a certain increase in the time step compared to other particle methods like Molecular Dynamics.

6.2.2 Velocity profile smoothing

In hybrid models, described in Chapter 4, the sensitivity of the model on changes in the flow is regulated by the period of data exchange between the discrete and the continuous part of the model. Reducing this period will increase the frequency of data exchange, thus making the model more precise. However, this will also reduce the measurement time for the velocity profile, and thus cause the increase of noise in the measured profile. This effect of the noise increase can be eliminated to some level by applying methods for noise filtering or smoothing. One of such methods which proved to be efficient for this problem is the Gaussian filter. In one dimension the Gaussian filter method consists of convolution of the measured data f with a normalized Gaussian function g:

$$(f * g)(x) = \int_{-\infty}^{\infty} f(t)\, g(x - t)\, dt, \tag{6.1}$$

where g is given by

$$g(x) = \frac{1}{\sigma\sqrt{2\pi}} e^{-\frac{x^2}{2\sigma^2}}. \tag{6.2}$$

and σ is the standard deviation. In two-dimensions the velocity field can be separated on components of velocity (x- and y-direction velocity profile). Then the Gaussian filter can be applied on each of the velocity profiles separately. The two dimensional Gaussian function has the following form:

$$g(x, y) = \frac{1}{2\pi\sigma^2} e^{-\frac{x^2+y^2}{2\sigma^2}}. \tag{6.3}$$

6.2.3 Dual time steps

In DPD models of platelet aggregation in flow, described in Chapters 3 and 4, the inter-platelet adhesion forces are usually much stronger than DPD inter-particle forces. Because

of the stronger forces the time step needs to be significantly lower than it would be the case in a simulation without platelet aggregation. As aggregated platelets occupy only a small part of the simulation domain, in each step of the algorithm DPD forces between particles in the rest of the domain are calculated with the unnecessary small time step. A possible way to avoid this problem and to increase the computational efficiency of the algorithm is to use two time steps, instead of only one. The first time step, dt_{dpd}, serves for DPD interactions, while the second one, dt_{plt}, is used for platelet interactions. It is expected that the DPD time step is significantly larger than the inter-platelet time step ($dt_{dpd} \gg dt_{plt}$). In the one DPD step dt_{dpd} of the algorithm the DPD forces are first calculated between all particles, including platelets. Then, before plasma particles are moved for dt_{dpd} time step, the inter-platelet forces are calculated and only platelets are moved for time step dt_{plt}. Afterwards, the inter-platelet forces are recalculated and platelets are moved for the time step dt_{plt}. This process is repeated until the sum of dt_{plt} steps is not equal to the dt_{dpd} step. Then the plasma particles are moved for dt_{dpd} time step. This approach offers a significant increase in the computational performance for simulations of clot growth.

6.2.4 Additional integration scheme for the equations of motion in DPD

In scope of this work a new method was also used. The method can be considered as semi-implicit in the context of the dissipative force, as it takes implicitly a part of the velocity term into the calculation of the dissipative force. Let us write a sum of DPD forces on some particle i:

$$\mathbf{F}_i = \sum_j \left(\mathbf{F}_{ij}^C(\mathbf{r}_i, \mathbf{r}_j) + \mathbf{F}_{ij}^D(\mathbf{r}_i, \mathbf{r}_j, \mathbf{v}_i, \mathbf{v}_j) + \mathbf{F}_{ij}^R(\mathbf{r}_i, \mathbf{r}_j) \right). \tag{6.4}$$

where the conservative and the random force depend only of the positions of the particles i and j, while the dissipative force depends additionally of particles' velocities. Let us take the velocity of the particle i in the implicit form and the remaining variables in the explicit form:

$$\mathbf{F}_i = \sum_j \left(\mathbf{F}_{ij}^C(\mathbf{r}_i^n, \mathbf{r}_j^n) + \mathbf{F}_{ij}^D(\mathbf{r}_i^n, \mathbf{r}_j^n, \mathbf{v}_i^{n+1}, \mathbf{v}_j^n) + \mathbf{F}_{ij}^R(\mathbf{r}_i^n, \mathbf{r}_j^n) \right). \tag{6.5}$$

By including it in the first step of Euler integration method (equation (2.8)) the following equation is obtained :

$$\mathbf{v}_i^{n+1} = \mathbf{v}_i^n + \frac{dt}{m_i} \sum_j \left(\mathbf{F}_{ij}^C(\mathbf{r}_i^n, \mathbf{r}_j^n) + \mathbf{F}_{ij}^D(\mathbf{r}_i^n, \mathbf{r}_j^n, \mathbf{v}_i^{n+1}, \mathbf{v}_j^n) + \mathbf{F}_{ij}^R(\mathbf{r}_i^n, \mathbf{r}_j^n) \right). \tag{6.6}$$

After expanding the dissipative force to its full form given by the equation (2.2) and placing all the expressions multiplying $\mathbf{v}_i^{n+1}$ on the left side one obtains:

$$\mathbf{v}_i^{n+1} + \frac{dt}{m}\sum_j \gamma\omega^D(r_{ij}^n)(\mathbf{v}_i^{n+1}\cdot\hat{\mathbf{r}}_{ij}^n)\hat{\mathbf{r}}_{ij}^n = \tag{6.7}$$
$$= \mathbf{v}_i^n + \frac{dt}{m_i}\sum_j \left(\mathbf{F}_{ij}^C(\mathbf{r}_i^n,\mathbf{r}_j^n) + \gamma\omega^D(r_{ij}^n)(\mathbf{v}_j^n\cdot\hat{\mathbf{r}}_{ij}^n)\hat{\mathbf{r}}_{ij}^n + \mathbf{F}_{ij}^R(\mathbf{r}_i^n,\mathbf{r}_j^n)\right),$$

where $\mathbf{r}_{ij} = \mathbf{r}_i - \mathbf{r}_j$, $r_{ij} = |\mathbf{r}_{ij}|$ and $\hat{\mathbf{r}}_{ij} = \mathbf{r}_{ij}/r_{ij}$. Now the left side of the equation (6.7) can be written as:

$$\mathbf{v}_i^{n+1}\left(I + \frac{dt}{m}\sum_j \gamma\omega^D(r_{ij}^n)(\hat{\mathbf{r}}_{ij}^n\otimes\hat{\mathbf{r}}_{ij}^n)\right) = \tag{6.8}$$
$$= \mathbf{v}_i^n + \frac{dt}{m_i}\sum_j \left(\mathbf{F}_{ij}^C(\mathbf{r}_i^n,\mathbf{r}_j^n) + \gamma\omega^D(r_{ij}^n)(\mathbf{v}_j^n\cdot\hat{\mathbf{r}}_{ij}^n)\hat{\mathbf{r}}_{ij}^n + \mathbf{F}_{ij}^R(\mathbf{r}_i^n,\mathbf{r}_j^n)\right).$$

Set

$$A = I + \frac{dt}{m}\sum_j \gamma\omega^D(r_{ij}^n)(\hat{\mathbf{r}}_{ij}^n\otimes\hat{\mathbf{r}}_{ij}^n). \tag{6.9}$$

Lemma 6.1. *If $\mathbf{v}_i \in \mathbb{R}^n$ for $i = 1,\ldots,k$ and $\alpha_i \in \mathbb{R}$, $i = 1,\ldots,k$, such that $\alpha_i \geq 0$, $\forall i$, then the matrix $A = I + \sum_{j=1}^{k}\alpha_j(\mathbf{v}_j\otimes\mathbf{v}_j)$ is invertible.*

Proof. Let us first define matrices A_i as

$$A_i = \alpha_i(\mathbf{v}_i\otimes\mathbf{v}_i), \qquad \text{for } i = 1,\ldots k. \tag{6.10}$$

Let us first note that matrices A_i, $i = 1,\ldots,k$, are symmetric and positive semi-definite as for any vector $\mathbf{x}\in\mathbb{R}^n$ we have:

$$\mathbf{x}^\tau A_i\mathbf{x} = \alpha_i\begin{pmatrix}x_1 & \ldots & x_n\end{pmatrix}\begin{pmatrix}v_1^2 & \ldots & v_1v_n\\ \vdots & \ddots & \vdots\\ v_nv_1 & \ldots & v_n^2\end{pmatrix}\begin{pmatrix}x_1\\ \vdots\\ x_n\end{pmatrix} \tag{6.11}$$

$$= \alpha_i\begin{pmatrix}v_1\sum_{i=1}^n x_iv_i & \ldots & v_n\sum_{i=1}^n x_iv_i\end{pmatrix}\begin{pmatrix}x_1\\ \vdots\\ x_n\end{pmatrix} \tag{6.12}$$

$$= \alpha_i\sum_{j=1}^n\left(x_jv_j\sum_{i=1}^n x_iv_i\right) = \alpha_i(x_1v_1+\ldots x_nv_n)^2 \geq 0. \tag{6.13}$$

As the identity matrix is positive definite and as the sum $A + B$ of a positive definite matrix A and a positive semi-definite matrix B is positive definite:

$$x^\tau Ax > 0, \qquad \forall x \in \mathbb{R}^n, x \neq 0, \tag{6.14}$$

$$x^\tau Bx \geq 0, \qquad \forall x \in \mathbb{R}^n, \tag{6.15}$$

$$x^\tau (A+B)x = (x^\tau A + x^\tau B)x = x^\tau Ax + x^\tau Bx > 0 \qquad \forall x \in \mathbb{R}^n, x \neq 0, \tag{6.16}$$

it follows that $I + \sum_{i=1}^{n} A_i$ is a positive definite matrix, and as such is invertible. □

From Lemma 6.1 it follows that the matrix A is invertible, so from the equation (6.8) we can write:

$$\mathbf{v}_i^{n+1} = \left[\mathbf{v}_i^n + \frac{dt}{m_i} \sum_j \left(\mathbf{F}_{ij}^C(\mathbf{r}_i^n, \mathbf{r}_j^n) + \gamma \omega^D(r_{ij}^n)(\mathbf{v}_j^n \cdot \hat{\mathbf{r}}_{ij}^n)\hat{\mathbf{r}}_{ij}^n + \mathbf{F}_{ij}^R(\mathbf{r}_i^n, \mathbf{r}_j^n) \right) \right] A^{-1}. \tag{6.17}$$

Once the new velocity of particle i is obtained, its new position can be calculated by the second step of Euler integration method (the equation (2.9)).

On the one hand the previously described method is not symmetrical as one part of the velocity difference $\mathbf{v}_i - \mathbf{v}_j$ is taken implicitly and the other part explicitly. As a result the particle system does not preserve its total momentum. On the other hand, for a small time step the error does not significantly influence the behaviour of the whole system, and it allows an increase of time step for the DPD method for several orders of magnitude. Because of the loss of symmetry, the method should be used cautiously and results should be verified by comparison to a more precise integration scheme.

6.2.5 Parallelism - OpenMP, GPGPU

Dissipative Particle Dynamics, as a discrete particle method allows a certain level of parallelism. Different technical solutions can be used in order to use this ability. One of them is multicore computing. A multicore processors consists of multiple execution units, called "cores", that are placed on the same chip. Each of the cores is capable of executing its own thread of instructions independently of the other cores, i.e. they can work asynchronously. Multicore processors are today present in most of the personal computers in form of central processing units (CPU). As the software for modelling blood coagulation was developed in C++, one of the most prominent application programming interfaces (API) for parallelization, called Open Multi-Processing (OMP), was used to run the code in parallel on a CPU. In a single step of the algorithm, especially if using the boxing scheme, the data (particle position, velocity, state, etc.) is being reused to some extent. However, the reuse of the data

is low compared to the number of instructions executed over the same part of data - one particle is in contact with a small number of other particles compared to the total number of particles in the system. Because of that the reuse of data in the processor cache (very fast low capacity memory) is low and RAM (fast high capacity memory) is often accessed. With this limitation on reuse of data stored in the CPU cache, and with the overhead of instructions needed to parallelize a loop that comes from OMP, it is more efficient to parallelize top loops than the nested ones. Therefore, in the algorithm (Figure 6.1) the top loops are parallelized. With this approach the performance of the simulations is significantly increased compared to a serial approach. Performance on Intel Core i7-3770 with 4 cores was around 350 percent higher in parallel (OMP) than in serial mode.

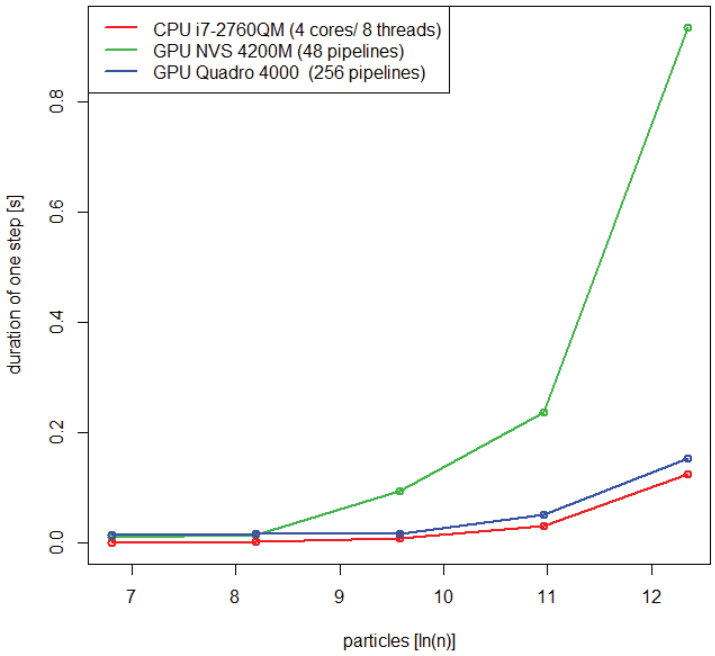

Figure 6.4: Comparison of CPU and GPU performance for 2D DPD simulations. Number of particles was varied from 900 to 230400. The test on GPU includes a single transfer of necessary data from and to GPU.

Another approach to parallel code execution, that has become very popular in scientific computing in the last decade, is general-purpose computing on graphics processing units (GPGPU). This approach makes use of graphic processing units (GPU), which are typically utilised for computer graphics, to perform computation in applications traditionally handled by CPU. Because of the parallel nature of graphic rendering problems, during the years the GPU development led to the construction of GPUs with a large number of processors that are optimized to simultaneously execute the same instruction over different pieces of

particles	CPU i7-2760QM 4 cores	GPU NVS4200M 48 cores	GPU Quadro 4000 256 cores
900	0.000684	0.010947	0.015154
3600	0.002146	0.015358	0.017762
14400	0.007634	0.093835	0.017026
57600	0.030303	0.236768	0.052430
230400	0.125000	0.934587	0.152770

Table 6.1: Comparison of CPU and GPU performance for 2D DPD simulations. Number of particles was varied from 900 to 230400. The test on GPU includes a single transfer of necessary data from and to GPU. The values in the table correspond to average duration of a single step of the DPD algorithm, expressed in seconds.

data. However, in order to exploit the significant parallel computation power of GPUs, the data from RAM memory has to be transferred to the GPU's local memory. This process is extremely costly compared to the cost of sole data processing, and hence it should not be used frequently in order to achieve better performance. Once the data is on the GPU it is stored in the GPU's global memory and is transferred to the shared memory in order to execute the instructions over that data. The transfer of data from global to shared memory is considerably slower than the execution of instructions over that data. As the size of the shared memory is extremely limited, this data transfer presents a common performance bottleneck in GPGPU. Hence, the GPGPU approach is well suited for some mathematical problems, like matrix operations in linear algebra, or n-body problem. In our model however, as a DPD particle is in contact with a rather small amount of other particles, the reuse of the data is quite low. Therefore, the transfers between the global and shared GPU memory are rather frequent, which counteracts the performance gain from large number of cores.

A 2D Poiseuille flow in a square domain was chosen to test performance of DPD method in parallel on CPU and GPU. Tests were done for the numbers of particles from 900 to 230400. The test for GPUs also included a single data transfer from RAM to GPU memory and a single transfer from GPU memory to RAM. Between the transfers 100 to 100000 steps were simulated (depending on the number of particles of the system), and the duration of a single step was calculated by dividing the total simulation time (including the two data transfers) by the number of steps. The CPU performance was tested on a machine with Intel i7-2760QM processor with 4 cores and 4GB of RAM memory. The GPU performance was tested on Nvidia NVS 42000M with 48 pipelines and Nvidia Quadro 4000 with 256 pipelines. Test results in Figure 6.4 and in Table 6.1 show a better performance on the CPU than on the two tested GPUs. However, the difference in performance on Intel i7-2760QM and Nvidia Quadro 4000 was not so large, and future advancements in GPGPU technology should lead to improvements in data transfer speeds on GPUs and to easier development of applications utilizing computing capabilities of GPUs.

6.3 Numerical method for solving reaction-diffusion-advection equation

The alternating direction implicit (ADI) method was used to solve the problem consisting of reaction-diffusion-advection equations (4.13) with conditions (4.16)–(4.20). The method is based on finite differences and is unconditionally stable. However, because of the advection term, a significant error is possible at sudden changes in velocity field. In the coagulation model this situation can occur when a part of the clot breaks off and is taken by the flow, as velocity will suddenly increase in the region of the domain previously occupied by the clot part. In order to avoid such errors in the evolution of a concentration profile, a good estimate of sufficiently small time and space steps is given by the Courant-Friedrichs-Lewy (CFL) condition:

$$C = \frac{v_x \Delta t}{\Delta x} + \frac{v_y \Delta t}{\Delta y} \leq C_{max}, \tag{6.18}$$

where C is the Courant number, v_x and v_y are x and y components of maximal velocity respectively, Δx and Δy spatial steps used in the numerical approximation (usually a finite difference method), and C_{max} is the upper boundary which depends on the numerical method being used and is equal to 1 for explicit schemes.

Below is given a detailed description of ADI method applied to a general reaction-diffusion-advection equation with a degradation term:

$$\frac{\partial T}{\partial t} = \alpha \Delta T - \nabla \cdot (\vec{v} T) + \beta(T)\,(C_0 - T) - \gamma T, \tag{6.19}$$

or

$$\frac{\partial T}{\partial t} = \alpha \left(\frac{\partial^2 T}{\partial x^2} + \frac{\partial^2 T}{\partial y^2} \right) - \frac{\partial v_x T}{\partial x} - \frac{\partial x_y T}{\partial y} + \beta(T)\,(C_0 - T) - \gamma T, \tag{6.20}$$

where

$$\beta(T) = k \frac{T^2}{T_0 + T}, \qquad 0 \leq x \leq L, \qquad 0 \leq y \leq D, \qquad 0 \leq t, \tag{6.21}$$

and with boundary conditions:

$$\left.\frac{\partial T}{\partial x}\right|_{x=0,L} = 0, \qquad \left.\frac{\partial T}{\partial y}\right|_{y=0,D} = 0. \tag{6.22}$$

The two-dimensional version of the ADI method solves the problem in two half-steps. In the first half-step the part of stencil along the x axis is implicit while the part along the y axis is explicit. Once solved, in the second half-step the y part is implicit, while the x one is explicit. The spatial steps in x and y direction and the time step are denoted by Δx, Δy and Δt respectively. The numbers of spatial nodes in x and y direction are denoted with N_x and N_y respectively.

Implicit in x, explicit in y direction. Written in terms of finite differences the equation (6.22) looks like:

$$\begin{aligned}
\frac{T_{i,j}^{n+\frac{1}{2}} - T_{i,j}^{n}}{\frac{\Delta t}{2}} &= \alpha \left(\frac{T_{i+1,j}^{n+\frac{1}{2}} - 2T_{i,j}^{n+\frac{1}{2}} + T_{i-1,j}^{n+\frac{1}{2}}}{\Delta x^2} + \frac{T_{i,j+1}^{n} - 2T_{i,j}^{n} + T_{i,j-1}^{n}}{\Delta y^2} \right) + \\
&+ \frac{1}{\Delta x} \left(k_{i-\frac{1}{2},j}^{x+} v_{i-\frac{1}{2},j}^{x} T_{i-1,j}^{n+\frac{1}{2}} + k_{i-\frac{1}{2},j}^{x-} v_{i-\frac{1}{2},j}^{x} T_{i,j}^{n+\frac{1}{2}} - \right. \\
&\left. - k_{i+\frac{1}{2},j}^{x+} v_{i+\frac{1}{2},j}^{x} T_{i,j}^{n+\frac{1}{2}} - k_{i+\frac{1}{2},j}^{x-} v_{i+\frac{1}{2},j}^{x} T_{i+1,j}^{n+\frac{1}{2}} \right) \\
&+ \frac{1}{\Delta y} \left(k_{i,j-\frac{1}{2}}^{y+} v_{i,j-\frac{1}{2}}^{y} T_{i,j-1}^{n} + k_{i,j-\frac{1}{2}}^{y-} v_{i,j-\frac{1}{2}}^{y} T_{i,j}^{n} - \right. \\
&\left. - k_{i,j+\frac{1}{2}}^{y+} v_{i,j+\frac{1}{2}}^{y} T_{i,j}^{n} - k_{i,j+\frac{1}{2}}^{y-} v_{i,j+\frac{1}{2}}^{y} T_{i,j+1}^{n} \right) \\
&+ \beta \left(T_{i,j}^{n} \right) \left(C_0 - T_{i,j}^{n+\frac{1}{2}} \right) - \gamma T_{i,j}^{n+\frac{1}{2}},
\end{aligned} \tag{6.23}$$

where

$$k_{i-\frac{1}{2},j}^{x+} = \frac{1}{2} \left(\left| v_{i-\frac{1}{2},j}^{x} \right| - v_{i-\frac{1}{2},j}^{x} \right), \qquad k_{i-\frac{1}{2},j}^{x-} = \frac{1}{2} \left(\left| v_{i-\frac{1}{2},j}^{x} \right| + v_{i-\frac{1}{2},j}^{x} \right), \tag{6.24}$$

$$k_{i,j-\frac{1}{2}}^{y+} = \frac{1}{2} \left(\left| v_{i,j-\frac{1}{2}}^{y} \right| - v_{i,j-\frac{1}{2}}^{y} \right), \qquad k_{i,j-\frac{1}{2}}^{y-} = \frac{1}{2} \left(\left| v_{i,j-\frac{1}{2}}^{y} \right| + v_{i,j-\frac{1}{2}}^{y} \right), \tag{6.25}$$

$$v_{i-\frac{1}{2},j}^{x} = \frac{v_{i-1,j}^{x} + v_{i,j}^{x}}{2}, \qquad v_{i,j-\frac{1}{2}}^{y} = \frac{v_{i,j-1}^{y} + v_{i,j}^{y}}{2}, \tag{6.26}$$

and i, j, and n denote indices of nodes on the numerical mesh in x direction, y direction, and in time respectively. The term expressing the concentration change in time is approximated by the first order forward difference, the diffusion term is approximated by

the second order central difference, while the advection terms are approximated with first order upwind scheme. The scheme generates N_y linear systems, i.e. for each $j = 1, ..., N_y$ a linear system

$$A^j X^j = B^j \tag{6.27}$$

is solved. Matrix A^j is a tridiagonal matrix with elements a_i, b_i, c_i of lower, main and upper diagonal respectively, where $i = 1, ..., N_x$:

$$a_i = -\frac{\Delta t}{2}\left(\frac{\alpha}{\Delta x^2} + \frac{1}{\Delta x} k^{x+}_{i-\frac{1}{2},j} v^x_{i-\frac{1}{2},j}\right), \tag{6.28}$$

$$b_i = 1 + \frac{\Delta t}{2}\left(\frac{2\alpha}{\Delta x^2} + \beta\left(T^n_{i,j}\right) + \gamma - k^{x-}_{i-\frac{1}{2},j} v^x_{i-\frac{1}{2},j} + k^{x+}_{i+\frac{1}{2},j} v^x_{i+\frac{1}{2},j}\right), \tag{6.29}$$

$$c_i = -\frac{\Delta t}{2}\left(\frac{\alpha}{\Delta x^2} - \frac{1}{\Delta x} k^{x-}_{i+\frac{1}{2},j} v^x_{i+\frac{1}{2},j}\right). \tag{6.30}$$

Then the elements of the vector B^j have the following form:

$$\begin{aligned} B^j_i = {} & \frac{\Delta t}{2}\left(\frac{\alpha}{\Delta y^2} + \frac{1}{\Delta y} k^{y+}_{i,j-\frac{1}{2}} v^y_{i,j-\frac{1}{2}}\right) T^n_{i,j-1} + \\ & + 1 + \frac{\Delta t}{2}\left[\left(-\frac{2\alpha}{\Delta y^2} + \frac{1}{\Delta y}\left(k^{y-}_{i,j-\frac{1}{2}} v^y_{i,j-\frac{1}{2}} - k^{y+}_{i,j+\frac{1}{2}} v^y_{i,j+\frac{1}{2}}\right)\right) T^n_{i,j} + C_0\beta\left(T^n_{i,j}\right)\right] + \\ & + \frac{\Delta t}{2}\left(\frac{\alpha}{\Delta y^2} - \frac{1}{\Delta y} k^{y-}_{i,j+\frac{1}{2}} v^y_{i,j+\frac{1}{2}}\right) T^n_{i,j+1}, \end{aligned} \tag{6.31}$$

and the elements of the vector X^j are the unknowns $X^j_i = T^{n+\frac{1}{2}}_{i,j}$, for $i = 1, ..., N_x$. As the matrix A^j is tridiagonal, the corresponding system $A^j X^j = B^j$ can be efficiently solved by the use of Thomas algorithm.

Explicit in x, implicit in y direction. In the second half-step the process is similar to the first half-step. The equation (6.22) is written in a form that is explicit in x direction and implicit in y direction:

$$\begin{aligned}
\frac{T_{i,j}^{n+1}-T_{i,j}^{n+\frac{1}{2}}}{\frac{\Delta t}{2}} &= \alpha\left(\frac{T_{i+1,j}^{n+\frac{1}{2}}-2T_{i,j}^{n+\frac{1}{2}}+T_{i-1,j}^{n+\frac{1}{2}}}{\Delta x^2}+\frac{T_{i,j+1}^{n+1}-2T_{i,j}^{n+1}+T_{i,j-1}^{n+1}}{\Delta y^2}\right)\\
&+ \frac{1}{\Delta x}\left(k_{i-\frac{1}{2},j}^{x+}v_{i-\frac{1}{2},j}^{x}T_{i-1,j}^{n+\frac{1}{2}}+k_{i-\frac{1}{2},j}^{x-}v_{i-\frac{1}{2},j}^{x}T_{i,j}^{n+\frac{1}{2}}-\right.\\
&\left.-k_{i+\frac{1}{2},j}^{x+}v_{i+\frac{1}{2},j}^{x}T_{i,j}^{n+\frac{1}{2}}-k_{i+\frac{1}{2},j}^{x-}v_{i+\frac{1}{2},j}^{x}T_{i+1,j}^{n+\frac{1}{2}}\right) \qquad (6.32)\\
&+ \frac{1}{\Delta y}\left(k_{i,j-\frac{1}{2}}^{y+}v_{i,j-\frac{1}{2}}^{y}T_{i,j-1}^{n+1}+k_{i,j-\frac{1}{2}}^{y-}v_{i,j-\frac{1}{2}}^{y}T_{i,j}^{n+1}-\right.\\
&\left.-k_{i,j+\frac{1}{2}}^{y+}v_{i,j+\frac{1}{2}}^{y}T_{i,j}^{n+1}-k_{i,j+\frac{1}{2}}^{y-}v_{i,j+\frac{1}{2}}^{y}T_{i,j+1}^{n+1}\right)\\
&+ \beta\left(T_{i,j}^{n+\frac{1}{2}}\right)\left(C_0-T_{i,j}^{n+1}\right)-\gamma T_{i,j}^{n+1}.
\end{aligned}$$

A set of linear systems

$$A^iX^i=B^i \qquad (6.33)$$

is obtained, where $i=1,...,N_x$. The matrix A^i is a tridiagonal matrix with the elements:

$$a_i = -\frac{\Delta t}{2}\left(\frac{\alpha}{\Delta y^2}+\frac{1}{\Delta y}k_{i,j-\frac{1}{2}}^{y+}v_{i,j-\frac{1}{2}}^{y}\right), \qquad (6.34)$$

$$b_i = 1+\frac{\Delta t}{2}\left(\frac{2\alpha}{\Delta y^2}+\beta\left(T_{i,j}^{n+\frac{1}{2}}\right)+\gamma-k_{i,j-\frac{1}{2}}^{y-}v_{i,j-\frac{1}{2}}^{y}+k_{i,j+\frac{1}{2}}^{y+}v_{i,j+\frac{1}{2}}^{y}\right), \qquad (6.35)$$

$$c_i = -\frac{\Delta t}{2}\left(\frac{\alpha}{\Delta y^2}-\frac{1}{\Delta y}k_{i,j+\frac{1}{2}}^{y-}v_{i,j+\frac{1}{2}}^{y}\right). \qquad (6.36)$$

where $j=1,...,N_y$. The elements of vector B^i are given with:

$$\begin{aligned}
B_j^i &= \frac{\Delta t}{2}\left(\frac{\alpha}{\Delta x^2}+\frac{1}{\Delta x}k_{i-\frac{1}{2},j}^{x+}v_{i-\frac{1}{2},j}^{x}\right)T_{i-1,j}^{n+\frac{1}{2}}+\\
&+ 1+\frac{\Delta t}{2}\left[\left(-\frac{2\alpha}{\Delta x^2}+\frac{1}{\Delta x}\left(k_{i-\frac{1}{2},j}^{x-}v_{i-\frac{1}{2},j}^{x}-k_{i+\frac{1}{2},j}^{x+}v_{i+\frac{1}{2},j}^{x}\right)\right)T_{i,j}^{n+\frac{1}{2}}+C_0\beta\left(T_{i,j}^{n+\frac{1}{2}}\right)\right]+\\
&+ \frac{\Delta t}{2}\left(\frac{\alpha}{\Delta x^2}-\frac{1}{\Delta x}k_{i+\frac{1}{2},j}^{x-}v_{i+\frac{1}{2},j}^{x}\right)T_{i+1,j}^{n+\frac{1}{2}}, \qquad (6.37)
\end{aligned}$$

while the elements of the vector X^i are unknowns $X^i_j = T^{n+1}_{i,j}$, $j = 1, ..., N_y$.

Boundary conditions. The ADI method reduces the problem of solving (6.20)-(6.22) to the problem of separately a series of linear systems (6.27) and (6.33) in each time step. As the linear systems (6.27) and (6.33) are characterised by a tridiagonal square matrix A^i in the first half-step or matrix A^j in the second half-step, each of the systems can be efficiently solved by use of Thomas algorithm. The implementation of Dirichlet boundary condition is simple and straight-forward, i.e. the elements b_1 and b_N are set to 1, c_1 and a_{N-1} to 0 and B_1 and B_N to the corresponding values of Dirichlet boundary conditions. Zero Neumann boundary conditions can be implemented by use of the similar method that is used in solving 1-D problems. The method follows directly from the interpretation of the boundary conditions as finite difference, which in terms of the coefficients of matrix A results in setting the elements b_1 and b_N again to 1, while the elements c_1 and a_{N-1} are set to -1. However in 2-D and higher dimensions this method can result in instability near the boundary, hence use of another method which uses so-called "ghost nodes" is preferable. In this method additional nodes are added outside the boundaries, with indices 0 and $N+1$, and the values in these nodes are considered to be equal to the values in the adjacent boundary nodes. Therefore, in the equations (6.24) and (6.33) for $i = 1$ all the variables of concentration and velocity in the "ghost node" with the index $i - 1 = 0$, can be substituted by variables in the corresponding nodes with the index $i = 0$. The same is applied by analogy to all equations involving "ghost nodes" with indices $i = 0, N_x + 1$ or $j = 0, N_y + 1$.

6.4 Proof of lemma 5.7

In order to simplify the presentation, we will suppose throughout this proof that the solution w of problem (5.35)-(5.37) exponentially converges to 0 at infinity together with its first derivatives, and

$$\int_\Omega |w(x, y)|dxdy \leq M.$$

In general, if it is not the case, we subtract some given sufficiently smooth function with the limits $u_\pm(y)$ as $x \to \pm\infty$. Exponential convergence of solution to its limits at infinity follows from the Fredholm property of the corresponding operator.

We multiply equation (5.35) by w and integrate over Ω. Taking into account the boundary conditions, we obtain the estimate

$$\int_\Omega |\nabla w|^2 dxdy \leq C.$$

Here and below we denote by C any constant which depends only on K, M and c. Hence $\partial w/\partial y \in L^2(\Omega)$.

Set $v = \partial w/\partial y$. Then this function satisfies the problem

$$\Delta v + c\frac{\partial v}{\partial x} + f'_\tau(w)v = 0, \tag{6.38}$$

$$y = 0 : v = 0, \quad y = 1 : v = g_\tau(w). \tag{6.39}$$

Here and below f'_τ and g'_τ denotes the derivatives of these functions with respect to w. Put $\phi = f'_\tau(w)v$ and consider the auxiliary problems

$$\Delta v_\pm + c\frac{\partial v_\pm}{\partial x} + \phi = 0, \tag{6.40}$$

$$y = 0 : v_\pm = 0, \quad y = 1 : v_\pm = \pm K. \tag{6.41}$$

Then from the maximum principle

$$v_-(x, y) \le v(x, y) \le v_+(x, y), \quad (x, y) \in \Omega.$$

Since the function $f'_\tau(w)$ is bounded, then $\phi \in L^2(\Omega)$. Therefore problems (6.40), (6.41) are solvable in $H^2(\Omega)$, and their norms depend only on K, M and c. By virtue of embedding theorems (on bounded subsets), the functions $v_\pm(x, y)$ are bounded and, consequently, solution v of problem (6.38), (6.39) admits the estimate:

$$\sup_{(x,y)\in\Omega} |v(x, y)| \le C. \tag{6.42}$$

Next, we multiply equation (6.38) by v and integrate over Ω. Taking into account that $v = 0$ at $y = 0$ and

$$\frac{\partial v}{\partial y} = g'_\tau(w)g_\tau(w), \quad y = 1,$$

we obtain the estimate

$$\int_\Omega |\nabla v(x, y)|^2 dxdy \le C. \tag{6.43}$$

Hence $\partial v/\partial y \in L^2(\Omega)$.

Set $z = \partial v/\partial y$. Then this function satisfies the equation

$$\Delta z + c\frac{\partial z}{\partial x} + f'_\tau(w)z + f''_\tau(w)v^2 = 0. \tag{6.44}$$

Since the boundary condition for z at $y = 0$ is not defined, we extend this problem by symmetry and consider it in the domain

$$\widehat{\Omega} = \{-\infty < x < \infty,\ \ -1 < y < 1\}$$

with the boundary conditions

$$|y| = 1 : z = g'_\tau(w)g_\tau(w). \tag{6.45}$$

Put

$$\zeta = f'_\tau(u)z + f''_\tau(u)v^2$$

and consider the auxiliary problems

$$\Delta z + c\frac{\partial z}{\partial x} + \zeta = 0. \tag{6.46}$$

$$|y| = 1 : z = \pm K^2. \tag{6.47}$$

As before, $z_- \le z \le z_+$, where z is a solution of problem (6.44), (6.45) and $z_\pm$ are solutions of problems (6.46), (6.47).

Since $v, z \in L^2(\Omega)$ and v is bounded, then $\zeta \in L^2(\Omega)$. As above, we prove that the functions $z_\pm$ are bounded. Hence

$$\sup_{(x,y)\in\Omega} \Big|\frac{\partial^2 w}{\partial y^2}\Big| \le C. \tag{6.48}$$

Having proved this estimate, we return to equation (5.35) which we consider as a second-order ordinary differential equation (y is a fixed parameter):

$$U'' + cU' + H = 0,$$

where $U(x) = w(x, y)$, prime denotes the derivative with respect to x,

$$H(x) = \frac{\partial^2 u}{\partial y^2} + f_\tau(w(x, y)).$$

By virtue of (6.48) and boundedness of the function f_τ, $H(x)$ is also bounded. Multiplying the last equation by U and integrating from $-\infty$ to ∞, we estimate the first derivative U' in

the L^2-norm. Next, we multiply the same equation by U' and integrate from $-\infty$ to x. This gives an estimate of U' in the supremum norm. From the estimate of the first derivative and the equation it follows the estimate of the second derivative U''. Hence

$$\sup_{(x,y)\in\Omega} |\frac{\partial w}{\partial x}|, |\frac{\partial^2 w}{\partial x^2}| \leq C. \tag{6.49}$$

Thus we have proved that $w \in C^2(\bar{\Omega})$. Finally, we write problem (5.35)-(5.37) in the form

$$\Delta w + c\frac{\partial w}{\partial x} + \beta(x,y) = 0, \tag{6.50}$$

$$y = 0 : \frac{\partial w}{\partial y} = 0, \quad y = 1 : \frac{\partial w}{\partial y} = \gamma(x,y), \tag{6.51}$$

where $\beta(= f_\tau) \in C^\alpha(\bar{\Omega})$ and $\gamma(= g_\tau) \in C^{1+\alpha}(\bar{\Omega})$, $0 < \alpha < 1$. From a priori estimates of solutions it follows that $u \in C^{2+\alpha}(\bar{\Omega})$, and the norm of the solution depends on K, M and c.

□